Optimizing the Efficiency and Cost of Catalysts for Sustainable Energy Applications: First-Principles Density Functional Theory Studies

by

Yusu Liu

B.S., Yale University (2015)

Submitted to the Department of Materials Science and Engineering
in partial fulfillment of the requirements for the degree of

Doctor of Philosophy in Materials Science and Engineering

at the

MASSACHUSETTS INSTITUTE OF TECHNOLOGY

June 2019

Signature redacted

Author .....
Department of Materials Science and Engineering
May 3, 2019

Signature redacted

Certified by .....
Jeffrey C. Grossman
Professor
Thesis Supervisor

Signature redacted

Accepted by .....
Donald R. Sadoway
Chairman, Department Committee on Graduate Studies

Optimizing the Efficiency and Cost of Catalysts for Sustainable Energy Applications: First-Principles Density Functional Theory Studies

by

Yusu Liu

Submitted to the Department of Materials Science and Engineering
on May 3, 2019, in partial fulfillment of the
requirements for the degree of
Doctor of Philosophy in Materials Science and Engineering

Abstract

In this thesis, I tackled, on two key fronts, the challenge of designing optimal catalysts for a sustainable future built on renewables. On the efficiency front, I studied electrochemical water-splitting, a reaction important for on-demand renewable energy conversion. I presented the electronic origin and feasibility of surface lattice oxygen participation during the kinetic bottleneck of the water-splitting reaction on perovskites with competing reactions, solvent effects and vacancy effects. On the cost reduction front, I provided design guidelines based on electronic structure modifications that employ core-shell nanoparticle architectures to reduce the loading of expensive noble metal catalysts.

Thesis Supervisor: Jeffrey C. Grossman
Title: Professor

Acknowledgments

It would be quite an understatement to characterize my PhD career as being 'eventful' (I imagine this sentence would undoubtedly put a smile on the faces of friends and family familiar with the matter). Though I won't divulge the details of the dramatic turns that took place, both on personal and professional fronts, I must thank the people whom in person or through their ideas, have delivered me through tough and unexpected times.

To Prof. Alexie Kolpak, I most genuinely believe that your actions and your character exemplify 'the best angels of our nature'. I have not met a single soul who is not deeply touched by your mind or your heart. It feels thus almost redundant to recount how you have impacted me - but let me just say that I will always look up to you, in a clumsy albeit sincere attempt to imitate your warmth and strength.

To Prof. Jeffrey Grossman, your steadfast support has anchored me (quite literally in 13-4069) through the most tumultuous periods of my time at MIT. In the depth of roaring tides of many forms, you have always helped me see a way through and went out of your way to ensure that. I am so grateful for your kindness.

To my committee members Prof. Alfredo Alexander-Katz and Prof. Rafael Gomez-Bombarelli, thank you for your valuable suggestions and kind understanding as I navigated my PhD. I am especially indebted to you for teaching me how to deliver ideas with clarity as I put together a coherent thesis.

To Prof. Jongsuk Yoo, who was the postdoc mentor every graduate student wishes he has but I actually had the good fortune of having. Jongsuk possesses an astonishing generosity of spirit and inquisitiveness that truly inspired me as we worked on papers together. From hands-on tutorials to much needed constructive criticism, Jongsuk has truly molded me into the researcher that I am today.

Now on to my personal connections, whom, given that this is a primarily academic document, I shall only acknowledge briefly but deeply.

To my forever coffee break gang of, well, without me now, three, so much was shared in DMSE commons in the past four years. You are truly like my family in

graduate school.

To my bag/strong friends, it is so rare to find a group of people who are on the same frequency. Though as a 'menshmen' I cannot verbalize my deep gratitude, let me just say I think you are all very prestigious.

To the many lab mates I had, graduate school would have been a dreadful bore without you. It is a my personal fortune to have met each one of you and I will remember you fondly.

To Firth's ship, may every Christmas be a glorious miracle.

Last but not least, my family. Though I never say it out loud, you are my constant source of strength and inspiration.

And for course, as my high school motto goes, 'to God be the glory, the best is yet to be'.

Contents

List of Figures

List of Tables

Chapter 1

Introduction

1.1 Motivation for Sustainable Energy Catalysts

The global economy depends on the transformation and utilization of energy. In the 18th century, the industrial revolution, which transformed the landscape of labor and ushered in the age of machines, was driven by the combustion of coals to power steam engines. Since the 20th century, oil and electricity became the backbones of every indispensable aspect of our daily lives - automobiles, the light bulbs, refrigerators, computers and so on.

According to the United Nations Development program, both human development and economic development have a positive correlation with energy consumption [3]. Therefore, it is expected that the continued flourishing of mankind will only lead to a larger consumption of energy, surpassing the current 4 tonne of oil equivalent (toe) per capita in developed countries [4]. As with all things in life, energy is also a double-edged sword. Since about 80% of energy generation in the world rely on fossil fuels [4], the release of greenhouse gases in the process has an effect on the rising temperature of the planet. Current policy measures to counter the aforementioned detriment include imposing carbon taxes on CO_2 generation, subsidizing renewable energy industries and implementing local as well as nationwide energy standards. These policy measures, however, cannot counteract the fact that delivering on-demand clean energy to consumers is still very expensive. It is challenging to phase out fossil fuels without putting a hefty price tag on either the state or everyday consumers. Therefore, bringing down the cost and increasing the efficiency of the clean energy industry will be the market force supplement to government intervention for a renewable future.

To do so, enhancing the performance and reducing the cost of the catalysts used in the clean energy industry are of crucial importance. Catalysts are substances that increase the rate of reactions by providing an alternative pathway for bond-breaking and bond-making (Figure 1-1). As this alternative pathway has a lower activation energy than that required without the presence of the catalyst, the overall energy needed to drive the reaction forward is reduced. Many renewables-relevant reactions depend on next-generation novel materials that act as catalysts to reduce the energy

required to generate clean energy. This is intuitive because if a large amount of energy is required to produce clean fuels or to store them, the value of these renewable sources is compromised. For example, electricity supplies the energy for electrochemical water splitting which produces hydrogen, a clean energy fuel. This process is also used to store energy for on-demand energy conversion. If too much electricity is required, the generation of that extra input electricity would reduce the net energy we can harvest out of clean fuels. Therefore, electrochemical water-splitting use catalysts like metal oxides [5] to reduce the input energy. Another example is biodiesel production which relies on catalysts such as alkaline earth oxides [6]. If we can improve the efficiency of these catalysts, less energy and less catalysts are required to support the clean energy economy. In addition, if we can bring down the cost of these catalysts by using cheaper alternative without compromising performance, we can reduce, on the generation front, the price tag of clean fuels, making them more feasible and accessible for large-scale adoption.

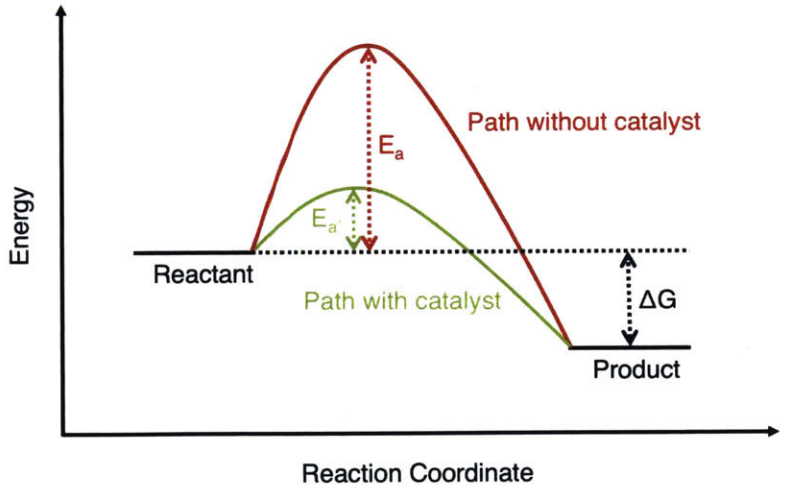

Figure 1-1: Schematics illustrating how a catalyst alters reaction energetics. The reaction goes through a pathway with lower activation energy ($E_{a'}$) with a catalyst compared to that of the pathway without the catalyst (E_a). The Gibbs free energy (ΔG) of the reaction is the energy difference between the reactant and the product. ΔG stays unchanged when a catalyst is added.

In this thesis, two classes of materials are investigated to tackle both the efficiency and cost fronts of improving current catalysts with sustainable energy applications.

Specifically, a new mechanism that reduces the overall energy required to split water using perovskites as catalysts is proposed and investigated. We show that this new mechanism, which involves the direct participation of catalyst atoms in the reaction, requires a lower theoretical overpotential than the previous consensus mechanism, and therefore is a breakthrough point for increasing the efficiency of electrochemical water splitting. In addition, we demonstrate the feasibility of this mechanism on representative catalyst surfaces with solvation effects and competing side reactions taken into consideration. We also propose the electronic origin of the thermodynamic driving force for this new mechanism. Lastly, we evaluate how oxygen nonstoichiometry affects the reaction energetics of the proposed mechanism on various catalysts.

On the cost side, a detailed electronic structural understanding is presented for transition-metal core-shell nanoparticles, which can reduce the amount of noble metal loading in catalysis and therefore bring down the cost. We explain the mechanism through which the core-shell architecture alters the performance of precious metal catalysts and provide fundamental insights into routes of modification through which they can be tuned to mimic the catalytic performance of pure noble metal catalysts.

1.2 Perovskites and the Oxygen Evolution Reaction for the Generation and Storage of Renewable Energy

1.2.1 Perovskites as Catalysts

Perovskite oxides have the general chemical formula of ABO_3, where the B site ions, usually a transition metal, form a corner-sharing octahedra of O anions, and the larger A-site cations, usually rare-earth metals are 12-coordinated with O as shown in Figure 1-2. Given the flexibility of the perovskite structure to accommodate a wide range of A-site and B-site metals, it affords a vast chemical space where its structural and electronic properties can be tuned to suit the needs of a particular chemical reaction. In addition, perovskites' flexible tolerance for substitutions and nonstoichiometry, be it in the metallic or the oxygen sites, provides further grounds of exploration. The structural integrity of the perovskite structure depends on two factors: accommodating the ionic radii of the composition and electroneutrality. In an ideal perovskite, the structure is cubic and the ionic radii of the three species should satisfy the Goldschmidt [7] tolerance factor (t):

$$t = \frac{r_A + r_O}{\sqrt{r_B + r_O}}$$

where t is between 0.75 and 1 (ideal case). When multiple types of A-site or B-site ions are present due to substitution, the positions of the oxygen are slightly shifted to optimize for radii and charges [8]. In addition, orthorhombic, rhombohedral, tetragonal, monoclinic, and triclinic symmetries are also observed to accomodate deviations from the ideal structure [9–11]. To preserve charge neutrality, the sum of charges of the A-site and B-site ions should sum to 6 per 3 oxygens. This gives rise to a wide range of substitutions allowed that satisfy the criterion. In a similar manner, to accommodate oxygen excess, perovskites can use cation nonstoichiometry to balance. For example, in the case of $CaTiO_3$, a combination of stoichiometric

binary oxides CaO and TiO2 can exist with an excess of 1% TiO_2 [12]. In case of oxygen defects, (A -site B-site strategies)

Thanks to perovskites versatility, they have proven to be a tunable class of materials with applications in many industrially relevant applications such as electrochemical water splitting [13–15], nitrogen reduction [16–18], carbon dioxide reduction [19–21], solar cells [22–24]and solid oxide fuel cells [25–27].

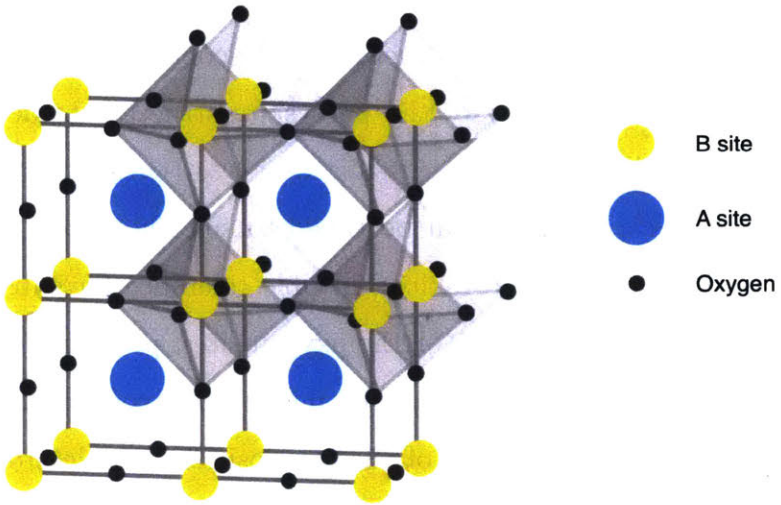

Figure 1-2: Illustration of the perovskite oxide structure. Yellow circles indicate B site, blue circles indicate A site and grey circles indicate oxygen.

One key aspect to perovskites' versatility that makes them efficient, stable and selective for a vast variety of chemical reactions lies in the fact that the metal-oxygen bond in perovskites is highly tunable and can be employed to control surface binding which is essential for reaction energetics [28]. Given that quantifying properties at the atomic bond scale is time-consuming and challenging with experiments, theoretical studies, such as those employing Density Functional Theory (DFT) which is the central method of this thesis, become critical in accelerating materials discovery and gaining critical insights into the fundamental physical forces governing the catalytic behavior of perovskites.

1.2.2 The Water Splitting Reaction

Two of the most important challenges to overcome in order to advance towards a clean energy future are cheap and efficient energy production and high energy storage per volume at scale [29]. Currently there are many limitations on these two fronts. For example, electricity generated by wind or solar needs efficient storage and on-demand conversion due to the intermittent nature of their generation. Hydropower is costly and the interruption it introduces in natural waterways can have adverse environmental effects.

The eletrochemical water splitting reaction, which produces hydrogen, is an important reaction to solve the above mentioned problems that both generates a clean fuel and serves as a key technology for seasonal and portable storage of energy [30–32]. Currently, commonly employed methods for customer energy management,bulk and renewables storage [33] include pumped storage hydropower, compressed air energy storage, flywheels and batteries. Of these methods, batteries have the unique advantage of being the most portable option and can be used in applications such as electric vehicles. Li-ion battery has become a popular choice due its relative environmental-friendliness compared to lead-acid batteries that use sulfuric acid and large amounts of lead. In addition, lead has adverse health effects that upon exposure are detrimental to young children in particular [34]. In terms of operating conditions, Li-ion batteries can operate at room temperature compared to around 300° for many molten salt batteries [35] this is of paramount importance for portable applications such as electric vehicles.

Despite the popularity of Li-ion batteries, hydrogen as a fuel storage option offers additional competitive advantages. Firstly, hydrogen has a 2 orders of magnitude higher theoretical mass energy density compared to Li-ion battery as compressed hydrogen has an energy density of 142 MJ/kg and Li-ion batteries sit at an energy density of 0.6 MJ/kg. This enables hydrogen-fueled vehicles to have a shorter charging time and travel further. Secondly, hydrogen has other applications in the chemicals industry such as serving as a reactant in ammonia and synthetic natural gas.

In water electrolysis, electrical energy is converted to chemical energy via the formula:

$$H_2O \rightarrow H_2 + \frac{1}{2}O_2 \tag{1.1}$$

The electrical energy can be recovered through the reverse reaction where hydrogen and oxygen are combined in a combustion cell to produce water. Water electrolysis can be coupled to wind, solar or geothermal where the electricity generated by these renewable sources are used to drive the electrolysis and the energy is stored as hydrogen and oxygen. This coupling enables excess electricity to be stored when supply is greater than demand and then converted back when the energy need increases. A schematic of the energy flow is shown in Figure 1-3. Evidently, the role of water electrolysis is two-fold: energy generation and energy storage. Through the conversion of electrical energy to chemical energy stored in hydrogen, this energy can either be harvested in a fuel cell to regenerate electricity, or stored as compressed hydrogen for future use.

Water electrolysis has two half reactions, one takes place at the negatively charged anode, the other at the positive charged cathode (Figure 1-4). At the anode, oxidation takes place to generate oxygen with the following half reaction:

$$2H_2O \rightarrow O_2 + 4H^+ + 4e^- \tag{1.2}$$

This reaction is called the oxygen evolution reaction (OER).

At the cathode, reduction takes place to generate hydrogen as shown in the half reaction below:

$$2H^+ + 2e^- \rightarrow H_2 \tag{1.3}$$

This reaction is called the hydrogen evolution reaction (HER).

The minimum cell voltage required to drive the reaction is given under standard temperature and pressure as:

$$E^0_{cell} = \frac{-\Delta G^0}{nF} \tag{1.4}$$

where ΔG^0 is the Gibbs free energy under standard temperature and pressure, n is

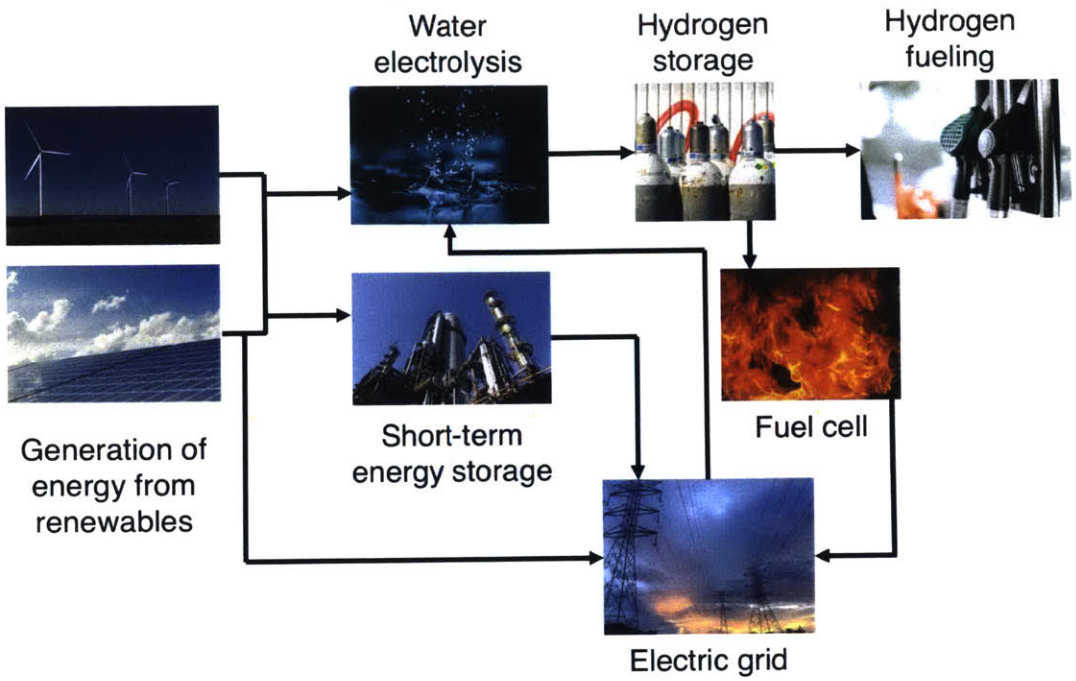

Figure 1-3: Schematic showing the storage and utilization of renewable energy via water electrolysis. Energy generated from renewable sources can be supplied to the electric grid for immediate usage, stored short-term, or drive water electrolysis which produces hydrogen. The hydrogen produced can be used in hydrogen fueling, or used later in fuel cells to produce energy that is supplied to the electric grid.

the number of electrons transferred during the reaction and F is Faraday's constant. For water electrolysis, E^0_{cell} is 1.23 eV [36]. As the OER is the thermodynamic and kinetic bottleneck of the reaction, much research has been dedicated to finding a suitable catalyst that both optimizes activity and stability [15].

Understanding the behavior of existing catalysts and designing the ideal OER catalyst candidate both require detailed mechanistic insights of how the reaction takes place on an atomic scale. Therefore, theoretical study affords a cost-effective means to investigate the reaction mechanisms of OER. This thesis will discuss at length a novel mechanism and dissect its kinetic and thermodynamic properties in great detail.

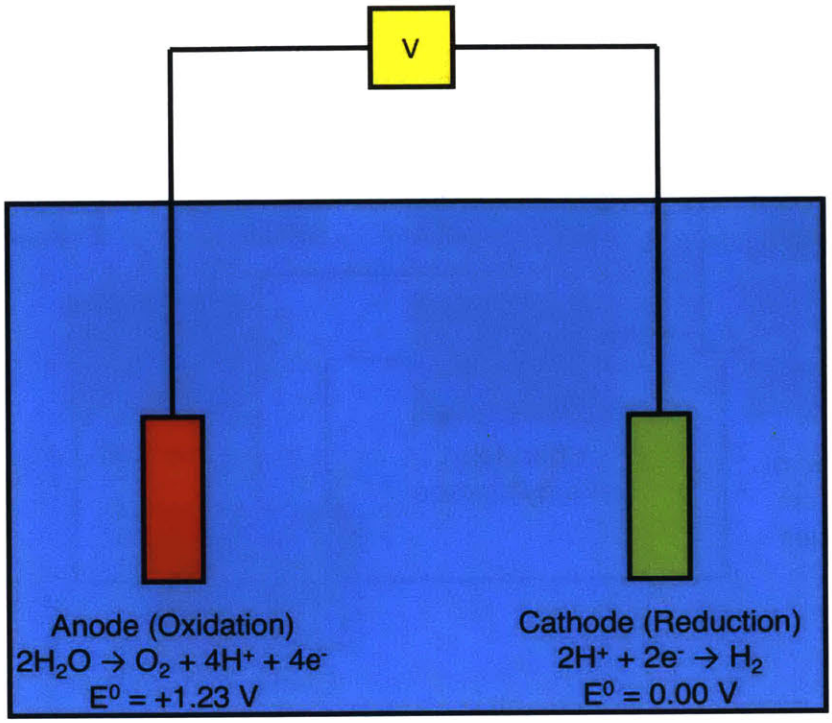

Figure 1-4: Schematics showing the the two half reactions of water electrolysis.

1.3 Cost Reduction via Core-Shell Nanoparticles

1.3.1 Properties of Core-Shell Nanoparticles

Noble metals, metals that are resistant to corrosion and oxidation in moist air, such as platinum and gold, make up 70% of the world heterogeneous catalyst market, and experience a growth of 8% per year [37]. They play a key role in improving the efficiency of renewables-relevant applications including fuel cells and water splitting [38–41].

Their high activity and stability are key drivers of their demand but their scarcity and high cost pose challenges for their long-term availability and economic feasibility [42–45]. To implement infrastracture such as hydrogen storage through catalyzing water electrolysis at a global scale, it is essential to discover new materials that are cheap and sustainable to manufacture. To reduce precious metal usage, many strategies have been employed. Most commercially available noble metal catalysts

come in the form of nanoparticles dispersed on top of a cheap support such as an oxide or carbon. However, this geometry suffers from problems such as poisoning, dissolution and support degradation [46, 47]. Single atom catalysts and clustered catalysts are also used but the lack of adjacent noble metal sites and high under-coordination hinders their broad application [48]. One route for improvement is to employ a core-shell architecture that has a noble metal shell which preserves their catalytic abilities but replace the core with cheaper materials (Figure 1-5). This class of materials is highly tunable as their size, shape, core material, core percentage, shell thickness and composition can all be modified to suit the needs of a particular reaction [48, 49].

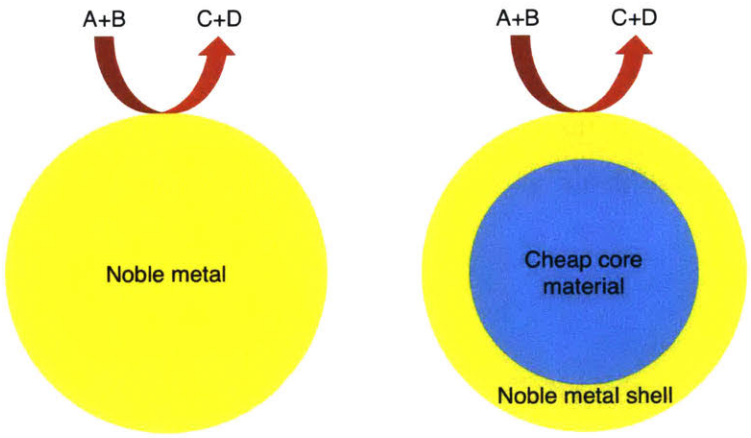

Figure 1-5: Schematics showing the composition of a core-shell nanoparticle (right) compared to a noble metal nanoparticle.

Despite these attractive properties, there are two challenges that need to be overcome. Firstly, progress needs to be made on the synthesis front to achieve independent control of core and shell properties. Secondly, in order to know what to synthesize, theoretical studies need to be conducted to investigate how the core modifies shell properties [48].

1.3.2 Transition Metal Ceramic Core

To understand what materials make the ideal core, we first need to establish a set of criteria governing properties desirable in a core material. These properties include: abundance, low cost, heat resistance, corrosion resistance, strong interfacial interaction with shell without alloying, and synthetically feasibility [48]. One class of materials that satisfy many of these criteria is transition metal ceramics. They are transition metals with non-metal elements such as carbon, nitrogen and phosphorus intercalated in the interstitial sites of the parent metal. They have been proven to endure both alkaline and acidic conditions [50]. Furthermore, they exhibit noble-metal like properties for example catalysis of reactions involving C-H bonds [51–53] and have been used to modify the properties of noble metal catalysts [54–56]. In addition, they have not been observed to alloy with noble metals [48].

Recent advances in the synthesis of transition metal ceramic core with noble metal shell nanoparticles [57–59] have paved the way for further exploration of this class of materials. Theoretical insight is needed to further elucidate structure-activity relationships which is difficult to observe under reaction conditions.

1.4 Summary of Thesis Scope and Significance

In this thesis, two key challenges in the quest for achieving a clean-energy future are addressed, namely efficiency and cost, on two specific catalytic systems. On the efficiency front, a new reaction mechanism that leads to overall the lowest overpotential for water electrolysis on perovskites is presented and its thermodynamic driving force, as well as feasibility under various reaction conditions investigated. Secondly, on the cost front, fundamental insights are obtained on a class of promising core-shell materials which could guide the future design of economically viable, low precious-metal-loading catalysts.

Chapter 2

Theoretical Background and Methodology

2.1 Theoretical Studies of Heterogeneous Catalysis

Heterogeneous catalysis takes place at interfaces such as that between gas and solid, or gas and liquid phases. Therefore, to study a reaction and its energetics, one not only has to model the bond-breaking, bond-making and electron transfer that occurs in the phase that the reactants are in, but also the reactants' interaction with the catalytic surface. Since the way a catalyst modifies the reaction pathway and lowers the energy barrier is through bonding with the reactants to modify the existing bonds in the reactants, the surface-adsorbate interaction is of paramount importance in the study of heterogeneous catalysis. In fact, the strength of this interaction has been shown to determine reaction energies and therefore catalytic activities [1, 5, 60]. In this section, the two most important concepts underlying this relationship are laid out in detail.

2.1.1 Electronic Description of Adsorption

Since this thesis concerns heterogeneous catalysis where the adsorption site is a transition metal, we narrow our scope to the discussion of models most relevant to transition metal catalysis. The most used model in this field to describe reactivity trends and adsorption energy is the d-band model [61, 62] as it has been verified experimentally with X-ray emission (XES) and X-ray adsorption (XAS) spectra [1] and agree well with both experimentally measured [63] and calculated adsorption energies [64].

Consider an adsorbate's interaction with a transition metal surface - this interaction can be described in electronic terms as the coupling between the valence states of the adsorbate and the s,d states of the transition metal [1]. This model is illustrated in Figure 2-1, which is adapted from Reference [1]. We can consider the adsorption energy then as:

$$\Delta E_{ads} = \Delta E_s + \Delta E_d \tag{2.1}$$

The first term describes the interaction energy between the adsorbate and the s

band of the metal while the second term describes the interaction energy between the adsorbate and the d band of the metal. All transition metals have half-filled s bands (red band in Figure 2-1) in the metallic state. These bands are broad and therefore cause a shift and a broadening of the adsorbate states. Since this interaction does not vary much across transition metals, it does not contribute significantly to the difference in bonding between an adsorbate and different transition metals. The d states are more localized and therefore the d band (green band in Figure 2-1) is narrower than the s band. As the broadened adsorbate band couples to the d band, it is split into bonding and antibonding states. The filling of these states depend on the d band level of the metal. The electrons will fill all the way to the Fermi level. If more antibonding states are located below the Fermi level, these filled antibonding states will destablize the overall adsorbate-metal system and therefore weaken the bond. Conversely, if the antibonding states are less filled, the bond will be strengthened.

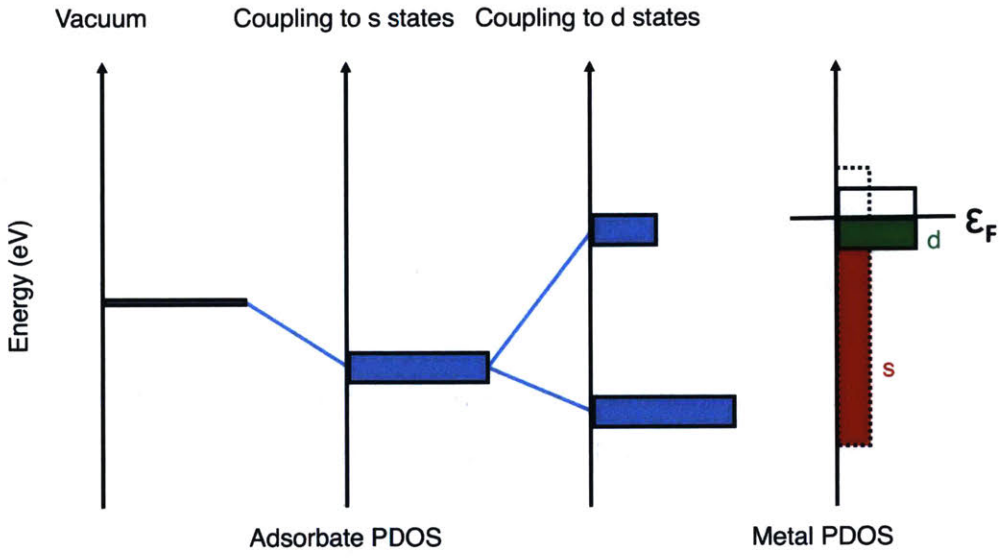

Figure 2-1: Adsorbate-metal bond formation schematics. Adsorbate valence bands are shown in blue, metal s bands are shown in red and metal d bands are shown in green. The filling of the antibonding state of the adsorbate-metal bonds determines the bond strength. The higher the d-band level of the metal relative to the Fermi level, the less filled the antibonding levels and the stronger the bond. Adapted from Reference [1].

It is therefore evident that the filling of the antibonding states largely depend on

the position of the d-band. Since the antibonding states are always above the d-states, the higher the position of the d-band, the higher the position of the antibonding states are relative to the Fermi level and therefore the stronger the bond due to less filling of these antibonding states. In computational catalysis literature, a convenient indicator for the position of the d band is called the d-band center, which is the energy weighted average of the density of the d states.

One thing to note though is that as with all rules, exceptions do exist. When electronegative adsorbates with almost completely filled valence shell interact with metals with almost full d bands, the repulsion between the electrons will lead to a reversal of the d-band model's predicted trend [65]. In this study, we did not apply the d-band model to the absorbates that are exceptions to the rule and therefore can safely assume the validity of the model on the systems we studied. As for the accuracy of the calculated results, we corroborated our data with experimental evidence whenever the model was employed.

2.1.2 Activity Volcanoes

To relate adsorption energies to the performance of a catalyst, one has to find a relationship that describes how adsorption energies of reaction intermediates are related to the overall reaction energy. The French chemist Paul Sabatier proposed that the optimal catalyst of a reaction should be one that does not bind reactants too strongly because that would lead to poisoning which results in a catalyst surface completely covered by species that do not desorb. The surface also should not bind the reactants too weakly as the reactions would not proceed if reactants do not bind [66]. This relationship is represented in Figure 2-2. Catalysts on the left (yellow) leg of the activity volcano (represented by the black triangle) bind the reactants too strongly, therefore the reaction is limited by desorption that releases the products. On the other hand, catalysts on the right leg (purple) of the activity volcano bind reactants too weakly, therefore the reaction is limited by the binding of reactants to the catalytic surface. The optimal catalyst lies in the red rectangle which binds the reactants just right for the best reaction rate.

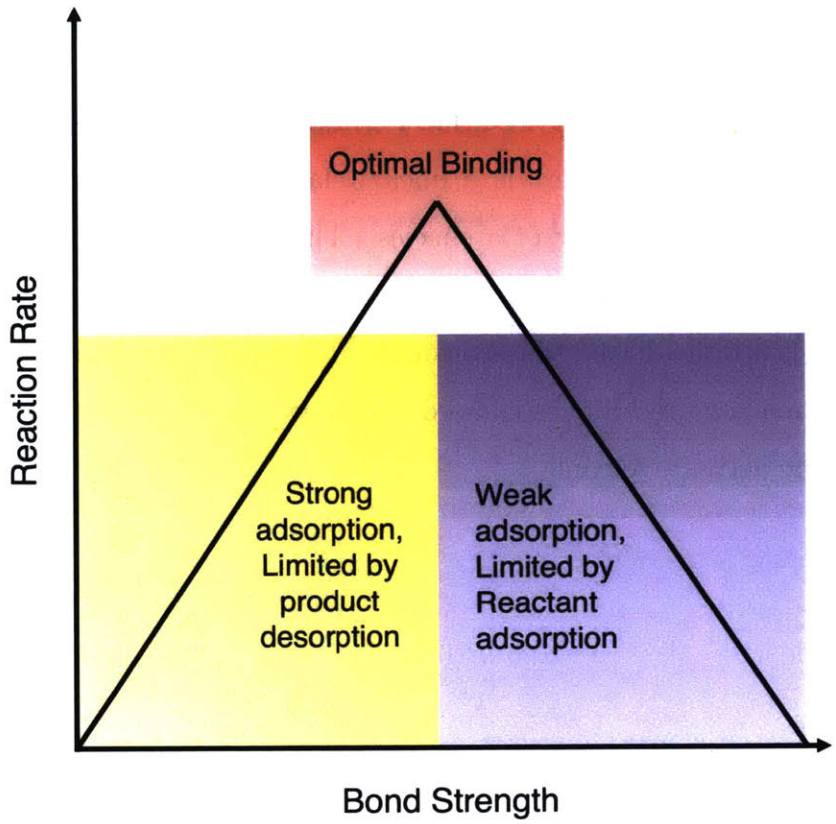

Figure 2-2: Schematic representation of the Sabatier principle. The Yellow rectangle shows reactants that bind too strongly (more negative bond strength indicates stronger binding). The purple rectangle shows reactants that binds too weakly. The peak of the volcano in the red region is where the optimal catalyst lies.

The task now is to find a suitable thermodynamic property that describes 'bond strength'. Since the reaction rate depends both on the thermodynamic binding strengths of the reactants and the kinetic activation barriers at the rate-limiting steps, it is not straightforward to determine one property that could stand in for bond strength. To simplify the situation, we can utilize the Brønsted-Evans-Polanyi (BEP) relationship [67, 68] as substantial evidence supports its validity for surface reactions such as those considered in this thesis [69–74]. Essentially, this relationship relates the activation energy of a reaction to enthalpy of the reaction with the equation:

$$E_a = \beta + \alpha E_{ads} \tag{2.2}$$

where E_a is the activation energy of the reaction, α and β are constants to be determined for a particular species of a particular reaction, and E_{ads} is the adsorption energy of that species on the catalytic surface. This means that for a system in which the BEP relationship applies, there is a linear relationship between the activation energy and the adsorption energy of a species. Therefore, one can use E_{ads} as an indicator of bond strength.

Obtaining E_{ads} is difficult and time-consuming for experimentalists. This is where computational chemistry techniques can aid and speed up the identification of catalysts on top of the activity volcano.

2.2 Density Functional Theory

Density Functional Theory is one of the most popular tools in computational chemistry due to its balance of computational cost and accuracy. To illustrate this, we must first begin with the time-independent, non-relativistic Schrödinger's equation:

$$\hat{H}\Psi_i(\vec{x}_1, \vec{x}_2, ...\vec{x}_N, \vec{R}_1, \vec{R}_2, ...\vec{R}_M) = E_i\Psi_i(\vec{x}_1, \vec{x}_2, ...\vec{x}_N, \vec{R}_1, \vec{R}_2, ...\vec{R}_M) \tag{2.3}$$

where $\hat{H}$ is the Hamiltonian for a system of M nuclei and N electrons:

$$\hat{H} = -\frac{1}{2}\sum_{i=1}^{N}\nabla_i^2 - \frac{1}{2}\sum_{A=1}^{M}\frac{1}{M_A}\nabla_A^2 - \sum_{i=1}^{N}\sum_{A=1}^{M}\frac{Z_A}{r_{iA}} + \sum_{i=1}^{N}\sum_{j>i}^{N}\frac{1}{r_{ij}} + \sum_{A=1}^{M}\sum_{B>A}^{M}\frac{Z_A Z_B}{R_{AB}} \tag{2.4}$$

In the Hamiltonian, M_A is the nuclear mass and Z_A is the atomic number. The first term describe the kinetic energies of the N electrons and the second term describe the kinetic energies of the M nuclei. The third term describes the attractive electrostatic interaction between the electrons and the nuclei. The fourth term accounts for the repulsive interactions between the electrons while the fifth term describes the repulsive interactions between the nuclei.

A first attempt in simplifying the solution is to introduce the Born-Oppenheimer Approximation [75]. Since nuclei are significantly heavier than electrons, they move extremely slowly as compared to electrons. Therefore, we can approximate the system as electrons moving in a field of fixed nuclei. Under this approximation, the second term in the Hamiltonian is reduced to zero as the kinetic energy of the nuclei can be ignored. In addition, the repulsive potential introduced by nucleus-nucleus interaction, which is the last term of the Hamiltonian becomes a constant. We can therefore write down the electronic Hamiltonian as:

$$\hat{H}_{elec} = -\frac{1}{2}\sum_{i=1}^{N}\nabla_i^2 - \sum_{i=1}^{N}\sum_{A=1}^{M}\frac{Z_A}{r_i A} + \sum_{i=1}^{N}\sum_{j>i}^{N}\frac{1}{r_{ij}} = \hat{T} + \hat{V}_{Ne} + \hat{V}_{ee} \tag{2.5}$$

We can then divide the energy of the whole atomic system into two components,

an electronic contribution and a nucleic contribution:

$$E_{tot} = E_{elec} + E_{nuc} \tag{2.6}$$

For the E_{elec} part, the Schrödinger's equation has Ψ_{elec} as the electronic wave function:

$$\hat{H}\Psi_{elec} = E_{elec}\Psi_{elec} \tag{2.7}$$

We define the Coulomb potential arising from nuclear-electron interaction $\hat{V}_{Ne}$ as a static external potential $\hat{V}_{ext}$ and the rest of the $\hat{H}_{elec}$ as $\hat{F}$ such that:

$$\hat{V}_{ext} = \hat{V}_{Ne} \tag{2.8}$$

$$\hat{F} = \hat{T} + \hat{V}_{ee} \tag{2.9}$$

$$\hat{H}_{elec} = \hat{V}_{ext} + \hat{F} \tag{2.10}$$

Since $\hat{F}$ does not vary for all N-electron systems, the ground state Ψ_0 can be completely determined by N and $\hat{V}_{ext}$. The electron density associated with Ψ_0 is:

$$n_0(r) = \langle\Psi_0|\hat{n}|\Psi_0\rangle = \int \prod_{i=2}^{N} dr_i \mid (\Psi_0(r, r_2, \ldots r_N)) \mid^2 \tag{2.11}$$

It can be seen here that the ground-state electron density $n_0(r)$ is also a functional of N and $\hat{V}_{ext}$. Hohenberg and Kohn postulated two statements that became the foundation of Density Functional Theory: The external potential $\hat{V}_{ext}$ is uniquely determined by the ground-state electron density and that the ground-state energy can be obtained variationally by finding the density (the ground-state density) that minimizes the total energy of the system [76, 77].

To prove the first theorem, we can assume there are two external potentials that map to the same electron density, $n_0(r)$. Assuming these two external potential corresponds to two ground-state wave functions $|\Psi_0\rangle$ and $|\Psi_0'\rangle$. We can thus write

down two ground-state energies:

$$E_0 = \langle \Psi_0 | \hat{H} | \Psi_0 \rangle \tag{2.12}$$

$$E_0' = \langle \Psi_0' | \hat{H}' | \Psi_0' \rangle \tag{2.13}$$

If we instead apply $\hat{H}$ to $|\Psi_0'\rangle$ and $\hat{H}'$ to $|\Psi_0\rangle$, the Varionational Principle stipulates that the energy we obtained will be higher than the ground-state energy obtained by applying Hamiltonian to its corresponding ground-state wave function:

$$E_0 < \langle \Psi_0' | \hat{H} | \Psi_0' \rangle \tag{2.14}$$

$$E_0' < \langle \Psi_0 | \hat{H}' | \Psi_0 \rangle \tag{2.15}$$

A series of algebraic manipulations of Equation 2.15 and Equation 2.14 would arrive at the contradicting result of:

$$E_0' + E_0 < E_0' + E_0 \tag{2.16}$$

which proves that an external potential is uniquely determined by its corresponding ground-state electron density.

This result has a few implications. Firstly, we can say that the ground-state electron density determines the $\hat{V}_{ext}$ of its corresponding $\hat{H}$. Since $\hat{V}_{ext}$ and N determine $\hat{H}$ and the ground-state wave function $|\Psi_0\rangle$, they determine all ground state properties of the system. For a ground-state density $n(r)$, since it determines $\hat{V}_{ext}$ and N, we can say it also has a uniquely defined $F[n] = \langle \Psi | \hat{F} | \Psi \rangle$. We can then write a functional $E_v[n]$ which is a sum of $F[n]$ and some arbitrary external potential $V(r)$:

$$E_V[n] = F[n] + \int dr V(r) n(r) \tag{2.17}$$

With $E_V[n]$ defined we can now move on to the second statement - for N electrons in the external potential $V(r)$ that has the ground-state energy E_0, $E_v[n] \geq E_0$. To

prove this, we use $|\Psi\rangle$ that is determined by $n(r)$ with its corresponding external potential $\hat{V}_{ext}$ as a trial state for:

$$\langle\Psi|\hat{H}|\Psi\rangle = \langle\Psi|\hat{F}|\Psi\rangle + \langle\Psi|\hat{V}|\Psi\rangle = F[n] + \int drV(r)n(r) = E_V[n] \geq E_0 \quad (2.18)$$

by variational principle. Only when $|\Psi\rangle$ is a ground-state for potential $V(r)$ does the equality hold.

We define a functional that takes the minimum value of the expectation value with respect to $|\Psi\rangle$ which give the density n_r:

$$F[n] = \min_{|\Psi\rangle\to n} \langle\Psi|\hat{F}|\Psi\rangle \quad (2.19)$$

We also define $E_V[n]$ for a state $|\Psi\rangle_{[n]}$ as:

$$E_V[n] = \left\langle\Psi_{[n]}\middle|\hat{F} + \hat{V}_{ext}\middle|\Psi_{[n]}\right\rangle \quad (2.20)$$

According to variational principle, we have:

$$E_V[n] \geq E_0 \quad (2.21)$$

where the equality holds only if $|\Psi_n\rangle = |\Psi_0\rangle$.

For the ground-state density n_0 we can write down:

$$F[n_0] \leq \langle\Psi_0|\hat{F}|\Psi_0\rangle \quad (2.22)$$

by definition.

Therefore,

$$E_V[n_0] \geq E_0 \quad (2.23)$$

and

$$E_V[n] \geq E_V[n_0] = E_0 \quad (2.24)$$

which means $E_V[n]$ is minimized by n_0 and that minimum is when $E_V[n] = E_0$.

Though we have defined $F[n]$, its exact form is unknown. To simplify the task of finding $F[n]$, Kohn and Sham reformulated the problem by mapping a system of interacting electrons to one that has non-interacting electrons [77]. This formulation divide $F[n]$ into three parts - the kinetic energy of the non-interacting system with the electron density $n(r)$, the classical electrostatic energy and a final term that takes into account all non-classical interactions as well as the difference in kinetic energy between the non-interacting system and the interacting system:

$$F[n] = T_{non-interacting}[n] + \frac{1}{2}\int drdr' \frac{n(r)n(r')}{|r-r'|} + E_{xc}[n] \tag{2.25}$$

By mapping the interacting electrons onto non-interacting electron orbitals, the size of the total wave function of a system now scales linearly with N rather than the N^{th} power where N is the number of electrons in the system. The only elusive part of the Kohn-Sham formulation of $F[n]$ is the $E_{xc}[n]$ term. The simplest approximation, the local density approximation (LDA) of $E_{xc}[n]$, is to treat the electron density as being uniform in space. One level up in complexity is the generalized gradient approximation (GGA) where the local gradient of the electron density is also taken into consideration. There is also meta-GGA which further adds non-interacting kinetic energy density to the electron density and its gradient.

In this thesis, the GGA functional revised-Perdew-Burke-Ernzerhof (RPBE) [78] is chosen because it is one of the best functionals in obtaining catalytic energies among GGA functionals [79] with an AECE (Average Error for Catalytic Energies)of 0.28 eV [79]. Since RPBE is a functional especially tested for atoms and small molecules adsorption on transition metal surfaces against experimental data, it is suitable for the system studied. In addition, we are deriving trends by comparing adsorption energies on different surfaces for the same substrates or vice versa instead of making claims based on the exact value calculated adsorption energies, we expect a degree of systemic error cancellation.

2.3 Simulating Periodic Systems

In a solid state system, simulating one cubic millimeter of materials requires one to account for number of atoms on the order of 10^{20}, and even more electrons, which is vastly expensive given current computational infrastructure available. Even though we have reduced the computational cost drastically thanks to the Hohenber-Kohn-Sham formulation of DFT, we need to exploit properties of solid state systems that differ from atoms or molecules to further reduce the computational load.

In crystalline systems, the material is periodic in nature thanks to crystal symmetries. This periodicity allows computational materials scientists to simulate unit cells that repeat in space with periodic boundary conditions.

To understand this, we start with Bloch's theorem [80]. In a perfect crystal in which atoms are arranged periodically according to Bravais lattice vectors, the system is invariant under translation along these vectors. The potential therefore, is also periodic for all Bravais lattice vectors (R):

$$V(r+R) = V(r) \tag{2.26}$$

We can define a translation operator $\hat{T}_R$ for lattice vector R such that:

$$\hat{T}_R f(r) = f(r+R) \tag{2.27}$$

Applying this operator to Schrödinger's equation we have:

$$\hat{T}_R \hat{H}(r)\psi(r) = \hat{H}(r+R)\psi(r+R) = \hat{H}(r)\hat{T}_R\psi(r) \tag{2.28}$$

which shows that $\hat{T}_R$ and $\hat{H}$ are commutable and the translation operators commute with each other:

$$\hat{T}_R\hat{T}_{R'} = \hat{T}_{R'}\hat{T}_R = \hat{T}_{R+R'} \tag{2.29}$$

Therefore, we can find states that are simultaneous eigenstates of both the Hamilto-

nian and the translation operator:

$$\hat{H}\,|\psi\rangle = E\,|\psi\rangle \tag{2.30}$$

$$\hat{T}_R\,|\psi\rangle = c(R)\,|\psi\rangle \tag{2.31}$$

For a set of 3 primitive lattice vectors $\{a_i\}$, we can rewrite:

$$c(a_i) = e^{2\pi i x_i} \tag{2.32}$$

Any R can be decomposed into a linear combination of the 3 primitive lattice vectors and therefore:

$$c(R) = e^{ik\cdot R} \tag{2.33}$$

where

$$k = x_1 g_1 + x_2 g_2 + x_3 g_3 \tag{2.34}$$

and g_i is the reciprocal lattice vector that satisfies $g_i \cdot a_i = 2\pi\delta_{ij}$. We can then write:

$$\hat{T}_R\psi(r) = \psi(r+R) = c(R)\psi(r) = e^{ik\cdot R}\psi(r) \tag{2.35}$$

which states Bloch's theorem.

We consider the periodic function $u(r)$ that satisfies:

$$\psi(r) = e^{ik\cdot r}u(r) \tag{2.36}$$

We can then show that $u(r)$ satisfies

$$u(r+R) = u(r) \tag{2.37}$$

If we express $u(r)$ as a Fourier series, we have:

$$u(r) = \sum_G \tilde{u}_G e^{iG\cdot r} \tag{2.38}$$

where G is the reciprocal lattice vector, we can then express the eigenstates of the Hamiltonian and the translation operators, $|\psi\rangle_{nk}$, as:

$$\psi_{nk} = e^{ik\cdot r}u_{nk}(r) = \sum_{G} c_{nk}(G)e^{i(k+G)\cdot r} \tag{2.39}$$

Therefore, we can limit ourselves to solving for the wave function in s single cell over many ks instead of over all space. These wave functions make up a plane wave basis set. The indexing of ψ_{nk} is such that n is called the band index which is of the order of the number of electrons per unit cell and k is a Bloch vector which lies usually within the first Brillouin zone of the reciprocal space lattice. In practice, we limit the number of ks with a kinetic energy cutoff defined by:

$$\frac{1}{2}|G+k|^2 < E_{cutoff} \tag{2.40}$$

2.4 Pseudopotentials

To describe strongly localized states and the nodal structures near the nucleus, we need a particularly large number of plane waves (large k cutoff). To address this, we use a frozen core approximation. The rationale behind this approximation is that since core electrons do not participate in interatomic interactions, they can be represented by a pre-calculated potential that is kept frozen during the simulation. We then adopt pseudopentials - these potentials use nodeless effective potentials to model core electrons but retain the nodal structures of the valence electrons. Beyond a cutoff distance from the nucleus, these potential match the exact potential, which ensures the accurate modeling of interatomic interactions. The particular type of pseudopotential employed in this thesis is called the Projector-Augmented-Wave (PAW) method [81]. In this method, the wave function is decomposed as:

$$|\psi_n\rangle = \left|\tilde{\psi}_n\right\rangle - \sum_i (|\phi_i\rangle - \left|\tilde{\phi}_i\right\rangle) \left\langle \tilde{p}_i \middle| \tilde{\psi}_n \right\rangle \tag{2.41}$$

where $\left|\tilde{\psi}_n\right\rangle$ is the pseudo wave function, $|\phi_i\rangle$ is the all-electron partial waves from radially integrating the Schrödinger's equation up to within an augmented region close to the nucleus, $\left|\tilde{\phi}_i\right\rangle$ is the pseudo wave function within the augmented region and $\tilde{p}_i$ is a projector function for each pseudo wave function within the augmented region that satisfies $\left\langle \tilde{p}_i \middle| \tilde{\psi}_n \right\rangle = \delta_{ij}$. Essentially, to describe the region close to the atomic radius, we subtract the pseudo wave within that region and add back an all-electron wave which describes the region more accurately capturing nodal features. The package we used which implements PAW pseudopotentials is called Vienna Ab initio Simulation Package (VASP) [82]. It has been widely used in the simulation of adsorption energies and catalysis [83–85]. In addition, as it is a commercial package with a large and well-maintained pseudopotential library, as well as stable performance, it is chosen as the DFT tool for this thesis. A final note here on the implementation of DFT - the variation among different solution methods, be it all-electron or pseudized is smaller than the variation among high precision experimnets for solid properties according

to the most recent benchmarking in Science [86]. For VASP [82] in particular, its average deviation from all-electron methods is 0.0006 eV per atom.

Chapter 3

Electronic Origin and Kinetic Feasibility of Lattice Oxygen Participation During the Oxygen Evolution Reaction on Perovskites

Parts of this chapter has been published in the following two papers that I co-authored [87] [88] with Dr. Jong Suk Yoo, Dr. Xi Rong and Prof. Alexie Kolpak.

3.1 Introduction

In order to transition from using fossil fuels as a main source of energy to more sustainable energy forms, alternative sources of energy with cheap and efficient production need to be identified. Hydrogen is one such candidate as its combustion in oxygen produces only water, with no harmful environmental consequences. The electrochemical splitting of water the cleanest way of producing hydrogen as compared to approaches that are still carbon-based such as steam-methane reforming [89–93]. In addition, this reaction is highly valuable for energy storage applications that can tackle the intermittent nature of renewable sources like wind and solar. The oxygen evolution reaction (OER) is the kinetic bottleneck of the reaction and the quest to find a cheap, highly active as well as stable electrocatalyst for OER has been challenging [94–97].

Perovskite oxides of the general form ABO_3 where A is a rare-earth element and B is a transition metal have shown great promise as electrocatalysts for water splitting [97–100]. For OER, perovskites demonstrate better performance than the more expensive IrO_2, which has one of the highest known activities for OER to date. Theoretical studies on the catalytic abilities of different combinations of A and B have led to not only the discovery of new catalysts but also reaction mechanisms [101–103]. One mechanism is the adsorbate evolution mechanism (AEM), in which the adsorbate is sequentially oxidized via

$$OH* \rightarrow O* \rightarrow OOH* \rightarrow O_2(g) \tag{3.1}$$

This mechanism is favorable for strongly binding perovskites such as $LaCoO_3$, while the newly proposed lattice oxygen mechanism (LOM), in which the surface lattice oxygen (O_{surf}) participates in the reaction, is favorable for weakly binding perovskites such as $LaCuO_3$ [102,103]. A comparison of the mechanisms on an example perovskite $LaNiO_3$ is shown in Figure 3-1.

My co-authors and I have demonstrated that the ideal perovskite with the lowest overpotential requires O_{surf} participation as the peak of the activity volcano for LOM has been shown to be higher than that for AEM [88]. This is because, in the case of

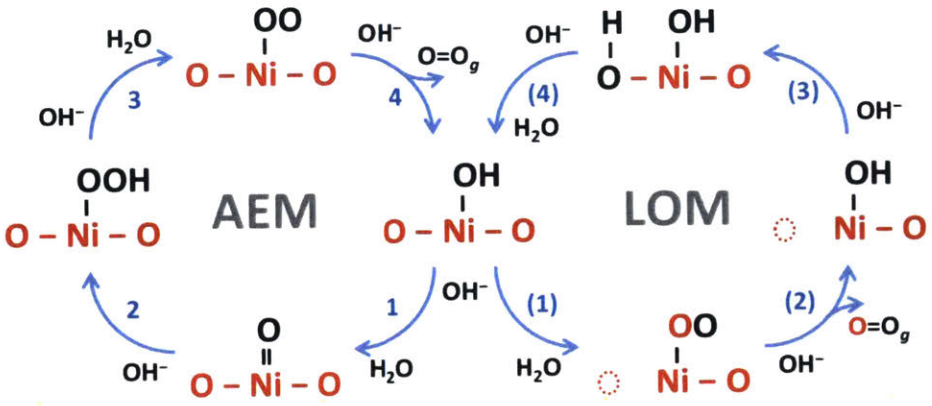

Figure 3-1: The illustration of the four charge transfer steps involved in AEM and LOM over the NiO_2 terminated $LaNiO_3(001)$ surface covered with OH*. Note the divergence shown in step 1 and (1), where in 1, the adsorbed OH* is oxidized to a O* double-bonded to the surface while in (1), one oxygen comes out of the catalyst (red) to form OO*. Please refer to Figure 3-5 for a model of the catalytic surface.

AEM, the free energy ΔG for OH* $\rightarrow$ OOH* has a constant value of 3.1 eV, which is 0.64 eV away from the ideal value of 2.46 eV (= 1.23 eV/step for 2 steps), therefore, the smallest overpotential possible for AEM is 0.32 V (= 0.64 eV/2e). On the other hand, in the case of LOM, ΔG for V_o + OO* $\rightarrow$ V_o + OH* has a constant value of 1.4 eV, which is 0.17 eV away from the ideal value of 1.23 eV, therefore, the smallest overpotential possible for LOM is 0.17 V (= 0.17 eV/e) [88] (Figure 3-2).

This new mechanism was able to corroborate experimental results that contradicted the predictions given by the consensus AEM mechanism. For example, Petrie et al. [104] recently found that compressive strains as small as -1.2% can improve the OER activity of $LaNiO_3$, while tensile strains of up to +2.7% have the opposite effect. To explain the experimental results with our theoretical study, we have obtained the values of oxygen adsorption energies on various strained $LaNiO_3$ surfaces, and the predicted overpotentials are shown by the overall OER activity volcano plot in Figure 3-3b. Interestingly, we find that compressive strain gradually weakens oxygen adsorption energies on $LaNiO_3$, whereas tensile strain significantly strengthens it. As a result, $LaNiO_3$ with a compressive strain of -4.0% has the lowest overpotential of

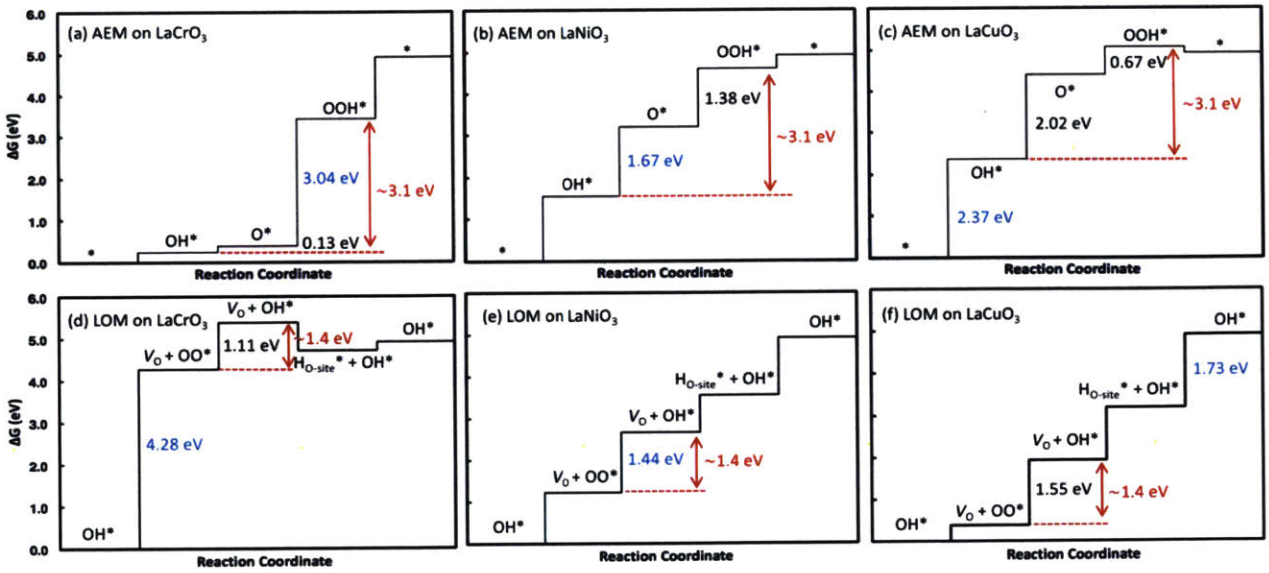

Figure 3-2: Free energy diagrams for OER via AEM for (a) $LaCrO_3$, (b) $LaNiO_3$, (c) $LaCuO_3$, and via LOM for (d) $LaCrO_3$, (e) $LaNiO_3$, (f) $LaCuO_3$ at pH = 0, T = 298 K, and zero applied potential (U = 0 V vs RHE). All adsorbates with * bind to the transition metal site of ABO_3 (001) except $H_{O\text{-site}}$*, which binds to the lattice-oxygen site. In each plot, the value of the reaction free energy for the potential-determining step (namely, the limiting potential) is shown in blue. The red arrows in (a), (b), and (c) show that ΔG_{OOH} - ΔG_{OH} is relatively constant for AEM, with an average value of 3.1 eV, whereas those in (d), (e), and (f) show that ΔG_{V_O+OH} - ΔG_{V_O+OO} is relatively constant for LOM, with an average value of 1.4 eV

0.1 V, which is 0.1 V lower than that of strain-free $LaNiO_3$. Thus, our overall volcano successfully corroborates the experimental trend toward enhanced OER activity with compressive strain on $LaNiO_3$. On the other hand, if we considered only the AEM volcano shown as black lines in Figure 3-3b, we cannot explain the strain-induced effect observed on $LaNiO_3$, as the AEM volcano gives the opposite trend, with tensile strain of +1.0% improving the OER activity of $LaNiO_3$ and any compressive strain worsening it.

In addition, experiments employing in situ ^{18}O isotope labeling showed that the O_2 gas produced during OER on highly active perovskites such as $La_{1-x}Sr_xCoO_{3-\delta}$ and $SrCoO_{3-\delta}$, contains the lattice oxygen from the perovskites [101].

However, questions remain as to (1) a detailed understanding of the reaction pathway through which O_{surf} participates in OER, (2) an explanation for different

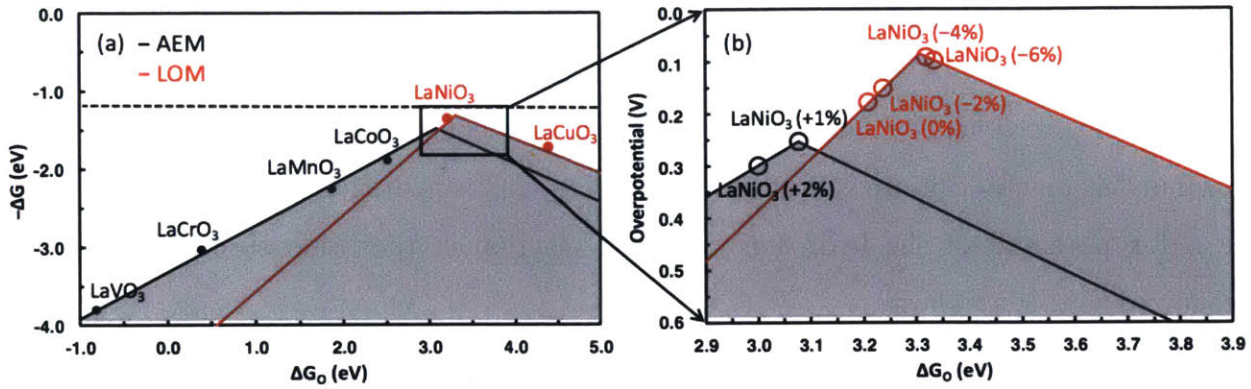

Figure 3-3: The shaded region in (a) shows the overall OER activity volcano that takes into account both AEM (black) and LOM (red). The dashed line in (a) indicates the equilibrium potential for OER (1.23 V). (b) Theoretical overpotential (= equilibrium potential limiting potential) vs. oxygen adsorption energy for the region shown as the black box in (a). Filled markers in (a) indicate the data points used to construct the volcano based on calculations of the reaction energetics. Empty markers in (b) indicate those added to the constructed volcano by calculating oxygen adsorption energy per surface. They are $LaNiO_3$ surfaces with either tensile (+) or compressive (-) strain relative to the lattice parameters of pristine $LaNiO_3$.

thermodynamic driving forces of O_{surf} participation on different perovskites, (3) the competition between O_{surf} participation and O_{surf} protonation that prevents O_{surf} from leaving the perovskite surface, and (4) the feasibility of LOM under the OER (oxidizing) condition that accounts for both the adsorbate-coverage and solvent effects. These effects are of particular importance when determining the mechanism on moderately binding perovskites where AEM and LOM can compete closely. In this chapter, we employ DFT to answer these questions. Theoretical insights gained from this chapter provide a detailed understanding of LOM and provides guidelines for the design of new perovskite catalysts that can react via LOM.

3.2 Computational Details

In this thesis, free energy relations follow conventions defined in [5] except potential shown in this manuscript are values versus RHE (reversible hydrogen electrode) when the redox potential of the hydrogen evolution reaction in the same electrolyte is recognized as the standard.

In this study we employ three model perovskite systems - the highly active $LaNiO_3(001)$ as an example for moderately binding perovskites with an oxygen adsorption energy of 3.21 eV relative to H_2O and H_2, $LaCoO_3(001)$ with an oxygen adsorption energy of 2.46 eV relative to H_2O and H_2 for strongly binding perovskites that prefer AEM to LOM, and $LaCuO_3(001)$ with an oxygen adsorption energy of 4.38 eV relative to H_2O and H_2 for weakly binding perovskites that prefer LOM to AEM. The (001) surface plane is chosen for its stability [105, 106] and experimental availability [107–110].

Spin-polarized calculations were performed using VASP [82], employing the PAW [111] pseudopotentials with the RPBE [78] functional. We chose the Fast algorithm, Accurate precision, and $4 \times 4 \times 1$ Monkhorst-Pack [112] k-point mesh for all calculations with the energy cutoff of 500 eV and Gaussian smearing of 0.1 eV. The periodic slab model for the MO_2 terminated $LaMO_3$ (M = Ni, Co, and Cu) (001) surface was built from the bulk cubic phase using a $2 \times 2 \times 4$ supercell. The periodic slab models were separated by more than 17 AA of vacuum perpendicular to the surface plane. The top two oxide layers of the slab models as well as the adsorbates were allowed to relax until the forces on the individual relaxed atoms were less than 0.001 eV per Å.

All adsorption energies were calculated in the low coverage limit of $\frac{1}{4}$ (i.e., one of the four surface nickel atom has a *OH adsorbed on it), unless noted otherwise, and they were all referenced to gas-phase H_2O and H_2. The projected density of states were calculated using a denser $12 \times 12 \times 1$ Monkhorst-Pack k-point mesh for higher accuracy.

Bader-charge analysis was conducted using the grid-based algorithm [113–116]. The activation barriers were determined using the climbing image nudged elastic band (CI-NEB) method [117, 118]. The solvation effects were investigated using the

VASPsol [119, 120] patch that implements the continuum solvation model with the dielectric constant of water. The reaction free energies were determined using the following equation: $\Delta G = (\Delta E + \Delta ZPE - T\Delta S)_{vac} - eU_{RHE} + \Delta H_{sol}$. $U_{RHE} = 0$ for non-electrochemical reactions. The zero-point-energy (ΔZPE) and entropic ($T\Delta S$) corrections were determined for $LaNiO_3$, and were used for all perovskites. These corrections are shown in Table 3.1. The calculated solvation energy ΔH_{sol} values for different reaction intermediates on $LaNiO_3$ are shown in Table 3.2. Finally, we also considered $2 \times 2 \times 7$ supercells with identical surface terminations on both sides of the slab models (thus, non-polar in z direction) in calculating adsorption energies, and found that the results are similar to those obtained with $2 \times 2 \times 4$.

Species	ΔZPE	$T\Delta S$	$\Delta ZPE - T\Delta S$	$\Delta(ZPE - TS)$
H_2O(l)	0.57	0.67	-0.10	–
H_2(g)	0.28	0.40	-0.12	–
-OH	0.34	0.11	0.23	0.27
-O (I_0)	0.07	0.06	0.01	-0.01
-O (I_1)	0.08	0.04	0.04	0.02
-O (TS for $I_0 \rightarrow I_1$)	0.05	0.03	0.02	0.00
-OOH	0.43	0.28	0.15	0.17
-OO	0.13	0.14	-0.01	-0.05
-OO (V_O) (I_2 and I_3)	0.13	0.14	-0.01	-0.03
-OO (V_O) ($I_{3\text{-}1}$)	0.11	0.17	-0.06	-0.08
-OO (V_O) (TS for $I_1 \rightarrow I_2$)	0.11	0.08	0.03	0.01
-OO (V_O) (TS for $I_1 \rightarrow I_{3\text{-}1}$)	0.10	0.15	-0.05	-0.07
-H	0.32	0.10	0.22	0.28

Table 3.1: Zero-point-energy and entropic corrections (in eV) obtained for different adsorbates involved in OER. They are obtained for $LaNiO_3$ but are used independent of the perovskite.

Species	$\Delta H_{sol-species}$	ΔH_{sol}
Clean	-0.19	–
-OH	-0.30	-0.11
-O	-0.15	0.04
-OOH	-0.40	-0.21
-OO	-0.11	0.08
-OO (V_O)	-0.15	0.04

Table 3.2: Enthalpy difference per site between intermediates in vacuum (dielectric constant=0) and water solvent (dielectric constant=78.4), denoted as $\Delta H_{sol-species}$, ΔH_{sol} denotes with respect to the clean surface.

3.3 Results and Analysis

3.3.1 Kinetic Feasibility of Lattice Oxygen Diffusion

As Figure 3-1 shows, the four charge-transfer (electrochemical) steps involved in AEM [5,121] vs. LOM [88,99,101,103,122] diverge at step 1 when a lattice oxygen diffuses out of the perovskite. The detailed reaction pathways possible for O_{surf} participation, i.e., step (1) in LOM is illustrated in Figure 3-4. We can see that O_{surf} participation may include step 1 in AEM ($I \rightarrow I_0$) depending on the stability of I_0 relative to I_1, and then requires additional non-electrochemical steps such as O* diffusion from Ni_{surf} to O_{surf} ($I_0 \rightarrow I_1$), followed by Ni_{surf}-O_{surf} bond cleavage to form OO* bound to Ni_{surf} via the original O* atom and a surface oxygen vacancy (V_O) ($I_1 \rightarrow I_2$) or the cleavages of both the Ni_{surf}-O_{surf} and Ni_{surf}-O* bonds to form OO* bound to Ni_{surf} via the original O_{surf} atom and V_O ($I_1 \rightarrow I_{3\text{-}1} \rightarrow I_3$). Thus, it is essential to first study the kinetic feasibility of all the non-electrochemical steps involved in O_{surf} participation before comparing the thermodynamics of the four charge-transfer steps involved in AEM vs. LOM, to determine which mechanism is more favorable for a particular perovskite. A detailed scheme of all the reaction intermediates shown in Figure 3-4 is presented in Figure 3-5.

Figure 3-6 shows the calculated reaction energetics of $I_0 \rightarrow I_1 \rightarrow I_{2/3}$ over MO_2 terminated $LaMO_3(001)$ (M = Ni, Co, and Cu). Note that $I_0 \rightarrow I_1$ does not denote an actual reaction but whether I will form I_0 or I_1 depending on which position of

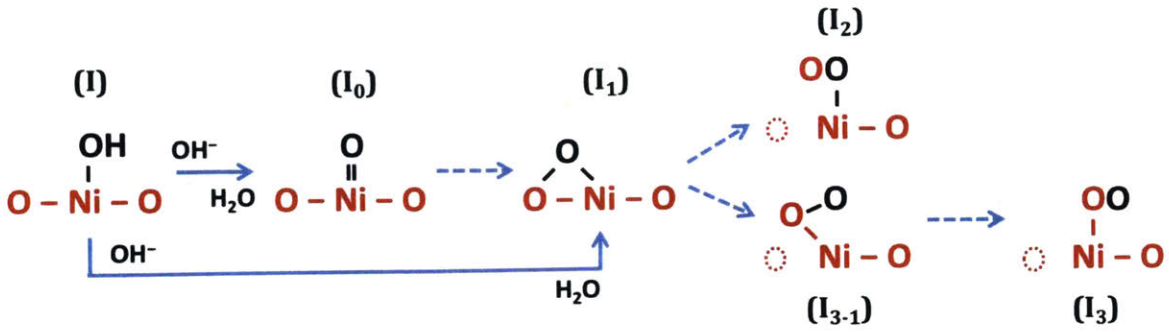

Figure 3-4: The detailed reaction pathways possible for O_{surf} participation, i.e., step (1) in LOM. Solid arrows indicate electrochemical steps that involve charge transfers from the water solvent, dashed arrows indicate non-electrochemical steps that involve only adsorbates and the surface lattice oxygen (O_{surf}).

the adsorbed oxygen is more stable. Interestingly, we can see the final state ($I_{2/3}$) is significantly more stable than the initial state (I_0) by 2.2 eV and 1.0 eV for $LaCuO_3$ and $LaNiO_3$, respectively, whereas it is conversely less stable by 0.5 eV for $LaCoO_3$. This can be explained considering the change in the oxidation state of the surface M site (M_{surf}) between the two states. We find that O* in I_0 binds to M_{surf} with a double bond character as indicated by e.g. the Ni_{surf}-O* bond length of 1.68 Å, which is noticeably shorter than the Ni-O single bond length of 1.93 Å in bulk LaNiO3. This indicates the oxidation state of M_{surf} of I_0 would be slightly more positive than the nominal charge of M^{3+} in bulk $LaMO_3$. On the other hand, OO* in $I_{2/3}$ binds to M_{surf} with a single bond character as indicated by e.g. the Ni_{surf}-OO* bond length of 1.93 Å. This indicates the oxidation state of M_{surf} of $I_{2/3}$ would be fairly close to the nominal charge of M^{3+} in bulk $LaMO_3$.

Bader charge analysis further confirms that I_1 and $I_{2/3}$ of $LaNiO_3$ and $LaCuO_3$ have oxidation states much closer to bulk M^{3+} than I_0 (Figure 3-7). Since late transition metals such as Cu and Ni are electronegative (χ = 1.90 and 1.91 by Pauling scale [123]), and therefore have large fourth ionization energies [124] (IE = 57 eV and 55 eV), compared to early transition metals such as Co (χ = 1.88 by, and IE =

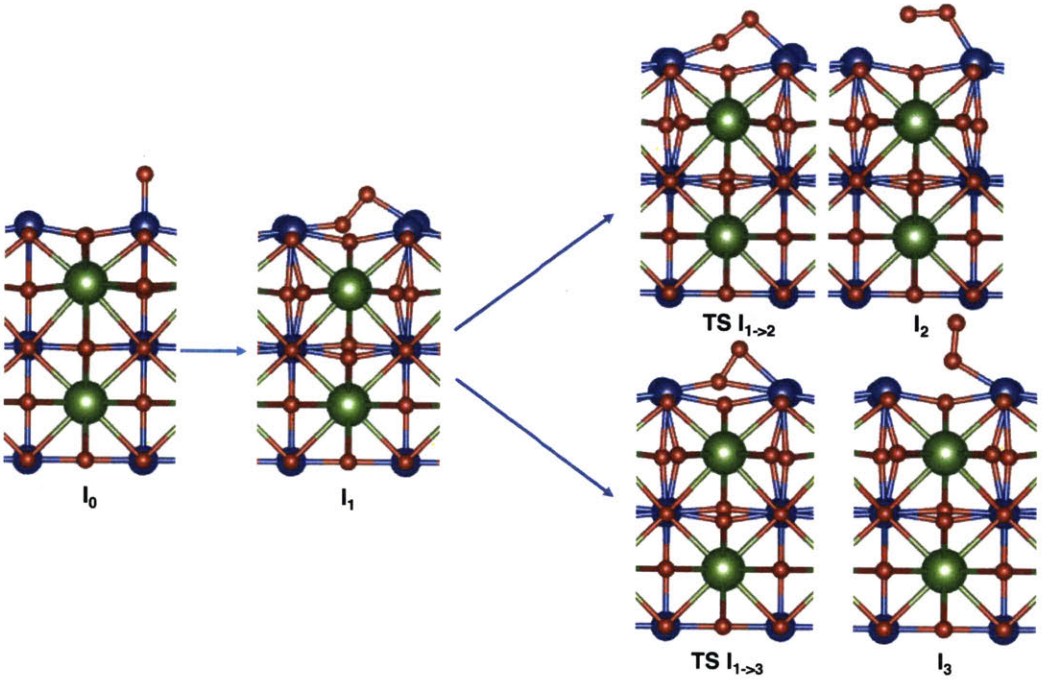

Figure 3-5: Illustrations of structures of reaction intermediates for $LaMO_3$ in non-electrochemical steps of LOM. The structures are optimized at surface coverage. TS indicates transition states. The optimized structures here are for $LaCuO_3$.

51 eV), it is not surprising to find $M^{(3+\delta)+}$ (I_0) being less stable than M^{3+} ($I_{2/3}$) for $LaCuO_3 > LaNiO_3 > LaCoO_3$.

Figure 3-6 indicates that O* is more stable on M_{surf} closer to O_{surf} ($I_0 \rightarrow I_1$) by 1.74 eV for $LaCuO_3$, 0.72 eV for $LaNiO_3$, whereas it is less stable by 0.99 eV for $LaCoO_3$. On the other hand, the variations in the reaction energetics of the actual bond-breaking and -forming involved in O_{surf} interacting with O* ($I_1 \rightarrow I_{2/3}$) among the different perovskites are relatively small as indicated by the reaction free energies being generally exothermic (and also the free-energy barriers being generally surmountable at room temperature) for all three perovskites. This can be explained considering that the electron density between the M_{surf} and O* remains relatively constant throughout $I_1 \rightarrow I_{2/3}$ stabilizing the transition state for all perovskites (Figure 3-8).

The significance of these findings is that the extent of O* preferring to sit closer to O_{surf} (e.g. the energy difference between I_0 and I_1) can be a convenient thermodynamic indicator for the kinetic feasibility of the overall O_{surf} participation for a

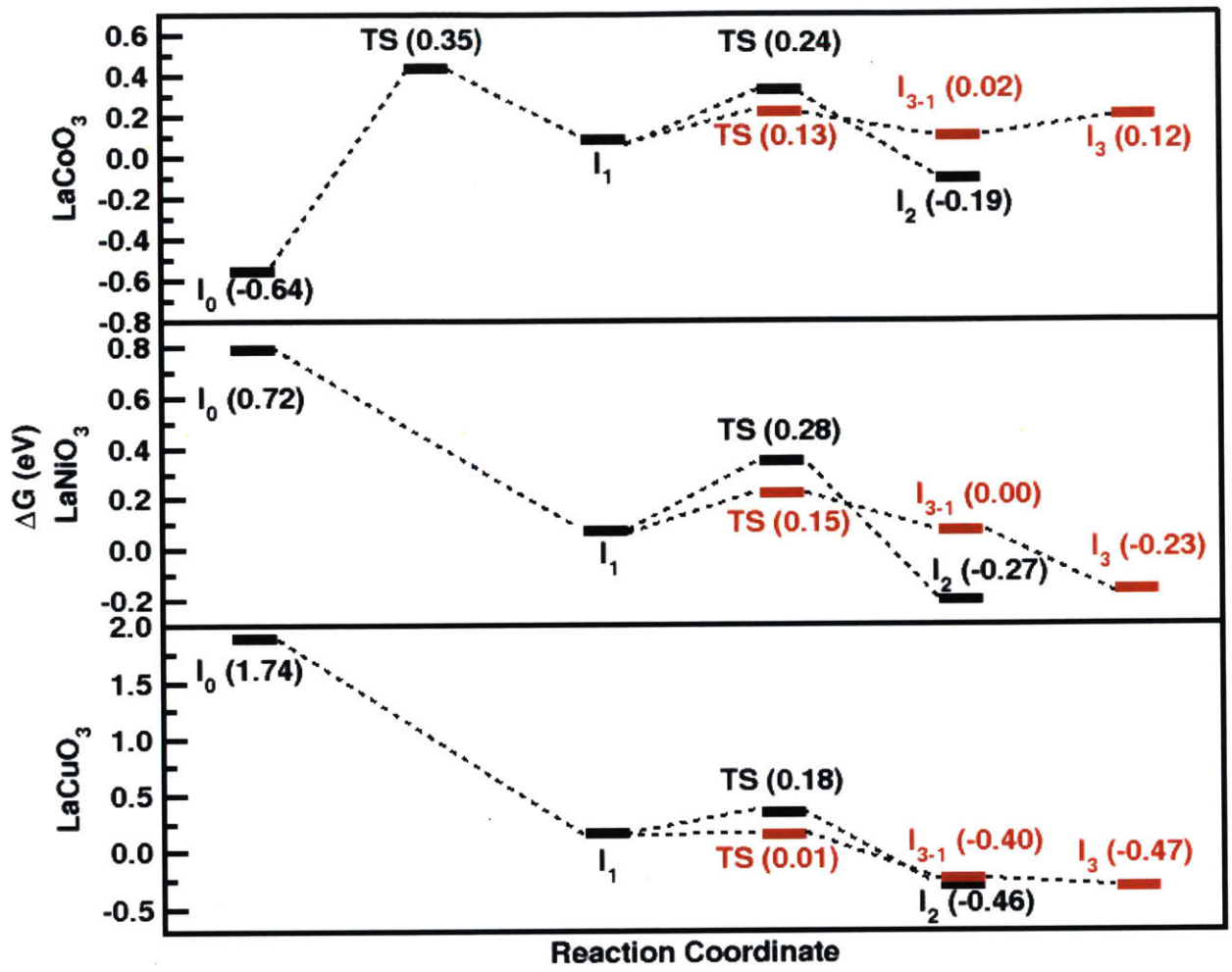

Figure 3-6: The calculated Gibbs free energies of $I_0 \rightarrow I_1 \rightarrow I_{2/3}$ for $LaCoO_3$ (top panel), $LaNiO_3$ (middle panel) and $LaCuO_3$ (bottom panel). All energies are referenced to I_1.

given perovskite as subsequent reaction steps stay largely similar energetically. This is tremendously useful for reducing the computational load of the screening of future perovskite catalysts that will proceed via LOM as finding the transition state from I_1 to $I_{2/3}$ is computationally way more expensive that performing only geometry optimizations for two structures I_0 and I_1. We expect this conclusion to hold for similar perovskites surfaces where O_{surf} and O* are placed in similar electronic environments compared to the three model systems investigated. If the B-sites are mixed (O_{surf} between two different metals) on the surface, further investigation is required

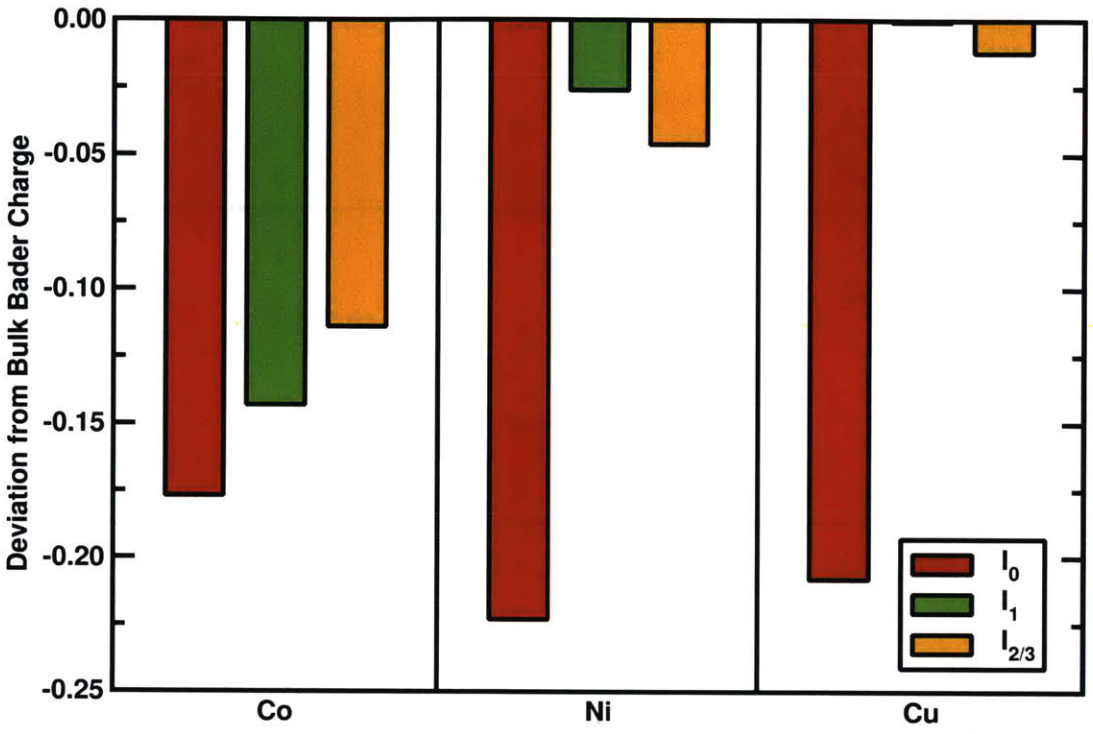

Figure 3-7: Bader charge difference between bulk M^{3+} and M_{surf} in I_0, I_1, and $I_{2/3}$ of $LaMO_3$ (M = Co, Ni, and Cu). Negative value indicates the metal atom has less electrons than M^{3+} (i.e. $M^{(3+\delta)+}$).

to establish the validity of this claim for such cases.

3.3.2 Effect of Reaction Concentration on Reaction Energetics

To better understand O_{surf} participation on moderately binding $LaNiO_3$ under the oxidizing condition of OER, we have investigated the effect of OH* and O* coverages on the reaction energetics of $I_0 \rightarrow I_1 \rightarrow I_{2/3}$, and found that the presence of these adsorbates on the adjacent Ni_{surf} slightly lowers the reaction energies and activation barriers (Figure 3-9).

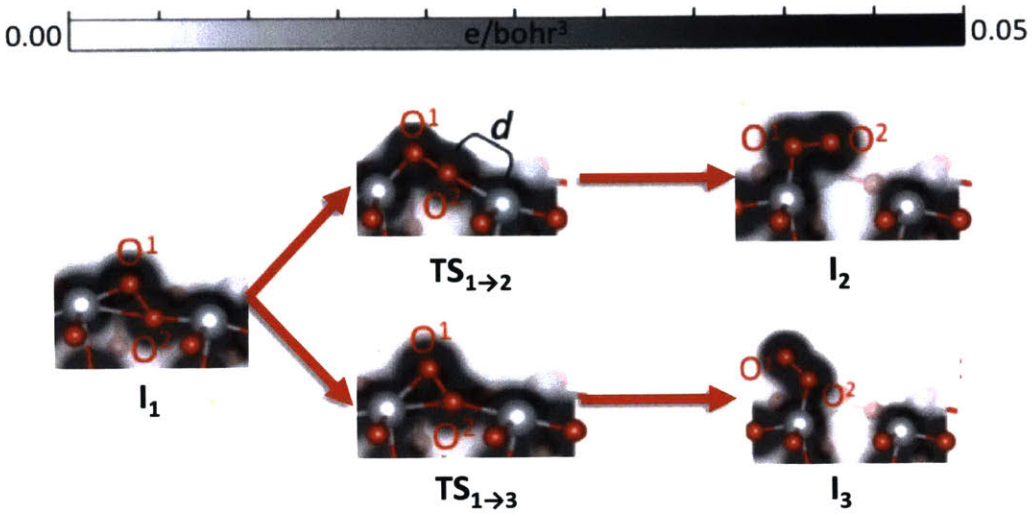

Figure 3-8: The calculated electron densities of all reaction intermediates and transition states of $LaNiO_3$.

This can be explained considering that the adsorption of the oxygen species on Ni_{surf} destabilizes O_{surf} neighboring the Ni_{surf}, thus promoting O* diffusion from a nearby Ni_{surf} to the O_{surf} ($I_0 \rightarrow I_1$) and also stabilizing the relatively oxygen-deficient final state ($I_{2/3}$) that contains V_O. Furthermore, we have also investigated O_{surf} participation on $LaNiO_3$ occurring at higher reaction concentrations, and found that $I_0 \rightarrow I_1 \rightarrow I_{2/3}$ remains exothermic until the reaction concentration is above 50% OH* coverage, as shown in Table 3.3 and Figure 3-10.

Step	Θ=0.00	Θ=0.25	Θ=0.50	Θ=1.00
$I_0 \rightarrow I_1$	-0.86	-0.68	-0.49	–
$I_1 \rightarrow I_2$	–	-0.10	-0.10	0.48

Table 3.3: The reaction free energies (eV) of O_{surf} participation on $LaNiO_3$ at various OO* coverages. Here, the coverage (Θ) is defined as the number of adsorbates in the supercell divided by the four Ni_{surf} sites in the supercell.

We also crosschecked our results by using RPBE+U (U_{eff} = 6.4 eV for nickel [125]), and found that applying the U parameter significantly weakens O* adsorption compared to OH* or OO* adsorption, and therefore induces a higher oxidation state for M_{surf} of I_0 compared to e.g.; that of $I_{2/3}$, further strengthening all the conclusions

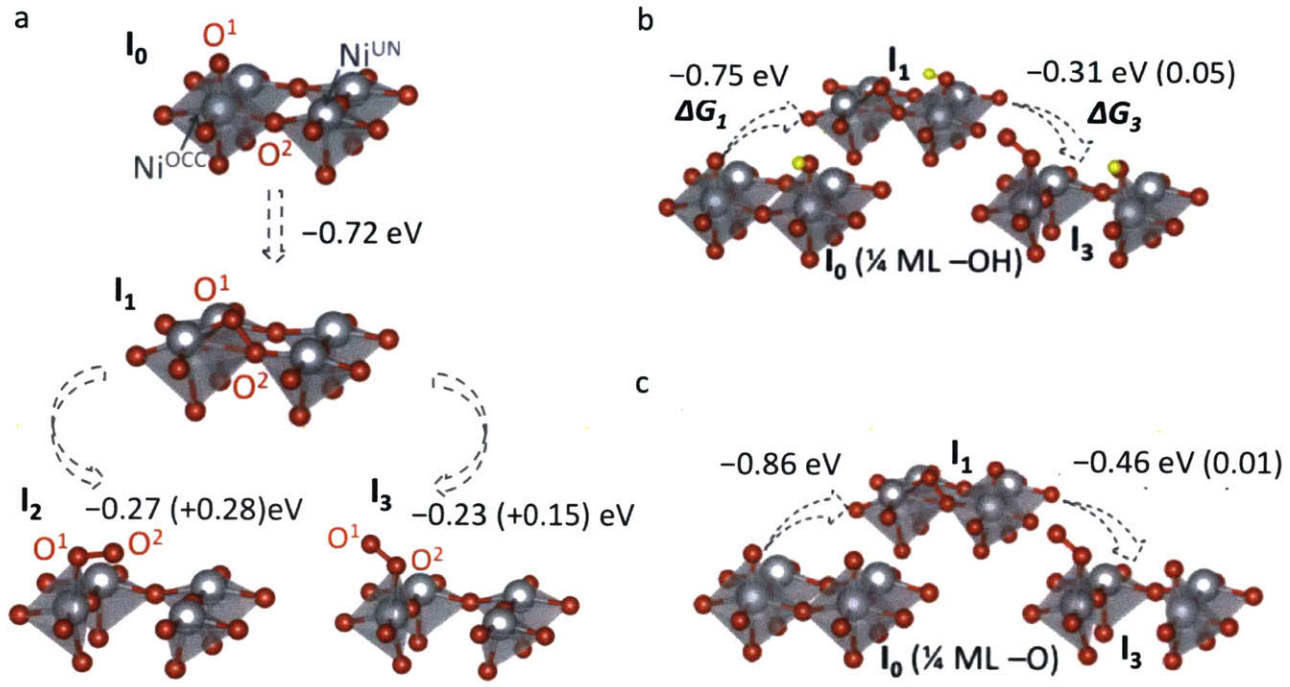

Figure 3-9: Effect of -OH (b) and -O (c) adsorption on reaction energies and activation barriers of LOM on $LaNiO_3$.ΔG_1 is the enthalpic change from I_0-to-I_1 like intermediate, and ΔG_3 is the enthalpic change from I_1-to-I_3 like intermediate. Numbers in brackets indicate kinetic barrier.

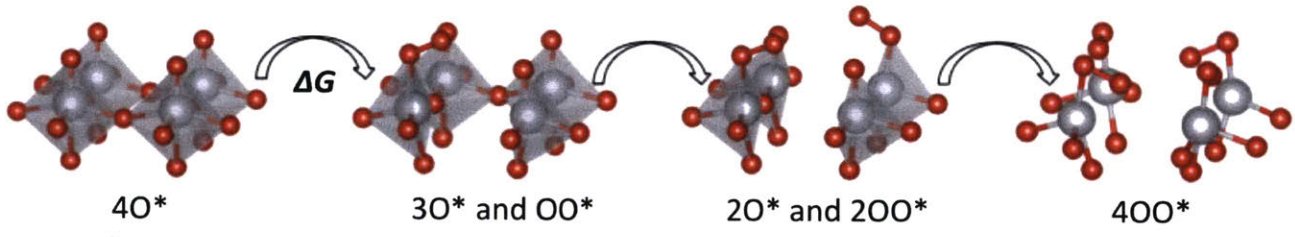

Figure 3-10: From left to right is an illustration of O_{surf} participation ($I_0 \rightarrow I_{2/3}$) occurring on $LaNiO_3$ at OO* coverage of 0.00, 0.25, and 0.75, respectively.

made in this study (Figure 3-11).

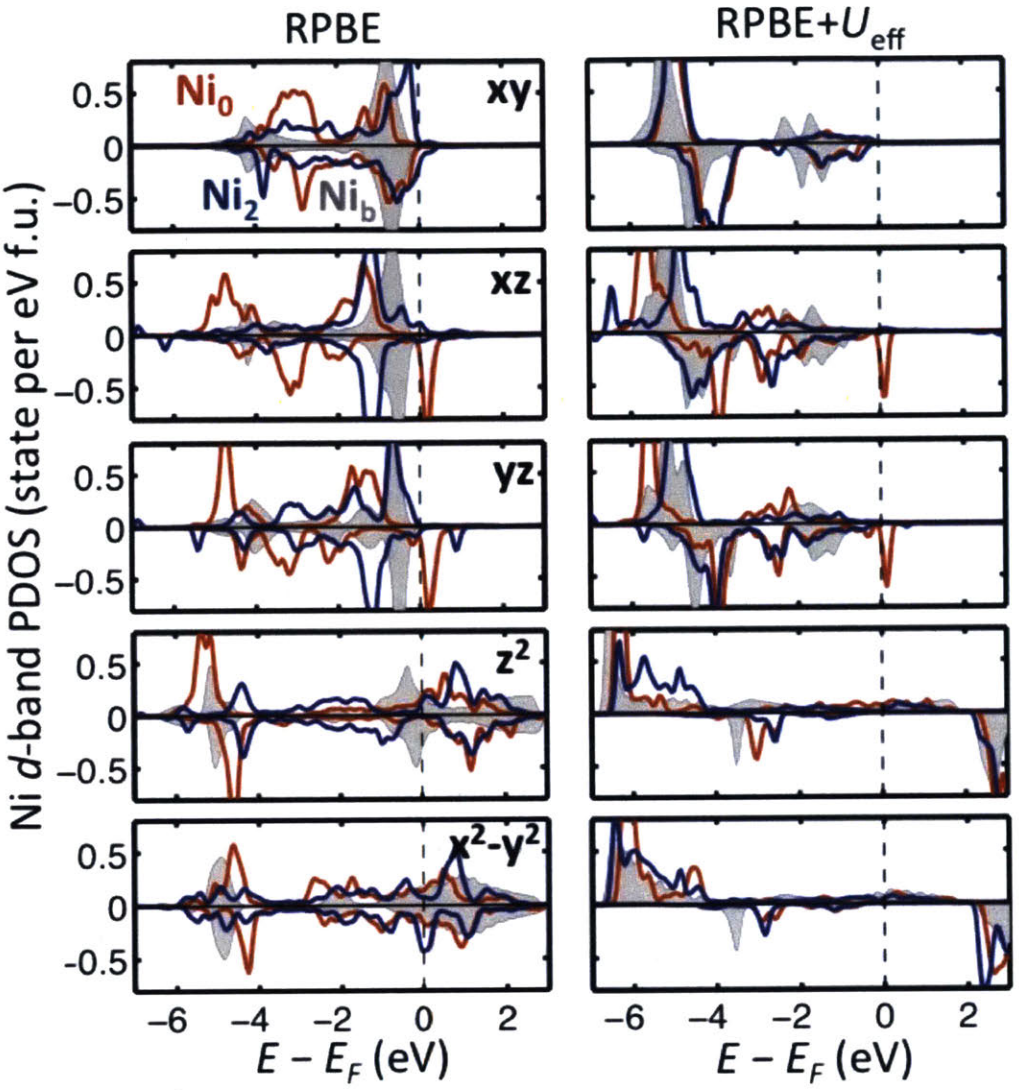

Figure 3-11: Projected density of states for the d states of Ni^{3+} in bulk $LaNiO_3$ (Ni_b), and Ni_{surf} of I_0 (Ni_0) and I_2 (Ni_2), computed by RPBE and RPBE+U (Ueff = 6.4 eV for nickel), respectively. Note that both methods yield similar shifts in the positions of the d bands responsible for the changes in the oxidation state of Ni_{surf} between I_0 and I_2. Thus, the U correction does not change any qualitative conclusions drawn in this study.

3.3.3 Effect of Surface Protonation on Reaction Energetics

In addition, we discuss the possibility of O_{surf} participation competing with undesirable O_{surf} protonation on $LaNiO_3$. The left panel of Figure 3-12(a) shows the reaction

energy of O_{surf} protonation obtained in the low coverage regime of 0.25 ML on clean $LaNiO_3$ (no other adsorbates on Ni_{surf} sites). It can be seen that O_{surf} protonation is highly exothermic (-1.37 eV), and therefore remains as exothermic by -0.14 eV under the OER equilibrium potential of U = 1.23 V, indicating that O_{surf} protonation can occur well before O_{surf} participation on some of the O_{surf} sites. The electronic origin of O_{surf} protonation being highly exothermic can be explained by comparing the pDOS for the p states of different oxygen atoms in the LaNiO3 surface. For example, the right panel of Figure 3-12(a) shows that the p band of O_{surf} is not fully filled with electrons, indicating that O_{surf} is electronically not very stable due to its unsatisfied valence, compared to the protonated surface oxygen (O_{prot}). With electron donations from the adsorbed proton to O_{prot}, the p band of O_{prot} is entirely below the Fermi level, resembling that of the lattice oxygen inside the bulk perovskite (O_{bulk}).

However, Figure 3-12(b) shows that the reaction free energy of O_{surf} protonation increases with increasing proton coverage on both the clean and OH* covered $LaNiO_3$. As a result, the calculated reaction energy at the adsorbed proton coverage of 2 H* is -1.25 eV and -1.65 eV on clean and OH* covered $LaNiO_3$ surfaces, respectively, indicating that many of the O_{surf} atoms (precisely, six out of the eight O_{surf} atoms in the supercell) stay unprotonated at 1.65 V, enabling O_{surf} participation (Figure 3-13).

3.3.4 Effect of Solvation on Reaction Energetics

We now compare the reaction free energies between AEM and LOM on the $LaNiO_3$ surface partially covered with OH* and protons under the water solvent implicitly modeled as a homogeneous dielectric medium, and they are shown in Figure 3-14(a). First, we can see that the inclusion of the solvation effect stabilizes polar adsorbates, such as $H^*_{O\text{-site}}$, OH* and OOH* by 0.1 eV - 0.2 eV, whereas it has a negligible effect on less polar adsorbates, such as OO* and O* (Table 3.2). As a result, the thermodynamic overpotential for the $LaNiO_3$ surface is increased by 0.1 V - 0.2 V for both AEM and LOM as the potential limiting step for AEM is OH* $\rightarrow$ O* (step 1 in Figure 3-1), and that for LOM is $H^*_{O\text{-site}}$ OH* (step (4) in Figure 3-1). However, notice that LOM is much preferred to AEM as the thermodynamic overpotential for

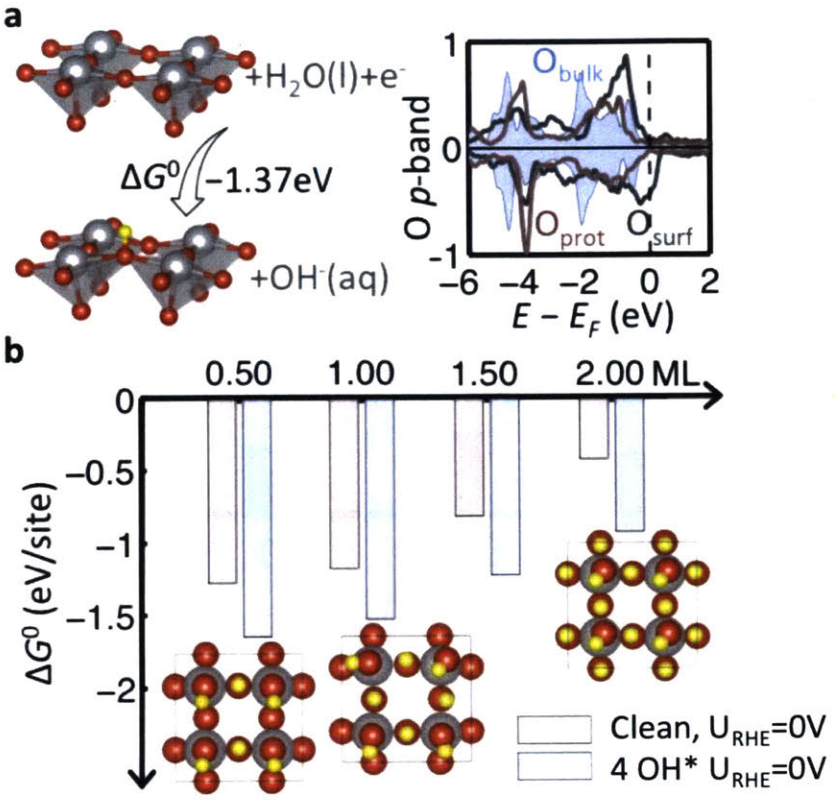

Figure 3-12: (a) The calculated reaction free energy of O_{surf} protonation (left panel) at U_{RHE} = 0 V (pH=0) on clean $LaNiO_3$, and the projected density of states for the p states of different oxygen atoms in the $LaNiO_3$ surface (right panel). O_{bulk} indicates the lattice oxygen in bulk $LaNiO_3$, O_{surf} indicates surface oxygen, and O_{prot} indicates surface oxygen with proton adsorbed on top, and (b) The adsorbed proton concentration dependent reaction energy of O_{surf} protonation on clean (pink) and 4 OH* (1ML) covered (light blue) $LaNiO_3$. The number of adsorbed proton is indicated by H*, fully protonated surface has 8 H* adsorbed.

LOM (η = 0.40 V) is found to be lower than that for AEM (η = 0.89 V) with the adsorbate-coverage and solvation effects all included.

Furthermore, Figure 3-14(b) shows the dependence of the LOM energetics on the reaction concentration. It can be seen that, as the LOM coverage increases from 1/4 (i.e., one of the four adsorbed hydroxyl species being oxidized to O_2) to 1/2 (i.e., two of the four adsorbed hydroxyl species being oxidized to O_2), the overpotential decreases slightly. This indicates that LOM remains thermodynamically favorable as

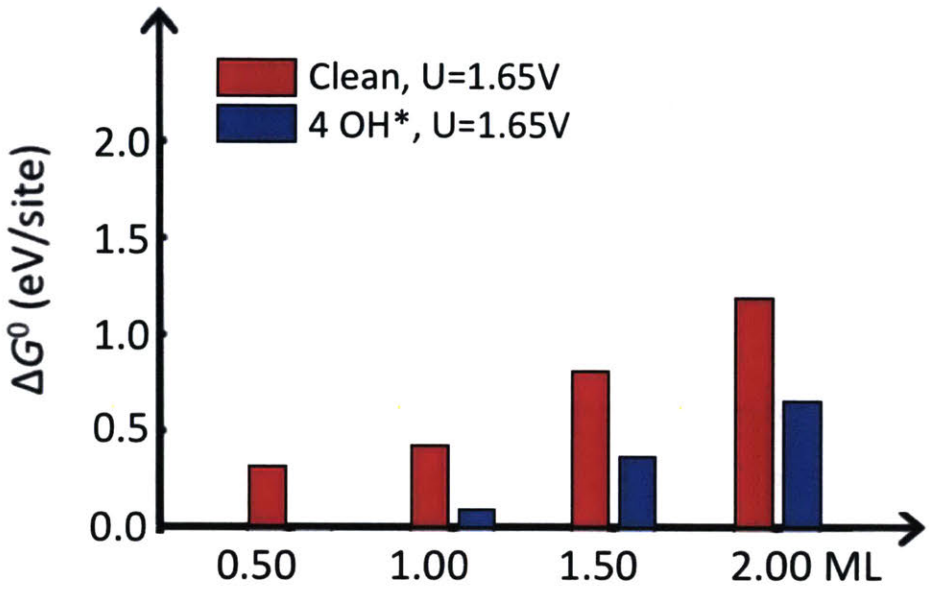

Figure 3-13: The adsorbed proton concentration and applied potential dependent reaction energy of O_{surf} protonation on clean U=1.65 V (magenta) and 4 OH* covered U=1.65 V (dark blue).

long as the amount of V_O surrounding a Ni_{surf} does not exceed one (LOM becomes unfavorable at reaction coverage higher than 1/2 (Table 3.3 and Figure 3-10) because it requires more than one V_O forming around a Ni_{surf}.

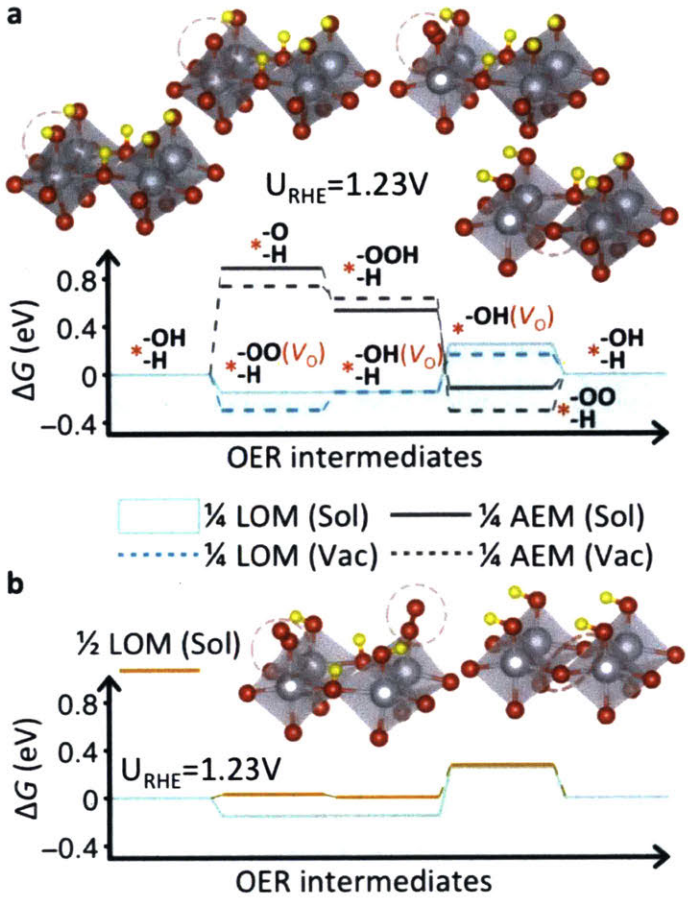

Figure 3-14: (a) The free energy diagrams at U_{RHE} = 1.23 V for OER via AEM (dark grey) vs. LOM (turquoise) on the $LaNiO_3$ surface covered with 1.00 ML of OH* on the Ni sites and 0.50 ML of adsorbed protons on the O sites (note that this is the surface on which O_{surf} protonation becomes endothermic under most OER conditions) at the product (OO*) coverage of 0.25 ML (i.e., one of the four adsorbed hydroxyl species being oxidized to OO*) under vacuum (dashed lines) or the water solvent implicitly modeled as a homogenous dielectric medium (solid lines). (b) The comparison of the free energy diagrams for LOM between the two product (OO*) coverages of 0.25 ML and 0.5 ML under the water solvent model.

3.4 Conclusion

To conclude, we have shown, based on DFT calculations, that O_{surf} of a perovskite can participate in OER via the non-electrochemical route in which adsorbed O* diffuses from M_{surf} to O_{surf} and then O_{surf} shifts out of the surface plane to form OO* and V_O.

This reaction pathway is more favorable for more weakly binding perovskites such as $LaCuO_3$. We found that the the preference of O* sitting on M_{surf} or closer to O_{surf} is a convenient thermodynamic indicator for the kinetic feasibility of overall O_{surf} participation. We also show that the origin of O_{surf} participation can be understood as M_{surf} recovering from the highly oxidized state to the electronically more stable, lower oxidation state throughout the reaction. The different thermodynamic driving forces of O_{surf} participation on different perovskites can be explained by the difference in the transition metals tolerance towards high oxidation states.

To better understand O_{surf} participation on moderately binding $LaNiO_3$ under the highly oxidizing condition of OER, we have investigated the effect of OH* and O* coverages on the reaction energetics of O_{surf} participation, and found that the presence of these adsorbates on the adjacent Ni_{surf} sites makes O_{surf} participation more favorable. Furthermore, we have also investigated the possibility of O_{surf} protonation hindering O_{surf} participation, and found that many of the O_{surf} atoms stay unprotonated under the typical operating OER potential of about 1.65 V, thus enabling O_{surf} participation. Finally, we have compared the reaction free energies between AEM and LOM on the $LaNiO_3$ surface partially covered with OH* and protons in implicit water solvent. As a result, we show that LOM is much preferred to AEM as the overpotential for LOM is found to be much lower than that for AEM with reaction concentration as high as 0.5 ML, thus contributing to a more complete understanding of catalytic mechanisms on different perovskites for water-splitting.

Taken together, these results suggest that in order to break scaling relations and find catalyst candidates that are even better than those on top of the consensus volcano, the identification of new volcanoes is of crucial importance. Instead of dismissing the outliers of the consensus volcano, by focusing on them, we are able to establish a new volcano that leads to the lowest theoretical overpotential for OER and prove its feasibility as well as understanding its electronic structure origins.

Chapter 4

Electronic Structure Analysis of the Oxygen Evolution Reaction via Lattice Oxygen Mechanism for Perovskites with Oxygen Vacancies

Parts of this chapter has been published in the following two papers that I co-authored [87] [88] with Dr. Jong Suk Yoo Dr. Xi Rong and Prof. Alexie Kolpak.

4.1 Introduction

The ideal simple perovskite with the chemical formula ABO_3 has a high tolerance for defect formation. These defects take the form of cation defects, which could be either A-site or B-site, and anion defects in the case of oxygen non-stoichiometry. In the case of cation defects, A-site cation deficiency can occur without compromising the structure as the BO_6 octahedra is very stable. B-site cation vacancies in contrast are less common as it requires larger structural change [126]. Oxygen vacancies occur more frequently than cation deficiencies. Oxygen vacancies in bulk and at interfaces have generated many interesting structural and electronic phenomena. In perovskites, they play important roles [127] such as materials hardening, aging [128–130], fatigue [131] and facilitating oxygen ionic conduction via hopping mechanism driven by an oxygen chemical potential gradient [132–134]. Small changes in oxygen vacancies have leveraged large shifts in the catalytic properties of perovskites other oxides [8, 102, 135–140]. In particular, oxygen vacancies near the surface of a catalyst alter reaction energetics through altering the surface geometry and electronic structure [141–148].

Since the discovery of OER, no study has been conducted to examine how near-surface oxygen vacancies alter the reaction energetics of OER, both kinetically and thermodynamically. Since experimentally synthesized perovskites are often non-stoichiometric [14, 149–151], we investigate the effect of lattice oxygen vacancies on the reaction energetics of O_{surf} participation. We identified trends that correlate activation barrier of key reaction steps to oxygen concentration, and explained how the B-site transition metal electronic properties affect a particular perovskite's tolerance for oxygen vacancies with respect to LOM.

This study expanded the scope of the analysis provided in Chapter 3 to oxygen-deficient perovskites and shed light on how oxygen defect engineering, combined with modifying the B-site cation can tune a perovskite's likelihood to carry out OER through LOM.

4.2 Computational Details

In this study we employ three model perovskite systems - the highly active $LaNiO_3(001)$ as an example for moderately binding perovskites with an oxygen adsorption energy of 3.21 eV relative to H_2O and H_2, $LaCoO_3(001)$ with an oxygen adsorption energy of 2.46 eV relative to H_2O and H_2 for strongly binding perovskites that prefer AEM to LOM, and $LaCuO_3(001)$ with an oxygen adsorption energy of 4.38 eV relative to H_2O and H_2 for weakly binding perovskites that prefer LOM to AEM. The (001) surface plane is chosen for its stability [105,106] and experimental availability [107–110]. For each perovskite, we have three oxygen concentrations, namely $LaMO_3$ (no oxygen vacancy), $LaMO_{2.875}$ (one oxygen vacancy) and $LaMO_{2.75}$ (two oxygen vacancies).

There are two ways in which one vacancy can form in the sub-surface layer of the periodic stable model we employed as shown in Figure 4-1 using I_1 as an example. The vacancy can form under the B-site on top of which is the adsorbed oxygen (left), or it could form in an adjacent site (right). We built all reaction intermediates for these two possible scenarios for thoroughness and chose whatever pathway was thermodynamically more favorable.

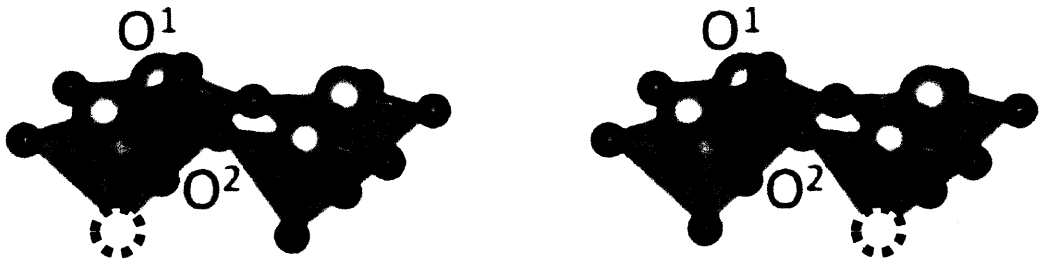

Figure 4-1: The illustration of the two types of vacancies that can form in I_1. Black dotted circle indicates where the vacancy lies.

In the case of two vacancies, an illustration of is shown in Figure 4-2.

Spin-polarized calculations were performed using VASP [82], employing the PAW [111] pseudopotentials with the RPBE [78] functional. We chose the Fast algorithm, Accurate precision, and $4 \times 4 \times 1$ Monkhorst-Pack [112] k-point mesh for all calcula-

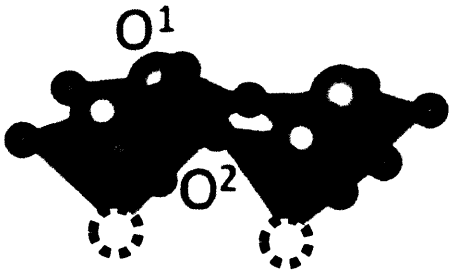

Figure 4-2: The illustration of two vacancies per unit cell in I_1. Black dotted circle indicates where the vacancy lies.

tions with the energy cutoff of 500 eV and Gaussian smearing of 0.1 eV. The periodic slab model for the MO_2 terminated $LaMO_3$ (M = Ni, Co, and Cu) (001) surface was built from the bulk cubic phase using a $2 \times 2 \times 4$ supercell. The periodic slab models were separated by more than 17 Å of vacuum perpendicular to the surface plane. The top two oxide layers of the slab models as well as the adsorbates were allowed relax until the forces on the individual relaxed atoms were less than 0.001 eV per Å.

All adsorption energies were calculated in the low coverage limit of (i.e., one of the four surface nickel atom is has a OH* adsorbed on it), unless noted otherwise, and they were all referenced to gas-phase H_2O and H_2. The projected density of states were calculated using a denser $12 \times 12 \times 1$ Monkhorst-Pack k-point mesh for higher accuracy.

Bader-charge analysis was conducted using the grid-based algorithm [113–116]. The activation barriers were determined using the climbing image nudged elastic band (CI-NEB) method [117, 118]. The reaction free energies were determined using the following equation: $\Delta G = (\Delta E + \Delta ZPE - T\Delta S)_{vac} - eU_{RHE} + \Delta H_{sol}$. $U_{RHE} = 0$ for non-electrochemical reactions. The zero-point-energy (ΔZPE) and entropic ($T\Delta S$) corrections were determined for $LaNiO_3$, and were used for all perovskites. These corrections are shown in Table 3.1.

Crystal Orbital Hamilton Populations (COHP) analysis was conducted using the LOBSTER suite [152–155]. The need for COHP analysis stems from the fact that just by analyzing the density of states we cannot tell if the newly created states introduced by perturbations to the system (creation of oxygen vacancies, oxygen diffusion out

of the lattice etc.) are bonding or antibonding in nature. Using COHP analysis, we are able to differentiate these states and therefore understand if newly created states stabilize (form bonding states) or destabilize (form antibonding states) the system.

		Reaction Energy (eV)	Activation Energy (eV)
$LaCoO_3$	I_0 to I_1	0.64	0.99
	I_1 to I_2	-0.19	0.13
$LaCoO_{2.875}$	I_0 to I_1	0.81	1.21
	I_1 to I_2	0.22	0.47
$LaCoO_{2.75}$	I_0 to I_1	1.08	-
	I_1 to I_2	0.73	-
$LaNiO_3$	I_0 to I_1	-0.72	-
	I_1 to $I_{3\text{-}1}$	0.00	0.15
$LaNiO_{2.875}$	I_0 to I_1	-0.67	-
	I_1 to $I_{3\text{-}1}$	0.07	0.40
$LaNiO_{2.75}$	I_0 to I_1	-0.27	-
	I_1 to $I_{3\text{-}1}$	0.49	-
$LaCuO_3$	I_0 to I_1	-1.74	-
	I_1 to $I_{3\text{-}1}$	-0.40	0.01
$LaCuO_{2.875}$	I_0 to I_1	-1.71	-
	I_1 to $I_{3\text{-}1}$	-0.37	0.05
$LaCuO_{2.75}$	I_0 to I_1	-1.30	-
	I_1 to $I_{3\text{-}1}$	-0.14	0.11

Table 4.1: Reaction energies and activation barriers (in Gibbs free energy) for $LaCoO_{3\text{-}\delta}$, $LaNiO_{3\text{-}\delta}$ and $LaCuO_{3\text{-}\delta}$ where $\delta = 0.125$ and 0.25. Note that the activation barriers are not obtained for the highly exothermic reactions or endothermic reactions. Energies shown correspond to the lower energy path between I_2 and I_3 formation for each material.

4.3 Results and Analysis

4.3.1 Trends in Reaction Energetics

Firstly, we identified that for all three model systems studied, namely $LaMO_3$ where M=Co, Ni, Cu, the one vacancy conformation shown on the left side of Figure 4-1 is more favorable LOM (I_0 less stable than I_1). We then calculated reaction energy of $I_0 \rightarrow I_1 \rightarrow I_{2/3}$ for $LaMO_3$, $LaMO_{2.875}$ and $LaMO_{2.75}$ where M=Co, Ni, and Cu . When the reaction is highly endothermic, we did not calculate the reaction kinetic barrier. The Gibbs free energies are shown in Table 4.1 which included zero-point-energy and entropic corrections (For an illustration of each structure, please refer back to Figure 3-4.).

As expected, $I_0 \rightarrow I_1$ is highly exothermic for $LaCuO_3$ across all oxygen vacancies

(δ), moderately exothermic for $LaNiO_3$ and highly endothermic for $LaCoO_3$. We also identified the trend that, when more lattice oxygen vacancies (δ) are introduced to the subsurface layer of $LaMO_{3-\delta}$ (M = Ni, Co, and Cu), the reaction energies as well as activation barriers for $I_0 \rightarrow I_1 \rightarrow I_{2/3}$ increase. This can be explained considering that O_{surf} participation, which involves reversibly subtracting a surface lattice oxygen from the perovskite to form OO* and V_O, would be more difficult on more oxygen-deficient perovskites as LOM is depriving the perovskite of oxygen even more. However, the effect of the subsurface lattice oxygen vacancies is much smaller for $LaCuO_{3-\delta} < LaNiO_{3-\delta} < LaCoO_{3-\delta}$. For example, incrementally adding one oxygen vacancy in $LaCuO_3$ only decreased the preference of I_1 over I_0 by 0.05 eV on average. In contrast, the decrease was about 0.2 eV for the other perovskites. This can be explained by the fact that though the effect of the subsurface lattice oxygen vacancies is qualitatively the same for all perovskites (one vacancies leaves behind 2 electrons nominally), late transition metals with high electronegativities can better tolerate the electron-rich environment created by lattice oxygen vacancies. In the case of $LaCuO_3$, due to Cu's ability to form stable +1 species, the introduction of vacancies does not significantly affect its ability to react via LOM. On the other hand, $LaNiO_3$ is more sensitive to vacancy formation and therefore is increasingly less likely to proceed via LOM as more vacancies are introduced.

Evidently, the transition metals' most favored oxidation state contributes to the determination of whether it prefers I_0 or I_1, as well as how many vacancies it can tolerate without structural distortion that leads to instability. We established in the previous chapter that the preference of I_1 over I_0 is an indicator of if a reaction will proceed through LOM. We can see here that taking vacancies into consideration does not alter our conclusion. As shown in the case of $LaNiO_3$, a decrease in the exothermicity of $I_0 \rightarrow I_1$ when two vacancies are introduced made the following reaction steps thermodynamically uphill. While in the case of $LaCuO_3$, an almost constant exothermicity of $I_0 \rightarrow I_1$ caused by Cu's ability to tolerate a low oxidation state after vacancies are introduced, guaranteed the feasibility of the following reaction steps.

4.3.2 Electronic Structure Analysis

Since $I_0 \rightarrow I_1$ is the determinant of if a perovskite will partcipate in OER via LOM, we take a closer look at the change in electronic structure of these two species. We plot the projected density of states (PDOS) of the metal B-site in I_0 and I_1 compared to bulk metal for $LaMO_3$ (Figure 4-3), $LaMO_{2.875}$ (Figure 4-4) and $LaMO_{2.75}$ (Figure 4-5).

The first feature to note is that in all three $LaMO_{3-\delta}$, the M_{surf} in I_0 (red) has a significant amount of states above the fermi level as compared to M^{3+} in bulk. This indicates that M_{surf} in I_0 is electron deficient compared to M^{3+} in bulk as corroborated by bader charge analysis (Figure 4-6 red bars). In the cases of $LaNiO_{3-\delta}$ and $LaCuO_{3-\delta}$, I_1 (shaded grey in PDOS plots), have significantly reduced states above Fermi-level compared to I_0 for all three oxygen vacancy concentrations which indicates less electron deficiency as shown in Figure 4-6 where I_1 of all three oxygen vacancy concentrations for $LaNiO_{3-\delta}$ and $LaCuO_{3-\delta}$ show little electron deficiency or even electron surplus compared to bulk. In $LaCoO_{3-\delta}$, the effect is less pronounced as the PDOS of I_0 and I_1 show less difference in states above the Fermi-level. For $LaCoO_3$ and $LaCoO_{2.875}$, the Bader charges of I_1 do not remedy the electron deficiency of I_0 significantly (Figure 4-6).

Here, we note that $LaCoO_{2.75}$ with two oxygen vacancies presents an apparent exception as I_1 is 1.05 eV higher in energy than I_0 (Table 4.1) but I_1 seems to have stabilized I_0 by being less electron deficient. This can be explained as we delve into the origin of the observed stability trends. The most stable oxidation state of Co is +3 while that of Ni is +2, and Cu is +1 and +2. For the surface Co in I_1 of $LaCoO_{2.75}$ with two oxygen vacancies to accommodate the additional electrons left behind through the creation of two oxygen vacancies, it has to go lower than its most stable oxidation state and forms a highly distorted structure in which the Co-O_{ads} bond is strained to -8.1% of the Co-O bond distance in $LaCoO_{2.75}$ bulk (as compared to -6.6% for $LaNiO_{2.75}$ and -1.6% for $LaCuO_{2.75}$ in the same scenario).

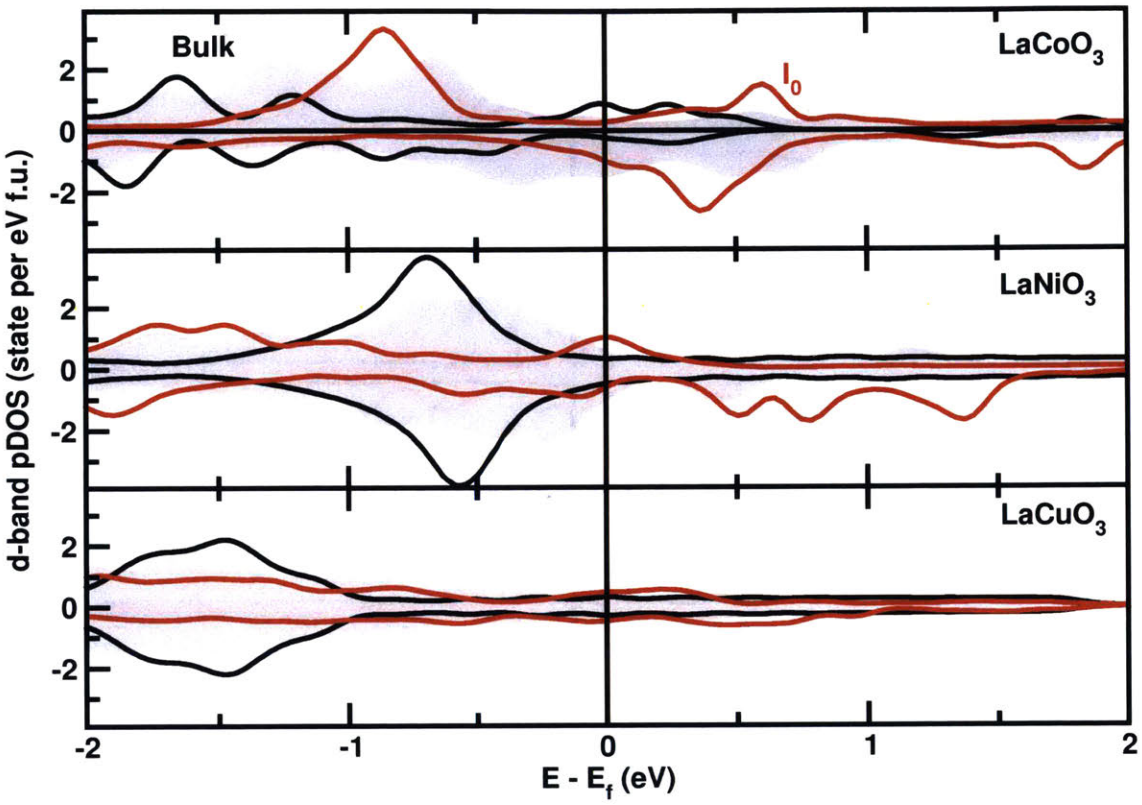

Figure 4-3: Projected density of states for the d states of M^{3+} in bulk without O vacancy (black), and M_{surf} in I_0 (red) and I_1 (grey) for $LaCoO_3$ (top panel), $LaNiO_3$ (middle panel), and $LaCuO_3$ (bottom panel).

4.3.3 Crystal Orbital Hamiltonian Population Analysis

We also conducted COHP analysis of the M_{surf}-O* bond of $LaCoO_{3-\delta}$, $LaNiO_{3-\delta}$ and $LaCuO_{3-\delta}$ for δ=0 (Figure 4-7), 0.125 (Figure 4-8) and 0.25 (Figure 4-9) for both I_0 and I_1 to examine how this transition shifts the occupation of the antibonding states in this bond.

It is evident that close to the Fermi level, there are occupied states just below the Fermi level that are antibonding (shown as positive in the COHP plots). Therefore, these states destabilizing the system if occupied. In the cases of $LaCoO_{3-\delta}$, we do

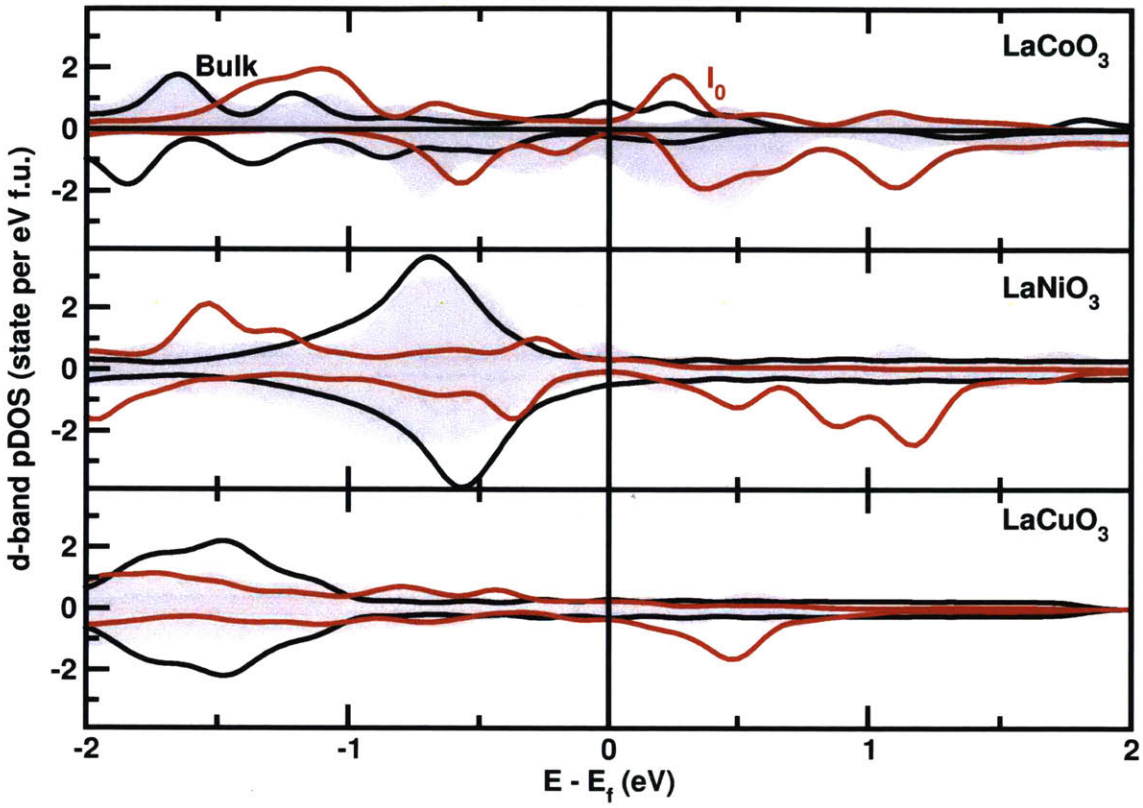

Figure 4-4: Projected density of states for the d states of M^{3+} in bulk without O vacancy (black), and M_{surf} in I_0 (red) and I_1 (grey) for $LaCoO_{2.875}$ (top panel), $LaNiO_{2.875}$ (middle panel), and $LaCuO_{2.875}$ (bottom panel). These perovskites are obtained by removing one lattice oxygen atom underneath the two M_{surf}s of $LaMO_3$ (224) supercell. O* in I_0 or I_1 is adsorbed on one of the two M_{surf}s.

not observe a significant reduction of these occupied antibonding states going from I_0 to I_1 and therefore stablization in terms of energy is not observed in the reaction energy diagram (Table 4.1). For $LaCuO_{3-\delta}$ and $LaNiO_{3-\delta}$, I_1 has much less occupied antibonding states than I_0, therefore substantially stabilizing the system. This reduction is especially apparant in the case of $LaCuO_{3-\delta}$ where an expansive portion of occupied antibonding states in I_0 is reduced to a much smaller peak in I_1.

Therefore, from a bonding point of view, we can also explain why $LaCuO_{3-\delta}$ is

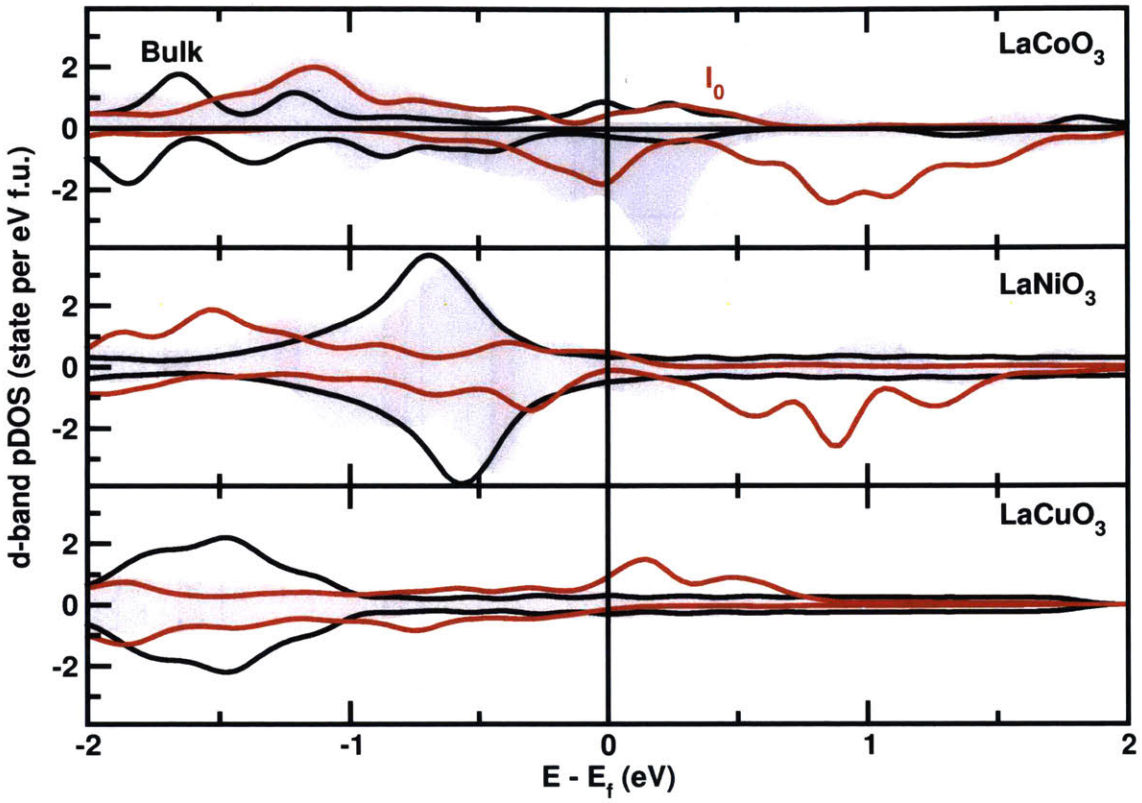

Figure 4-5: Projected density of states for the d states of M^{3+} in bulk without O vacancy (black), and M_{surf} in I_0 (red) and I_1 (grey) for $LaCoO_{2.75}$ (top panel), $LaNiO_{2.75}$ (middle panel), and $LaCuO_{2.75}$ (bottom panel). These perovskites are obtained by removing two lattice oxygen atoms underneath the two M_{surf}s of $LaMO_3$ (224) supercell. O^* in I_0 or I_1 is adsorbed on one of the two M_{surf}s.

most likely to proceed via LOM, followed by $LaNiO_{3-\delta}$. While for $LaCoO_{3-\delta}$, the step that we identified as the thermodynamic indicator of LOM feasibility is not favorable due to a lack of reduction of occupied antibonding states.

4.3.4 Bader Charge Analysis

To more quantitatively correlate the difference in thermodynamic driving forces of O_{surf} participation on different perovskites described in the previous section to reac-

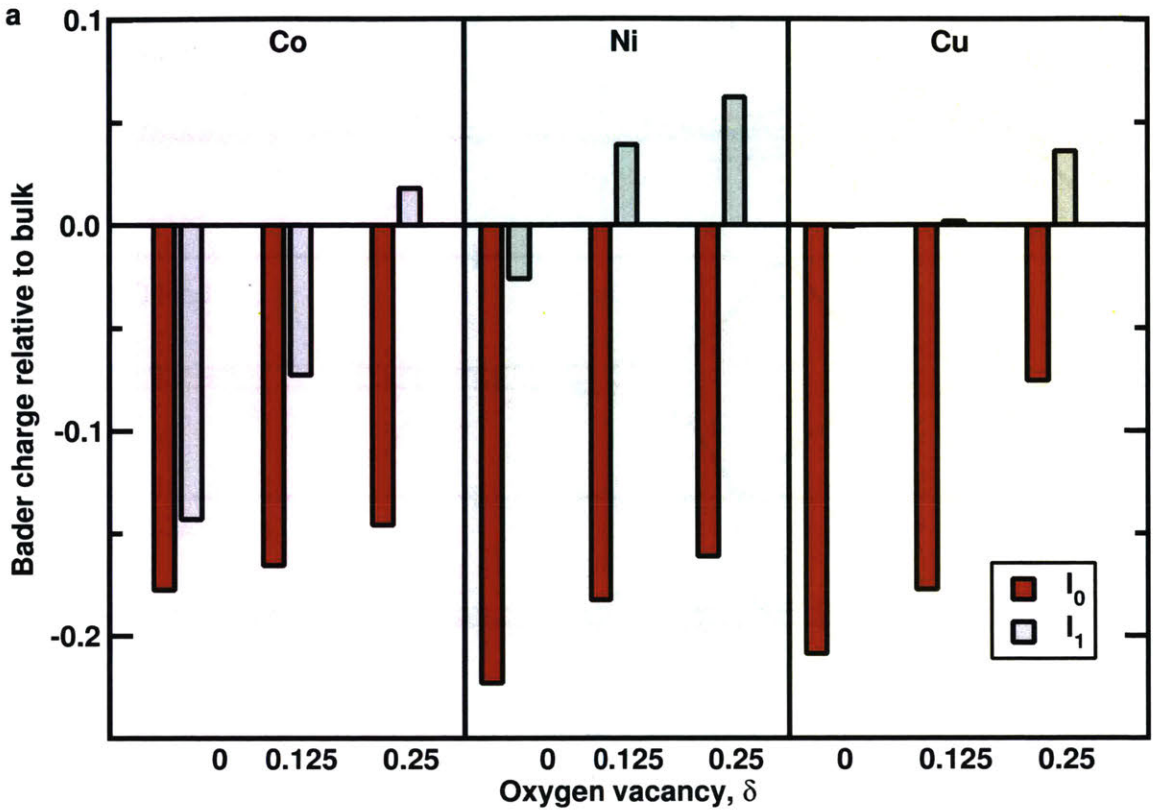

Figure 4-6: Relative number of electrons of M_{surf} of I_0 (red) and I_1 (grey) of $LaMO_{3-\delta}$ (M = Co, Ni, and Cu; δ = 0, 0.125, 0.25) relative to bulk M in $LaMO_{3-\delta}$ based on Bader charge analysis. Negative value indicates a smaller number of electrons (electron deficiency).

tion energies, we compared the relative Bader charges on M_{surf} of I_0, I_1, and $I_{2/3}$ of $LaMO_{3-\delta}$ (δ = 0, 0.125, and 0.25) to the calculated reaction energies of O_{surf} participation on $LaMO_{3-\delta}$. The charge we have chosen is the Bader charge relative to the most stable oxidation state of the metal.

A comparison between Figure 4-10a and Figure 4-10b reveals that there is an apparent correlation between the changes in the number of electrons in M_{surf} throughout O_{surf} participation, and the energies of I_1 and $I_{2/3}$ relative to I_0. For example, in the case of $LaCoO_3$, the electron deficiency of M_{surf} (see Figure 4-10a, left panel) is not

significantly alleviated by $I_0 \rightarrow I_1$ or $I_0 \rightarrow I_{2/3}$. As a consequence, the energies of I_1 and $I_{2/3}$ are high relative to I_0 (see Figure 4-10b, left panel) indicating endothermic O_{surf} participation. For $LaNiO_3$ and $LaCuO_3$ the electron deficiency of M_{surf} is significantly alleviated by $I_0 \rightarrow I_1$ or $I_0 \rightarrow I_{2/3}$ (see Figure 4-10a, center or right panel). As a consequence, I_1 and $I_{2/3}$ are energetically stabilized relative to I_0 (see Figure 4-10b, center or right panel) indicating exothermic O_{surf} participation.

These results support our hypothesis that the origin of the thermodynamic driving force of O_{surf} participation can be understood as M_{surf} recovering from the highly oxidized state to the electronically more stable, lower oxidation state throughout the reaction.

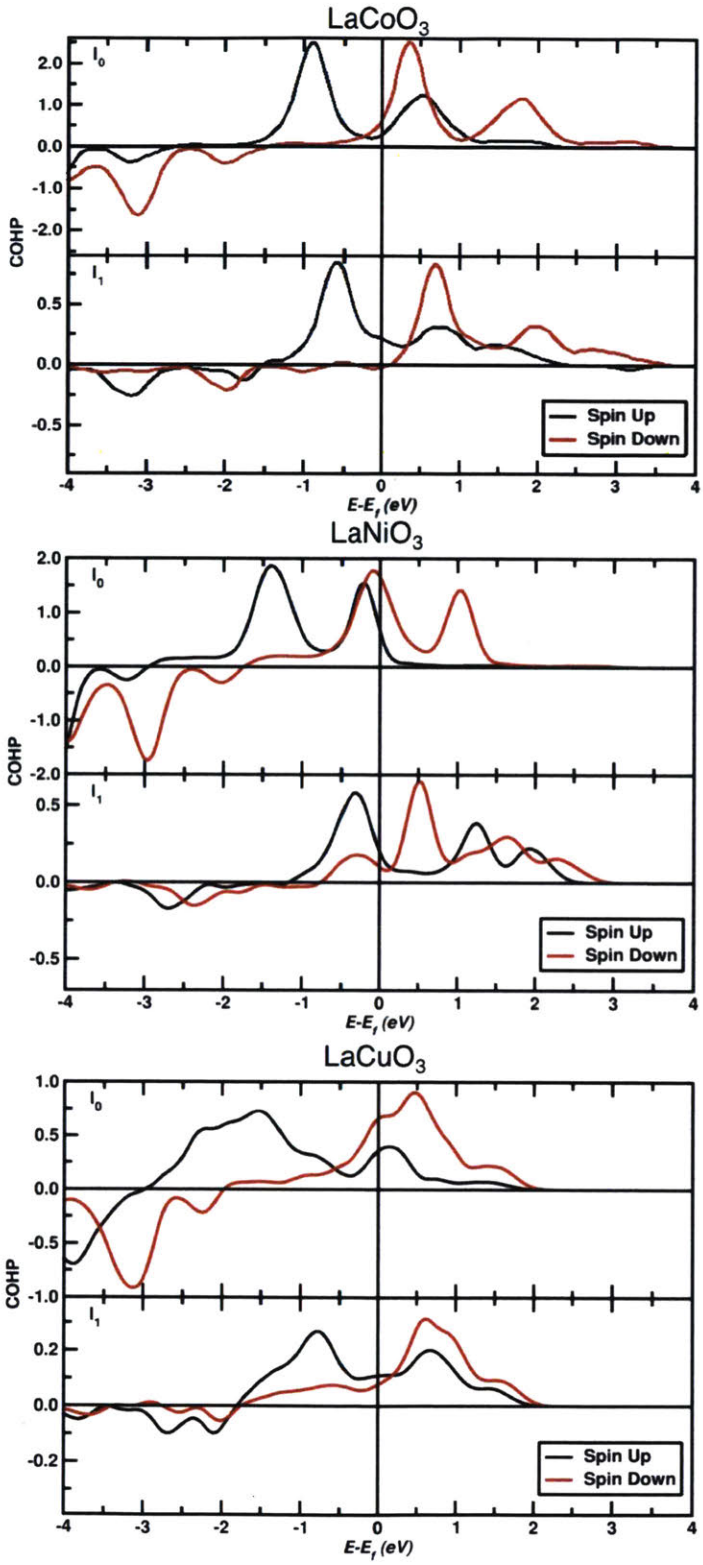

Figure 4-7: COHP analysis of M_{surf}-O* bond of $LaCoO_3$ (top panel), $LaNiO_3$ (middle panel), and $LaCuO_3$ (bottom panel). Negative y-value indicates bonding contribution, positive y-value indicates antibonding contribution to the total energy of the bond.

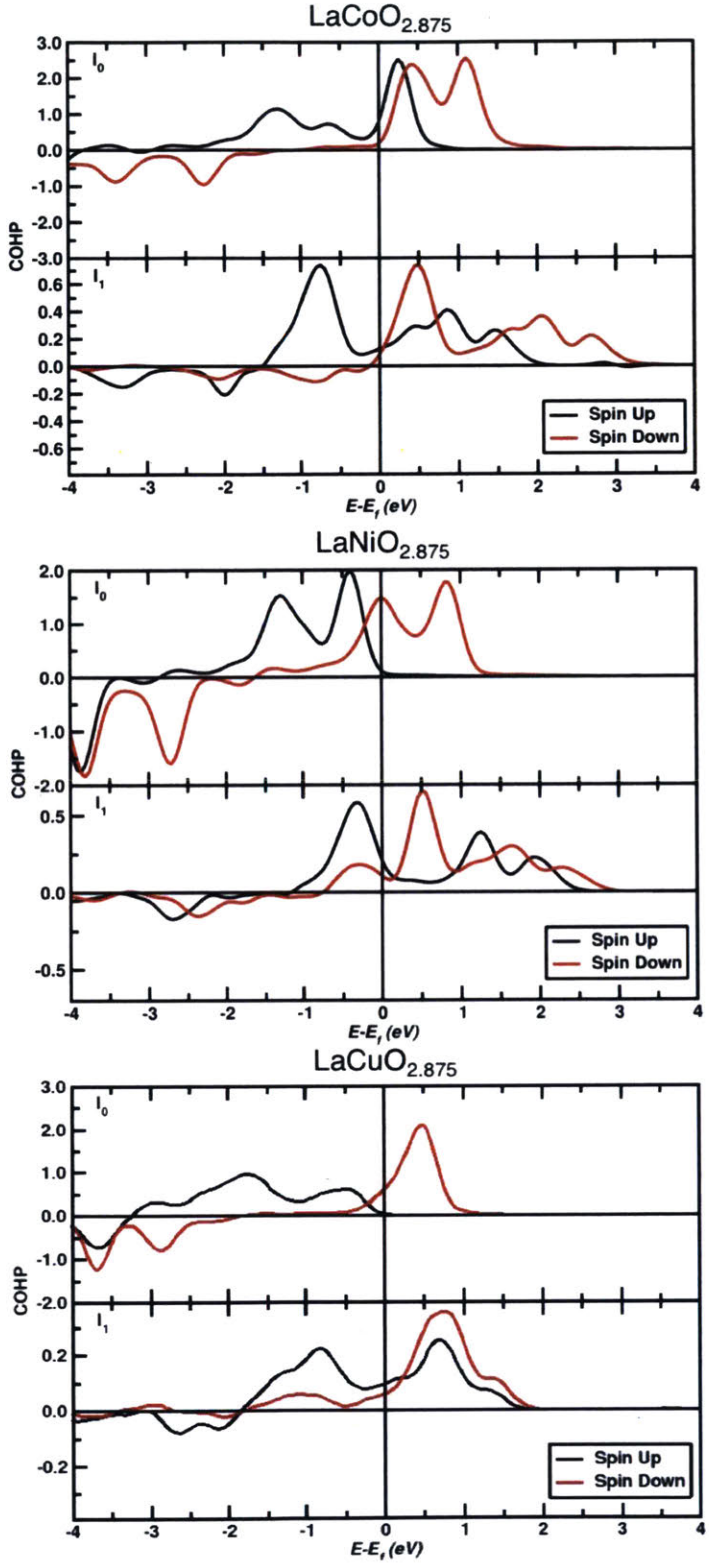

Figure 4-8: COHP analysis of M_{surf}-O* bond of $LaCoO_{2.875}$ (top panel), $LaNiO_{2.875}$ (middle panel), and $LaCuO_{2.875}$ (bottom panel). Negative y-value indicates bonding contribution, positive y-value indicates antibonding contribution to the total energy of the bond.

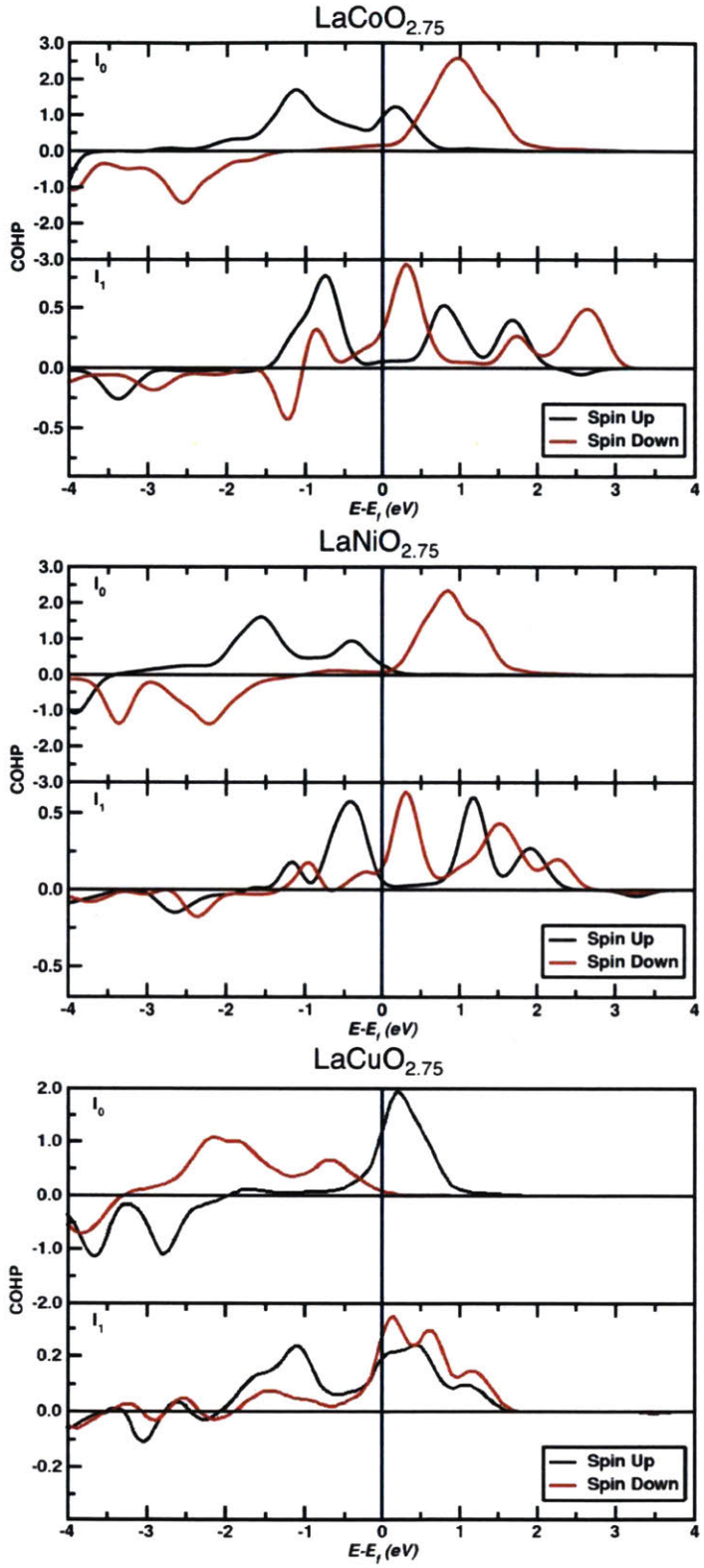

Figure 4-9: COHP analysis of M_{surf}-O* bond of $LaCoO_{2.75}$ (top panel), $LaNiO_{2.75}$ (middle panel), and $LaCuO_{2.75}$ (bottom panel). Negative y-value indicates bonding contribution, positive y-value indicates antibonding contribution to the total energy of the bond.

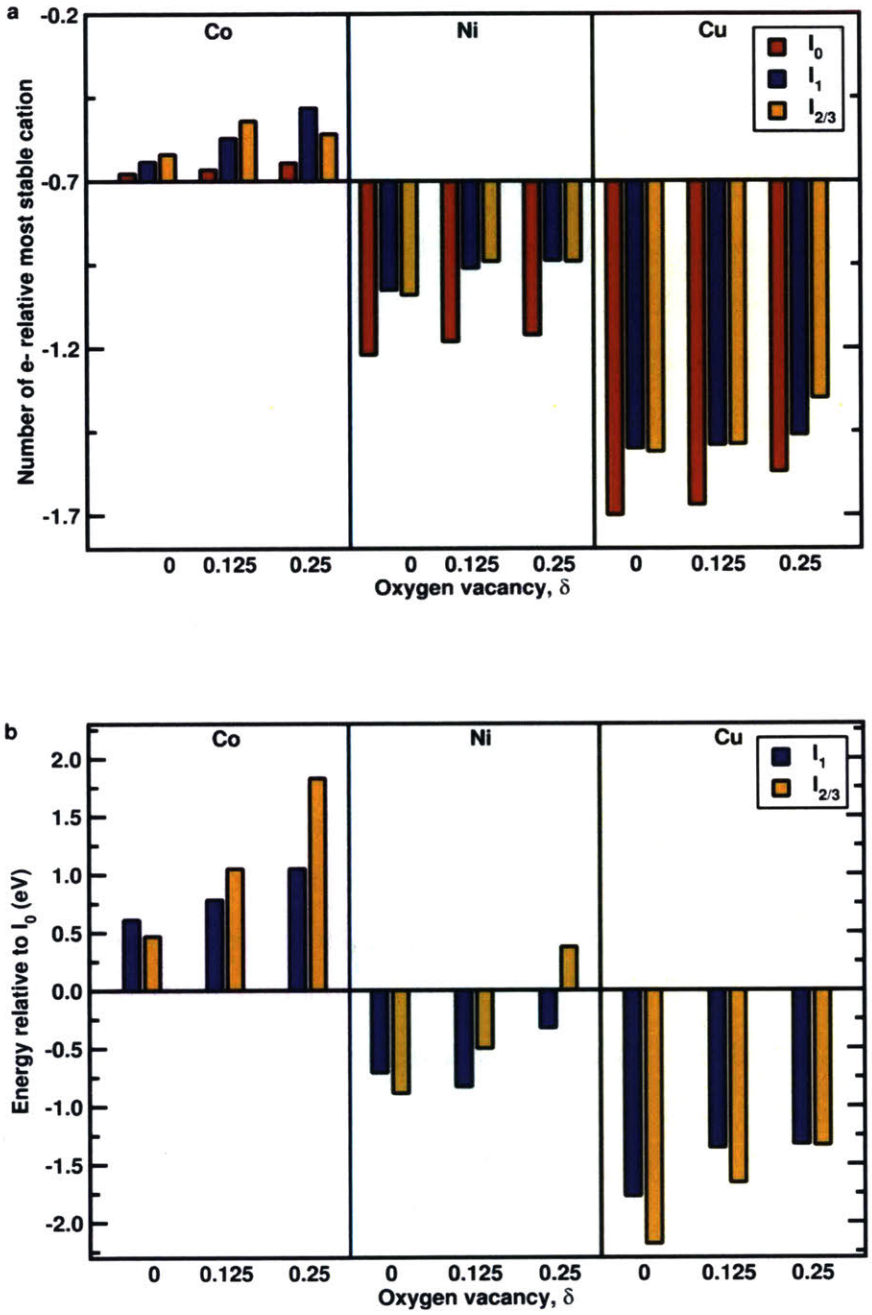

Figure 4-10: (a) The extra number of electrons in M_{surf} of I_0, I_1, and $I_{2/3}$ of $LaMO_{3-\delta}$ (M = Co, Ni, and Cu; $\delta = 0, 0.125, 0.25$) relative to that in the most stable transition-metal cation (Co^{3+} or Co^{2+}, Ni^{2+}, and Cu^{1+} or Cu^{2+}), obtained based on the Bader-charge analysis. In cases where two transition-metal cations are known to be stable, the average of the two is used. In (a), the x axis is arbitrarily positioned at y = 0.7, instead of y = zero, such that the trend in (a) can be more clearly compared to that in (b). (b) The calculated energy differences between I_0 and I_1, I_0 and $I_{2/3}$ on $LaMO_{3-\delta}$.

4.4 Conclusion

In this chapter, we have calculated the reaction energies from $I_0 \rightarrow I_1 \rightarrow I_{2/3}$ for $LaMO_{3-\delta}$ (M=Co, Ni, and; $\delta = 0$, 0.125, and 0.25) and observed that $LaCuO_{3-\delta}$ participates in LOM most readily, followed by $LaNiO_{3-\delta}$, while $LaCoO_{3-\delta}$ does not participate in LOM. We further strengthened the conclusion reached in the previous chapter that the energy difference between I_0 and I_1 serves as a good descriptor for whether a perovskite will carry out OER via LOM, even as we include various vacancy concentrations. In addition, we observed that as oxygen vacancies are introduced into the subsurface layer of the perovskite, LOM participation becomes more and more difficult. This is because LOM requires oxygen diffusion out of the perovskite lattice, which is more challenging on already oxygen-deficient perovskites. We also noted that different perovskites have different tolerance for oxygen vacancy concentrations with respect to LOM reaction barriers. $LaCuO_{3-\delta}$ can tolerate oxygen vacancies better than $LaNiO_{3-\delta}$ as reaction barriers did not become insurmountable due to the introduction of oxygen vacancies. This can be explained by the fact that Cu can form stable +1 species while Ni prefers +2 as its most stable oxidation state. As a result, Cu can tolerate more electrons left behind by the creation of oxygen vacancies.

To explain these observations we conducted PDOS, COHP and Bader charge analysis. We concluded that for a particular perovskite, if $I_0 \rightarrow I_1$ returns the PDOS to be more bulk-like, LOM will be favorable as the charge state on the B-site is stabilized. In addition, COHP analysis also showed that this return to bulk-like state corresponds to the reduction of occupied antibonding states in the M_{surf}-O bond, which stabilizes the system energetically. Finally, we correlated the change in M_{surf}'s deviation from the metal's most stable oxidation state to the energy of a particular reaction, showing that O_{surf} will participate in OER if M_{surf}, through the reaction, can reach a more stable oxidation state.

Chapter 5

Structural and Electronic Properties of Pt-coated Transition Metal Carbide and Nitride Nanoparticles

Parts of this chapter is under revision in the following paper that I co-authored [156] with my experimental collaborators Dr. Aaron Garg et al.

5.1 Introduction

Core-shell nanoparticles (NPs), where an inexpensive core made with earth-abundant materials is coated with a noble metal shell, represent a new and exciting class of materials that display enhanced catalytic properties for reactions such as the oxygen reduction reaction and CO_2 reduction [49, 157–164]. Not only are they cheaper to manufacture compared to bulk metal nanoparticles, variations in core-shell compositions and thickness can also be used to tune the performance and selectivity of these materials [165]. Early-transition-metal carbides (TMCs) and transition metal nitrides (TMNs) are often used as catalysts for a wide range of reactions [51,166–174]. They are also ideal core materials due to their thermal stability, chemical stability and affordability [57,175]. Our experimental colleagues have recently succeeded in synthesizing TMN and TMC NPs with atomically thin Pt shells [57–59]. Since TMNs offer an additional valence electron from N as compared to TMCs and N is more electronegative than C, the electronic properties of TMN NPs and TMC NPs are expected to differ, as are their catalytic abilities. These NPs exhibit differing catalytic behaviors compared to pure Pt NPs in terms of selectivity [58] and sinter-resistance [57]. However, a detailed explanation of these differing behaviors is still elusive and requires further studies.

In this study, I collaborated with experimental colleagues Dr. Aaron Garg et al. to elucidate the structural and electronic origins of the altered catalytic properties of Pt-coated TiWN and Pt-coated TiWC NPs (Ti:W ratio ca. 10:90, particle size ca. 7 nm). There are a few experimental observations that require theoretical insights for explanations. Firstly, it is observed through CO microcalorimetry measurements that CO on Pt NPs show a large heat of adsorption while the same heat signature was not observed on Pt/TiWN or Pt/TiWC [156]. Secondly, ethylene hydrogenation turn-over-frequencies (TOFs) shows a trend of Pt > Pt/TiWC > Pt/TIWN at 45°. However, when the NPs are prepared at a higher temperature, the TOFs on Pt/TiWC and Pt/TiWN shows an order of magnitude drop [156].

In this chapter, I will present detailed analysis of charge transfer, density of states,

atomic distances and coordination, as well as oxygen binding energies using DFT which provide fundamental explanations to these experimental phenomena. In addition, physical insights gained from this study could provide further guidance for the future design of TMNs and TMCs.

5.2 Computational Details

Recent theoretical work has pointed out that in order to realistically model core-shell NPs with an accurate description of surface and interface topology, a procedure called heat-quench-exfoliation (HQE) should be applied [2]. The HQE method (Figure 5-1) constructs a NP with excessive shell layers, heats the NP so that atoms find their thermodynamically favorable positions, cools it, and then removes excessive shell layers. This method prevents unrealistic initial guesses of core-shell NP topology and provides a good starting point for temperature-independent DFT calculations. Since the electronic properties of core-shell NPs vary drastically based on topology, it is essential to find a realistic structure in order to predict their catalytic properties. It has been demonstrated that geometrical structure and subsequent electronic structure changes are responsible for altering the catalytic properties based on both strain and ligand effects [176–182]. Therefore, in this study we employ HQE derived starting structures for enhanced modeling accuracy.

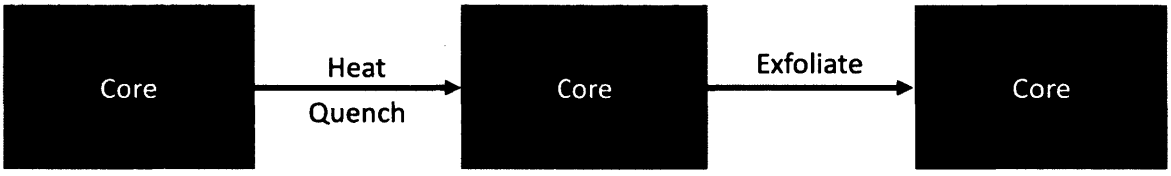

Figure 5-1: Schematic of the heat-quench-exfoliation (HQE) method. In this method, multiple layers of the shell material are constructed on top of the core at first, then the whole system is heated via ab initio molecular dynamics so that atoms have enough energy to move to more favorable positions. The system is then cooled down and the excess layers are removed. The monolayer is geometry optimized as a last step. Adapted from [2].

Spin-polarized calculations were performed using VASP [82] with PAW pseudopotentials [111] and the RPBE functional [78]. The Fast algorithm, Accurate precision, and $2 \times 2 \times 1$ Monkhorst-Pack k-point mesh [112] were used for all Pt/TiWC and Pt/TiWN slab calculations with an energy cutoff of 520 eV and a Gaussian smearing of 0.1 eV. The periodic slab models for Pt/TiWC and Pt/TiWN were built using the

methods outlined in [2] separated by more than 17 Å of vacuum perpendicular to the surface plane.

Due to the high computational intensity needed for these calculations, 1 monolayer of Pt-shell was modeled and, when comparing to experimental findings, extrapolated to the 2 monolayer case. The Pt layer along with the top 2 layers of TiWC or TiWN in the slab model and any adsorbates were allowed to relax until the forces on the individual relaxed atoms were less than 0.001 eV per Å. PDOS were calculated using a dense $9 \times 9 \times 1$ Monkhorst-Pack k-point mesh for accuracy.

5.3 Experimental Techniques

As this chapter concerns a collaboration of experiments and theoretical modelling in which I undertook only work for the latter, detailed experimental descriptions will not be presented but can be found in our paper [156]. However, a brief overview of the experimental techniques is provided here to guide readers unfamiliar with these methods so that subsequent sections citing results from these experiments are accessible.

Both techniques presented here are absorption processes of X-ray absorption spectroscopy (XAS). Though XAS is most known for probing atomic energy levels, it can also be used to give experimenters information about the lattice such as nearest neighbor distance and coordination number. In this study, both the energy level and structural uses of XAS are employed.

5.3.1 X-Ray Absorption Near Edge Structure (XANES)

XANES probes the absorption process where a core level electron is excited by the incident photon to a higher energy level. As each element has distinct energy levels, as long as these energy levels are not in close proximity to each other, they can be isolated and studied separately.

In this work, we used XANES to probe the Pt L_2-edge which is the transition of $2p_{1/2}$ to primarily $5d_{3/2}$ states. Due to spin-orbit coupling, the 5d states are split into $5d_{3/2}$ and $5d_{5/2}$ states. The $5d_{5/2}$ states are probed by Pt L_3-edge. However, its energy is close to the W L_2-edge therefore we could not use it in this study as our material contains W. The intensity of the absorption peak at the top of the rising edge (the white line) in the XANES spectra is a direct probe of the unoccupied d states and can provide details about the valence d band above the Fermi level [183].

5.3.2 Extended X-Ray Absorption Fine Structure (EXAFS)

EXAFS probes the result of the interference of the final wave function of the absorbing atom caused by resonant radiation and the backscattered electrons of neighboring

atoms. As these modulations interact with the outgoing electron from core levels of the absorbing atoms, the atom's environment in the lattice can be studied. Properties such as interatomic distance, coordination number and mean-square disorder of the interatomic distance can be fitted to the EXAFS region of the spectra [184]. This is done by fitting the oscillatory part of the absorption coefficient to the following form:

$$\chi(k) = \sum_{n=1}^{n} \frac{N_i}{kR^2} A_i(k) e^{(-2\sigma^2 k^2)} \sin(2kr_i + \Phi_0) \tag{5.1}$$

where N_i is the number of atoms in the N^{th} shell, r_i is the interatomic distance between the atom of interest and the i^{th} neighbor, A_i is the amplitude of the backscattered electron, and Φ_0 is the phase shift of the electron.

5.4 Results and Analysis

5.4.1 Core-Shell Geometry

Experimental observation via EXAFS by my experimental colleagues have indicated that Pt-Pt distance in pure Pt, Pt/TiWN and Pt/TiWC NPs are nearly identical, indicating that the Pt shell layer retained its own lattice without adopting that of the underlying substrate. Similar results have been observed in other core-shell systems [185, 186]. It is also worth noting that the employment of the HQE method to prepare a periodic slab for theoretical simulation is essential in obtaining this realistic structure that matches experimental Pt-Pt distances [2]. To obtain the periodic slabs that mostly closely resemble experimental structure for meaningful comparison, three starting structures of Pt layers of varying numbers of Pt atoms (16, 18 and 21) per layer in the unit cell are obtained via HQE for TiWN and TiWC respectively. The average distances between Pt-Pt are measured and presented in Table 5.1.

Species	Pt-Pt Distance (Å)
16 Pt Atoms on TiWN	2.95
18 Pt Atoms on TiWN	2.71
21 Pt Atoms on TiWN	2.58
16 Pt Atoms on TiWC	3.06
18 Pt Atoms on TiWC	2.81
21 Pt Atoms on TiWC	2.67
Pt (111)	2.70

Table 5.1: Average Pt-Pt Distance in Pt Shell for HQE-obtained Structures

The more atoms per layer they smaller the average distance as expected. The structures of 18 Pt Atoms on TiWN and 21 Pt Atoms on TiWC are chosen as they have the closest Pt-Pt distance to Pt (111) surface. Schematics of these slabs are shown in Figure 5-2. Since geometric effects are not significant given the similar Pt-Pt bond distances in pure Pt and Pt coated core-shell NPs, we need to look at ligand effects arising from bonding interactions between the Pt shell and the TiWC or TiWN core to further understand the difference in their catalytic behaviors.

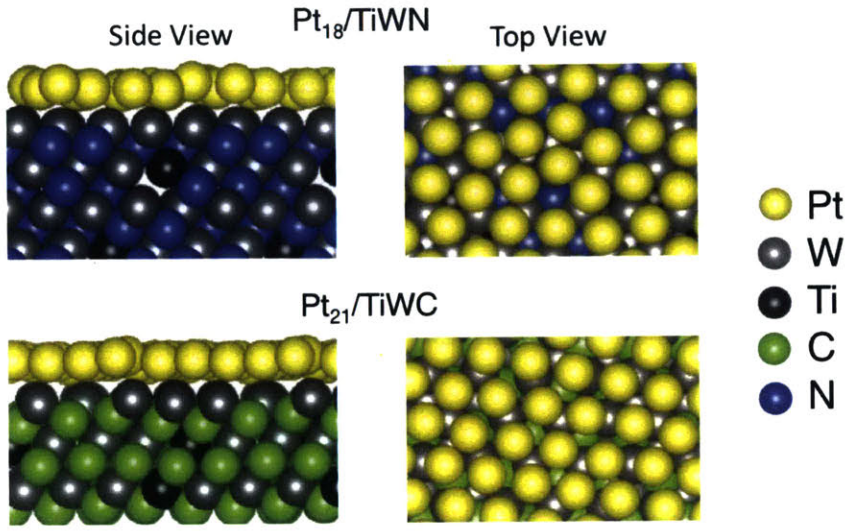

Figure 5-2: Representative slab models for Pt/TiWC (top) and Pt/TiWN (bottom) used in DFT calculations.

5.4.2 Changes in Electronic Structure due to Core-Shell Interaction

We posit that the observed difference in CO microcalorimetry and ethylene hydrogenation are due to changes in CO adsorption energies as well as the adsorption energies of key species in ethylene hydrogenation, namely, ethylene and hydrogen. To understand these changes, we first analyze the d bands of surface Pt on pure Pt, Pt/TiWN and Pt/TiWC as they hybridize with the bonding orbital of the adsorbates to form bonding and antibonding states [187] and are thus key to understanding shifts in adsorption energies. A schematic of the d-band model is shown in Figure 5-3. When the metal d-band center increases with respect to the Fermi level, the antibonding (d-σ)* orbital becomes less filled and therefore stabilizes the metal-adsorbate bond.

As shown in the PDOS plot (Figure 5-4), Pt/TiWN has the lowest d-band center of -2.94 eV, followed by Pt/TiWC's -2.87 eV. Pt(111) has the highest d-band center at -2.37 eV relative to the Fermi level. We also observe the broadening of d-bands in

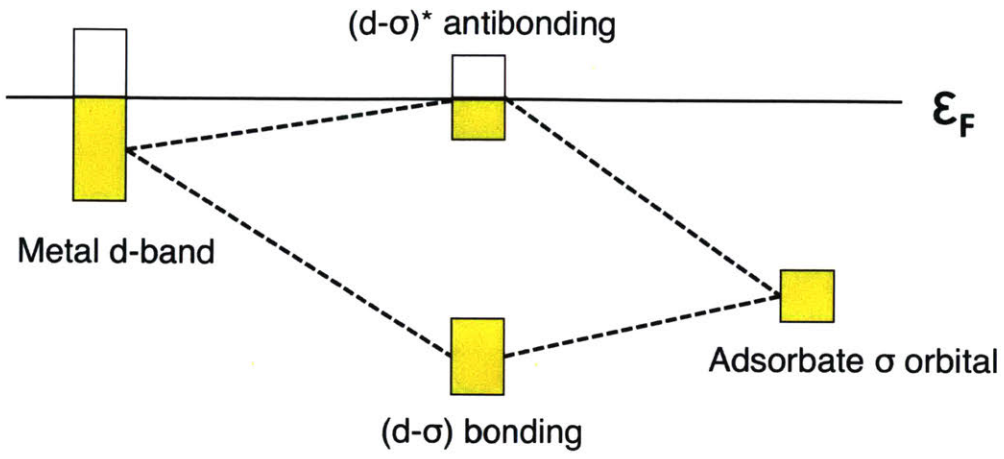

Figure 5-3: Schematics of the d-band model.

the core-shell materials as the standard deviation of d-band energies for Pt increase from 2.12 eV in Pt (111) to 2.30 eV in Pt/TiWC and 2.31 eV in Pt/TiWN. As W has a large coupling matrix which quantifies the span of metal d-states [61], hybridization of the shell Pt and core W d-states causes the d-band broadening of Pt by increasing the d orbital overlap and a more extensive splitting of the orbital energy levels [188].

Compared to Pt, W has a large coupling matrix element, which is a measure of the extent of the metal d states [61]. Thus, hybridization of the Pt and W d states result in increased d orbital overlap for Pt and a consequently broadened d-band. The d-band model also states that upon changes in the bandwidth, the d-band center relative to the Fermi level should move higher or lower in energy in order to conserve the d-band filling, and in this case, broadening of the Pt d-band caused a downshift of the d-band center.

We further investigate if charge transfer from W to Pt could have played a role in altering the Pt-states. Contour plots of the transferred charge density (Figure 5-5) indicates a small charge transfer from W to Pt as W has a lower work function compared to Pt. To quantify this, we plot the charge population analysis from the integrated PDOS (Figure 5-6). The overall filling of Pt s, p and d states show an increase for both Pt/TiWC and Pt/TiWN. This charge transfer effect could have

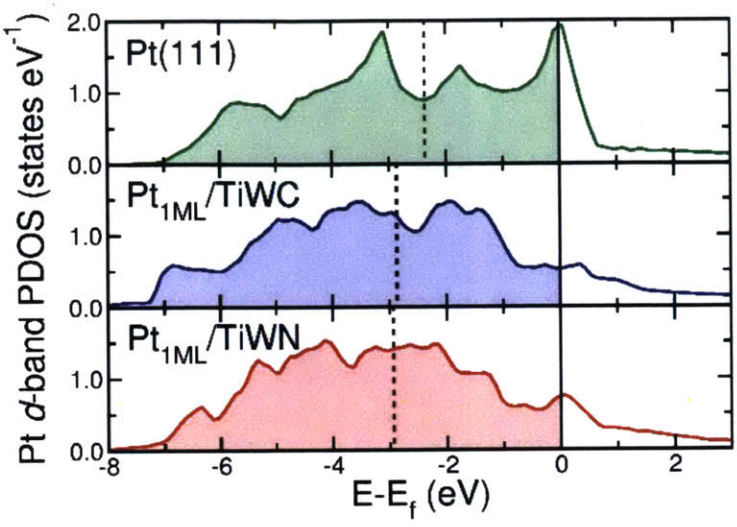

Figure 5-4: Calculated Pt valence d band PDOS and d band centers aligned to the Fermi level energy.

further contributed to the downshifting of d band centers in the core-shell NPs.

To summarize, we conclude that both band broadening due to the hybridization of the d states between Pt and W, as well as charge transfer led to the downshifting of the Pt d-band center. As shown in Figure 5-7, in order to preserve d-band filling in light of the ligand effects due to interactions with the carbide and nitride core, the Pt d band center lowers to conserve d band filling [188].

After analyzing the electronic structure of Pt, we proceed to explain the observed differences in the adsorption and catalytic behavior of pure Pt and Pt core-shell NPs. We can elucidate the CO microcalorimetry results based on the d band center shifts of the core-shell NPs. A downshifted Pt d band in Pt/TiWN and Pt/TiWC results in an increase in filling of the antibonding states (d-σ)* of the CO-NP adsorption system and therefore destabilizes the adsorption, leading to negligible heat traces from CO adsorption on these materials compared to pure Pt NPs. This is further corroborated by in-situ Pt L_2-edge XANES measurements conducted by my experimental colleagues of NP samples under 10% CO/90% He flow at room temperature [156] (Figure 5-8) which showed a considerable increase in empty antibonding states upon CO adsoprtion on Pt NPs compared to samples in environments with no CO flow, indicating

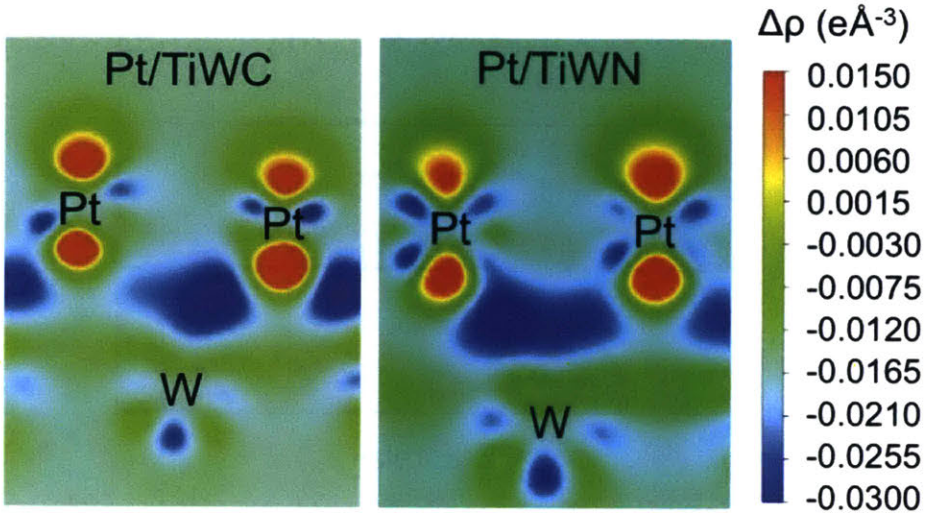

Figure 5-5: Contour plots of interatomically transferred charge density between Pt and W in Pt/TiWC and Pt/TiWN.

strong adsorption [189]. In contrast, with or without CO, the spectra of Pt/TiWN and Pt/TiWC remain unchanged, indicating no strong adsorption. Similarly, in the case of ethylene hydrogenation, we conclude that the weakening in reactant binding due to the downshifted d band center in Pt/TiWN and Pt/TiWC is a likely cause of the reduced TOFs compared to pure Pt NPs as weaker reactant binding on the catalyst reduces the rate at which the reaction could proceed.

5.4.3 Pt $5d_{3/2}$ and Pt $5d_{5/2}$ States

DFT calculation has revealed that there is charge transfer to the Pt shell from the cores (Figure 5-6). However, XANES spectra revealed that Pt on core-shell NPs has more empty d-states than pure Pt NPs as indicated by the higher peaks of the former (Figure 5-9).

In order to reconcile this apparent contradiction, we need to recall the fact that Pt L_2-edge XANES only probes the $5d_{3/2}$ of Pt not the $5d_{5/2}$ states. We propose that although the total d occupancy increased slightly, the relative filling between

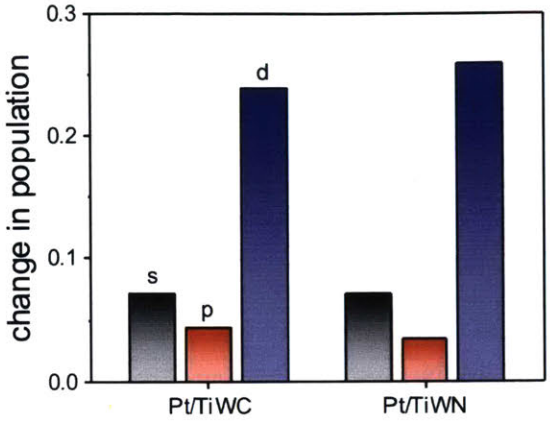

Figure 5-6: Change in Pt valence s, p, and d orbital populations for Pt/TiWC and Pt/TiWN relative to pure Pt calculated from the integrated PDOS.

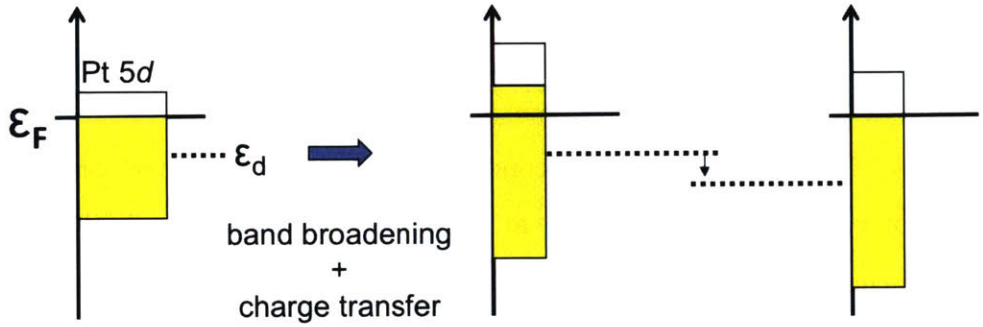

Figure 5-7: Schematic representation of changes to the Pt d-band electronic structure in core-shell NPs. Hybridization of Pt and W states and charge transfer from W to Pt lead to a downshift in the d band center to preserve the band filling

$5d_{3/2}$ and $5d_{5/2}$ states can change as a result of band broadening [190]. Assuming the spin-orbit coupling energy between the $5d_{3/2}$ and $5d_{5/2}$ states remains the same, the larger energy separation between the d orbitals in broadened d-bands should promote the filling of $5d_{5/2}$ states and decrease the filling of $5d_{3/2}$ states [190]. Thus, the increase in L_2-edge white line intensity should not be attributed to an overall increase in unoccupied d states, but rather to d-band broadening resulting in a lower $5d_{3/2}$ occupancy and a higher $5d_{5/2}$ occupancy. A schematic of this hypothesis is presented in Figure 5-10.

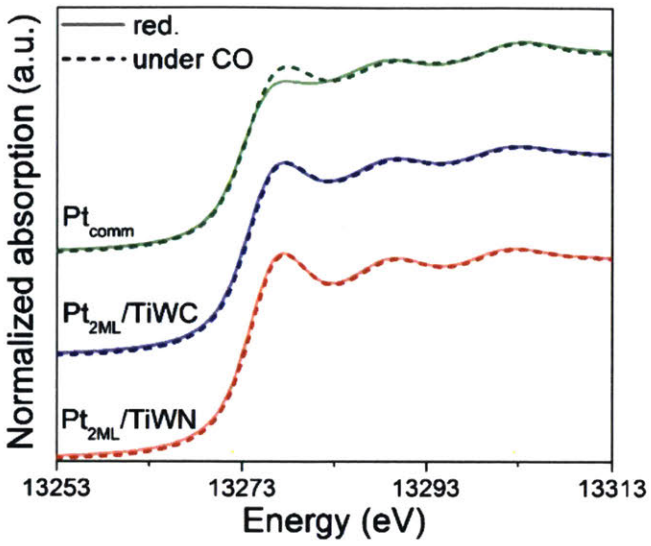

Figure 5-8: Pt L_2-edge XANES spectra for Pt, Pt/TiWC, and Pt/TiWN after reduction under H_2 and followed by 10% CO/90% He flow at room temperature.

5.4.4 Effect of Core Oxidation

The last piece of the puzzle to be solved concerns the varied behavior of core-shell NPs as catalysts for ethylene hydrogenation at different temperatures - TOFs drops an order of magnitude as the temperature under which the core-shell NPs are prepared drops from 200° to 600° (Figure 5-12b). We postulate that one cause for the change could be due to the fact that the core was not completely reduced at 200° as it is at higher temperatures. Previous experiments indicated that W oxides require a high temperature to be complete reduced [191]. Although the Pt shell is modeled by DFT as fully covering the core, in experiments, pinholes and inhomogeneities in the Pt coverage could allow the surface of TiWC and TiWN to be partially oxidized. These surface W oxides could then disrupt the interface interactions between the core and the shell Pt atoms.

We calculated the oxygen adsorption energies for the core materials which revealed fairly strong oxygen binding for both TiWC (-5.38 eV) and TiWN (-3.72 eV). We then constructed slab models with an oxygen atom intercalated between the core and the shell as shown in Figure5-11. By analyzing the d-band structure of Pt on top of clean TiWN/TiWC compared to that with an oxygen intercalated, we find that the latter

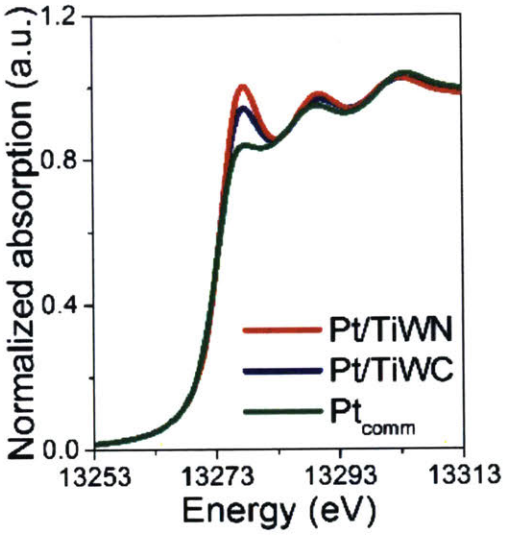

Figure 5-9: Pt L_2-edge XANES spectra for Pt, Pt/TiWC, and Pt/TiWN after reduction under H_2.

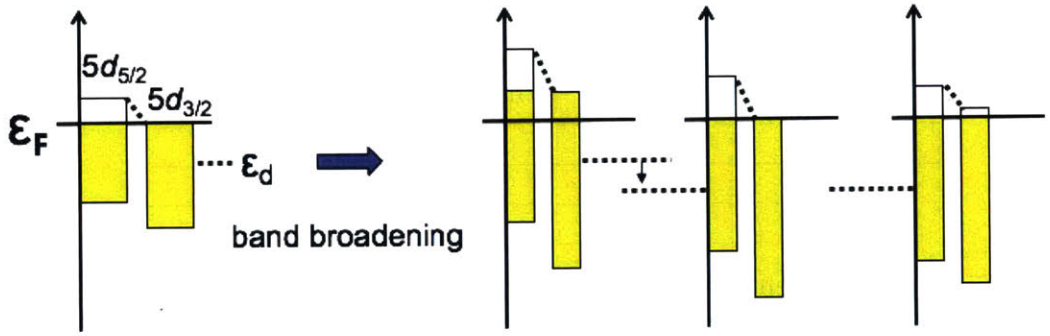

Figure 5-10: Schematics showing a downshift in the d-band center to preserve the band filling, and a shift in the $5d_{3/2}$ and $5d_{5/2}$ occupancies.

resulted in a slightly less downshifted Pt d band center compared to (Tabl e5.2). The d band center of Pt with O intercalation is still significantly lower that that of pure Pt (111). However, the d band center shift due to ligand effect of the core was reduced when W oxides are present on the core surface.

These results are further confirmed by the fact that Pt L_2-edge peak increased considerably after re-carburization at 600°, supporting the hypothesis that surface W oxidation weakened the interaction between the Pt shell and the TiWC core at lower temperatures (Figure 5-12a). In addition, analysis of the in situ W L_3-edge EXAFS spectra after re-carburization confirmed that W oxides were depleted and that the

re-carburized TiWC core features matched closely with those of an unoxidized carbide structure.

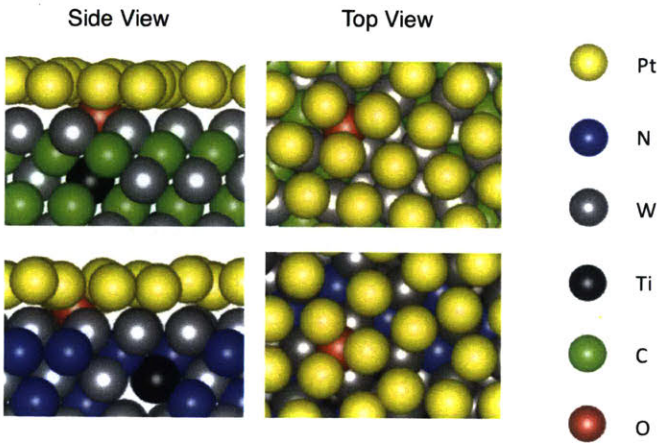

Figure 5-11: Schematics showing oxygen intercalated between Pt shell and te TiWN/TiWC cores.

Species	clean (eV)	with O intercalation (eV) (Å)
Pt (111)	-2.37	–
Pt/TiWC	-2.87	-2.82 (-2.72*)
Pt/TiWN	-2.94	-2.87 (-2.84*)

Table 5.2: Pt d-band centers from DFT calculations comparing with and without an oxygen atom intercalated between the Pt overlayer and either TiWC or TiWN. * indicates Pt d-band center for the 3 Pt atoms closest to the oxygen atom.

Therefore, the higher TOFs for the core-shell NPs prepared at 200° as compared to 600° result from the fact that the presence of surface W oxides on the core shifts the d band center of Pt up compared to a clean core without W oxides. Consequently, the adsorption system has a less filled antibonding state, resulting in stronger adsoprtion. This strong binding of ethylene and hydrogen leads to higher TOFs as the surface coverage of adsorbates are increased.

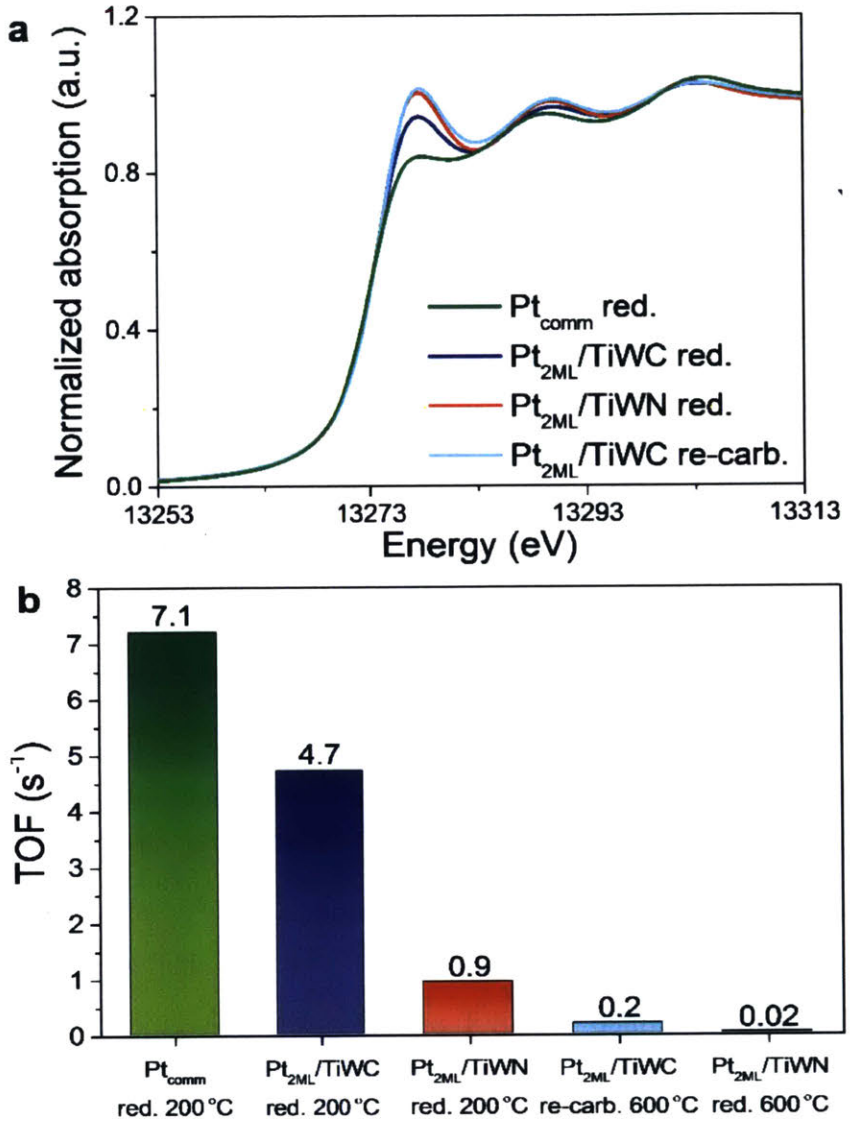

Figure 5-12: (a) Pt L_2-edge XANES spectra for Pt, Pt/TiWC, and Pt/TiWN after reduction under H_2 at 300° and Pt/TiWC after re-carburization under CH_4/H_2 at 600°. (b) TOF for ethylene hydrogenation at 45° with C_2H_4:H_2 ratio = 1:1 after sample pretreatment by reduction under H_2 or re-carburization under C_2H_4:H_2.

5.5 Conclusion

In this study, we have shown with DFT calculations how the electronic structures of Pt is modified from its bulk state as interacts with core materials TiWC and TiWN. Our simulation confirmed, together with experimental evidence that Pt does not match the lattice of the core material but instead maintains a Pt-Pt distance almost the

same as pure Pt NPs. Therefore, we trace these electronic structure modifications to ligand effect arising from Pt interacting with cores rather than strain effects. Through further analysis, we determined that the broadening of Pt d band as it hybridizes with W d states, as well as charge transfer from W to Pt lead to a lower d band center for Pt in Pt/TiWN and Pt/TiWC compared to pure Pt. Consequently, these core-shell NPs binds less strongly to adsorbates due to the more filled antibonding states in the adsorbant-adsorbate system accoridng to the d-band model. This conclusion explains CO microcalorimetry measurements which showed weaker CO binding, as well as the lower TOFs observed for ethylene hydrogenation on Pt/TiWN and Pt/TiWC compared to pure Pt.

Furthermore, we revealed that at low temperatures, partial oxidation of the W core leads to a shell Pt d band center that is closer to that of pure Pt, therefore resulting in stronger binding of adsorbates. This explains the temperature effect on the reactivities of ethylene hydrogenations.

This theoretical investigation not only explained experimentally observed changes in catalytic behaviors of TMNs and TMCs compared to TM NPs, but also demonstrated the importance of a detailed understanding of the electronic structure on elucidating the structural and chemical properties of core-shell materials. The detailed physical insights obtained via DFT provide invaluable guidance for the future design of catalysts that could be tuned for reduced CO poisoning in reactions such as hydrogen oxidation reaction which suffers from CO poisoning on pure Pt, as well as catalysts for selective hydrogenation reactions.

Chapter 6

Summary and Outlook

6.1 Summary

In this thesis, I presented efforts on two key fronts of designing optimal catalysts for a sustainable future built on renewable energy sources.

Firstly, on the efficiency front, I discussed a new activity volcano based on the recently discovered reaction mechanism with oxygen participation from the catalyst perovskite oxide itself for the oxygen evolution reaction, the bottleneck of electrochemical water splitting. Using model systems representing perovskite oxides with different binding strength to oxygen, I proposed for the first time a thermodynamic driving force for oxygen participation from the catalyst, not based on abstract descriptors but fundamental physical properties of transition metals derived from the periodic table. I extended this explanation further to include subsurface oxygen vacancies as experimentally synthesized perovskites are often nonstoichiometric. I introduced a method of gauging a perovskite's reactivity tolerance to oxygen vacancy, namely, the varying degrees of stress imposed on the transition metals based on their most stable oxidation state. In addition, I considered the effect of competing reactions and the solvent environment, thus demonstrating oxygen participation is feasible on moderately binding perovskites with these factors taken into account.

Secondly, on the cost front, I collaborated with experimental colleagues to elucidate how the electronic structure of noble metal Pt is modified in core-shell nanoparticle architectures where a monolayer thickness Pt shell surrounds a TiWN or TiWC core. Specifically, I isolated ligand effect as the key driver of Pt electronic structure modification instead of geometric effects. In addition, I used a d-band model taking into account the limitations of experimentally probing the empty d-states of Pt due to spin-orbit coupling to explain the observed catalytic activity modifications measured by my experimental colleagues. Lastly, I investigated the effect of core oxidation on the shell's electronic structure and provided an additional route to shell modification.

6.2 Outlook

On the perovskite front, the following are the two most intriguing areas of future research to me.

Firstly, the emergence of a brand new activity volcano for OER with a lower theoretical over potential compared to the consensus mechanism points to one thing - the discovery of new mechanisms is a promising route to break scaling relations of catalysis and reduce overpotentials. One class of reaction mechanisms that hasn't been explored thoroughly at the writing of thesis is that involving mixed B-sites. The 'synergy' often observed in certain transition metal combinations such as Fe and Ni of course can be attributed to eletronic effects. However, it is also possible that new reaction mechanisms that involve multiple reaction sites for different steps is the key in reducing reaction barriers. For example, given how sensitive the reaction barrier is to transition metal's tolerance to extra electron, it would be favorable for reaction steps that prefer an electronegative environment to take place on later transition metals and vice versa.

Secondly, in order to further tune the charges on the reactive sites, more complex perovskite structures can be exploited. The work done in this thesis is based on simple perovskites with the chemical formula ABO_3, there are more complex layered perovskites where the ABO_3 units are separated by sheets of other compositions. For example, in Ruddlesden-Popper phase perovskites, the ABO_3 layers are sandwiched between two AO layers (rocksalt layer). The Ruddlesden-Popper phase series has the general formula $A_{n+1}B_nO_{3n+1}$, where n indicates how many layers of ABO_3 is sandwiched between two AOs. A schematics representing the Ruddlesden-Popper phase for n=1, 2, and 3 is shown in Figure 6-1.

Taking the Ruddlesden-Popper phase of $LaNiO_3$ as a model system, I have conducted preliminary research to examine how this phase alters the electronic structure of perovskites and the trend as n increases. I first investigated the charge distribution on A and B sites compared to the simple $LaNiO_3$ structure. In terms of bulk charge distribution (Figure 6-2), we can see that as n increases, the bader charge on

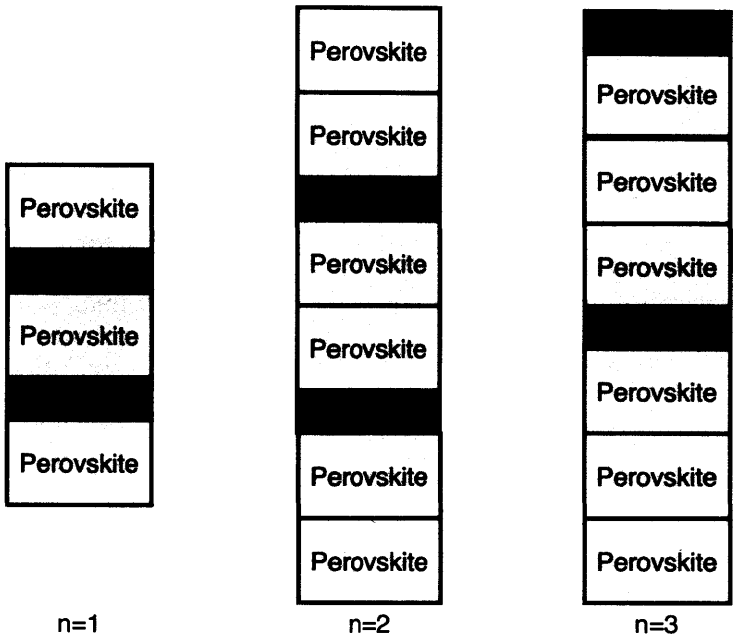

Figure 6-1: Schematics showing structures of n=1, 2 and 3 Ruddlesden-Popper phase perovskites.

both the A sites and B sites increases while that in the rocksalt insertions do not change. On the BO terminated surface (Figure 6-3), the charge of the B site where both AEM and LOM take place can also be tuned by varying n. This indicates that we now have another dimension, in addition to changing B site elements that can be exploited to tune perovskite properties which is how much AO insertion there is. Most importantly, as Ruddlesden-Popper phase have been shown to be more stable than simple perovskite phases in certain compositions, we can possibly also improve the stability and therefore the durability of this class of OER catalysts through this route [192].

On the core-shell nanoparticle front, I propose the following two routes for further research.

Firstly, the HQE method employed in this thesis requires tremendous computational efforts. Due to the significant number of steps of ab initio molecular dynamics involved, the size of the periodic slab is limited and investigations of thicker shell layers impose further computational cost. However, as obtaining accurate geometrical structures for core-shell nanoparticles is extremely important (in our case, if the Pt-Pt

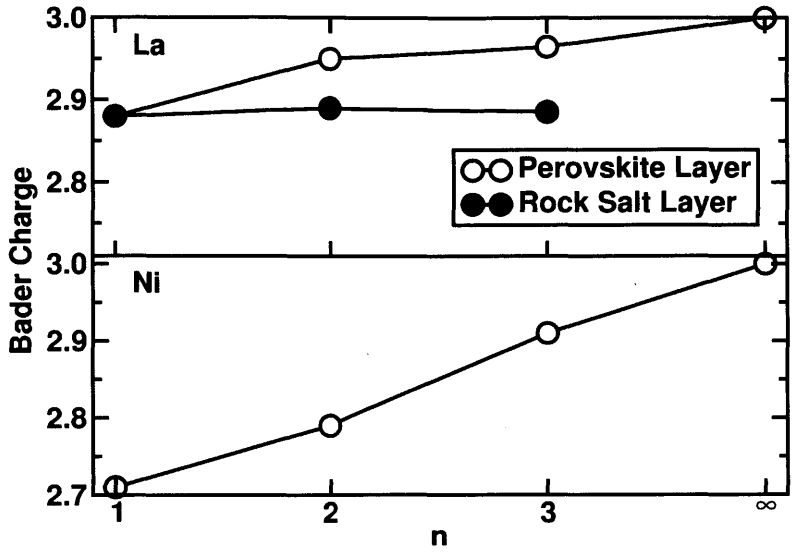

Figure 6-2: Bader charge on La and Ni of bulk n=1, 2 and 3 Ruddlesden-Popper phase perovskites. Simple perovskite $LaNiO_3$ is denoted as n=∞ since there is no AO insertion.

distance is not accurate, we could have attributed the electronic structure modification to strain effects), one cannot simply resolve to geometry optimization without HQE to save computational cost since the geometry obtained have been proven to be unrealistic [2]. Therefore, new methods should be explored that strike a compromise between obtaining accurate structure and reducing computational cost. Though none has been applied to core-shell nanoparticles, there are promising machine learning algorithms that explore the phase space of surface structures more efficiently than iterating through them one by one with DFT. For example, some of them employ genetic algorithm [193–195], some employ Gaussian process [196] and ab initio grand canonical Monte Carlo [197]. The feasibility of these methods as applied to core-shell surfaces and interfaces can be tested to reliably speed up the identification of realistic structures for this class of materials. The eventual goal is to produce phase diagrams for many core-shell combinations of interest at various temperatures and gas pressures, so that the d band center of the surface can be precisely pinpointed and selected for reactions of interest.

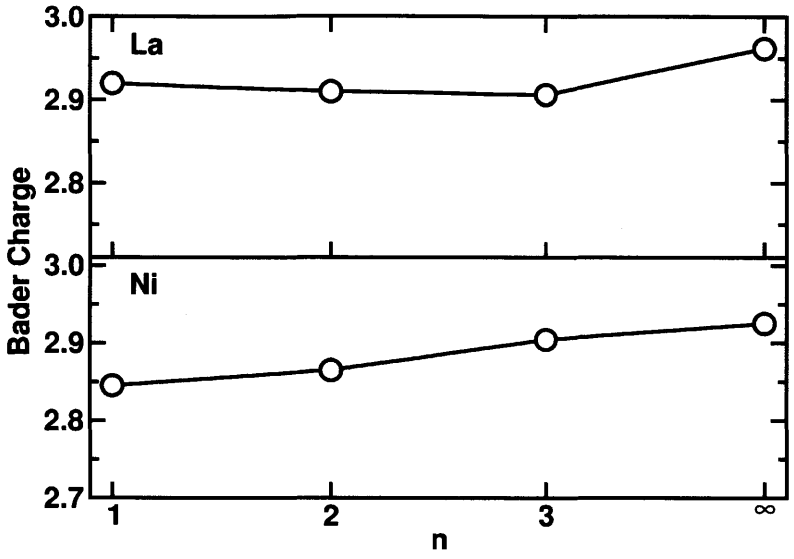

Figure 6-3: Bader charge on surface layer of Ni and subsurface layer of La for BO terminated n=1, 2 and 3 Ruddlesden-Popper phase perovskites. The subsurface layer is chosen to be the inserted AO layer to examine maximum deviation from the surfaces of BO terminated simple perovskites. Simple perovskite $LaNiO_3$ is denoted as n=∞ since there is no AO insertion.

With a more efficient way of obtaining structures that reflect the experimental reality, the next step is to explore the stability and activity of many combinations of core-shell materials for a wide range of catalytic reactions that currently require pure noble metal or other rare or expensive catalysts. As this thesis has demonstrated, one interesting property of Pt/TiWN and Pt/TiWC is that the extent of core oxidation is temperature-sensitive and therefore Pt's electronic structure is modified to different extents at different temperatures of reduction. This property would allow us to selectively tune core-shell materials based on the required reaction temperature of particular reactions. With reliable starting structures, we can then set out to explore the interaction of surfaces with a wide range of substrates of interests and obtain free energy diagrams starting with a cheaper core-shell surface with d band characteristics that most closely resemble the best catalyst available.

Bibliography

[1] A. Nilsson, L. Pettersson, B. Hammer, T. Bligaard, C. H. Christensen, and J. K. Nørskov, "The electronic structure effect in heterogeneous catalysis," *Catalysis Letters*, vol. 100, no. 3-4, pp. 111–114, 2005.

[2] C. H. Hendon, S. T. Hunt, M. Milina, K. T. Butler, A. Walsh, and Y. Romn-Leshkov, "Realistic surface descriptions of heterometallic interfaces: the case of tiwc coated in noble metals," *The journal of physical chemistry letters*, vol. 7, no. 22, pp. 4475–4482, 2016.

[3] R. U. Ayres and B. Warr, *The economic growth engine: how energy and work drive material prosperity*. Edward Elgar Publishing, 2010.

[4] H. Safa, "The impact of energy on global economy," 2017.

[5] I. C. Man, H.-Y. Su, F. Calle-Vallejo, H. A. Hansen, J. I. Martínez, N. G. Inoglu, J. Kitchin, T. F. Jaramillo, J. K. Nørskov, and J. Rossmeisl, "Universality in oxygen evolution electrocatalysis on oxide surfaces," *ChemCatChem*, vol. 3, no. 7, pp. 1159–1165, 2011.

[6] G. W. Huber, S. Iborra, and A. Corma, "Synthesis of transportation fuels from biomass: chemistry, catalysts, and engineering," *Chemical reviews*, vol. 106, no. 9, pp. 4044–4098, 2006.

[7] V. M. Goldschmidt, "Die gesetze der krystallochemie," *Naturwissenschaften*, vol. 14, no. 21, pp. 477–485, 1926.

[8] M. Pena and J. Fierro, "Chemical structures and performance of perovskite oxides," *Chemical reviews*, vol. 101, no. 7, pp. 1981–2018, 2001.

[9] H. Kagan and J. Namy, "Handbook on the physics and chemistry of rare earths," *by KA Gschneider and L. Eyring, Elsevier, Amsterdam*, p. 525, 1984.

[10] J. Goodenough and J. Longo, "Magnetic and other properties of oxides and related compounds, landolt-börnstein, numerical data and functional relations in science and technology, new series vol. iii. 4," 1970.

[11] J. Goodenough, "Solid state chemistry ed cnr rao," 1974.

[12] Y. Han, M. Harmer, Y. Hu, and D. Smyth, "A++/ti nonstoichiometry in alkaline earth titanates, ati0 3," in *Transport in Nonstoichiometric Compounds*, pp. 73–85, Springer, 1985.

[13] A. K. Opitz, A. Nenning, C. Rameshan, R. Rameshan, R. Blume, M. Hävecker, A. Knop-Gericke, G. Rupprechter, J. Fleig, and B. Klötzer, "Enhancing electrochemical water-splitting kinetics by polarization-driven formation of near-surface iron (0): An in situ xps study on perovskite-type electrodes," *Angewandte Chemie International Edition*, vol. 54, no. 9, pp. 2628–2632, 2015.

[14] Y. Zhu, W. Zhou, and Z. Shao, "Perovskite/carbon composites: applications in oxygen electrocatalysis," *Small*, vol. 13, no. 12, p. 1603793, 2017.

[15] E. Fabbri, M. Nachtegaal, T. Binninger, X. Cheng, B.-J. Kim, J. Durst, F. Bozza, T. Graule, R. Schäublin, L. Wiles, *et al.*, "Dynamic surface self-reconstruction is the key of highly active perovskite nano-electrocatalysts for water splitting," *Nature materials*, vol. 16, no. 9, p. 925, 2017.

[16] Y. Teraoka, K. Nakano, S. Kagawa, and W. Shangguan, "Simultaneous removal of nitrogen oxides and diesel soot particulates catalyzed by perovskite-type oxides," *Applied Catalysis B: Environmental*, vol. 5, no. 3, pp. L181–L185, 1995.

[17] H. Jiang, H. Wang, F. Liang, S. Werth, T. Schiestel, and J. Caro, "Direct decomposition of nitrous oxide to nitrogen by in situ oxygen removal with a perovskite membrane," *Angewandte Chemie International Edition*, vol. 48, no. 16, pp. 2983–2986, 2009.

[18] Y. Nishihata, J. Mizuki, T. Akao, H. Tanaka, M. Uenishi, M. Kimura, T. Okamoto, and N. Hamada, "Self-regeneration of a pd-perovskite catalyst for automotive emissions control," *Nature*, vol. 418, no. 6894, p. 164, 2002.

[19] P. Li, S. Ouyang, G. Xi, T. Kako, and J. Ye, "The effects of crystal structure and electronic structure on photocatalytic h2 evolution and co2 reduction over two phases of perovskite-structured nanbo3," *The Journal of Physical Chemistry C*, vol. 116, no. 14, pp. 7621–7628, 2012.

[20] Y.-F. Xu, M.-Z. Yang, B.-X. Chen, X.-D. Wang, H.-Y. Chen, D.-B. Kuang, and C.-Y. Su, "A cspbbr3 perovskite quantum dot/graphene oxide composite for photocatalytic co2 reduction," *Journal of the American Chemical Society*, vol. 139, no. 16, pp. 5660–5663, 2017.

[21] S. Zeng, P. Kar, U. K. Thakur, and K. Shankar, "A review on photocatalytic co2 reduction using perovskite oxide nanomaterials," *Nanotechnology*, vol. 29, no. 5, p. 052001, 2018.

[22] N. J. Jeon, J. H. Noh, W. S. Yang, Y. C. Kim, S. Ryu, J. Seo, and S. I. Seok, "Compositional engineering of perovskite materials for high-performance solar cells," *Nature*, vol. 517, no. 7535, p. 476, 2015.

[23] W. Nie, H. Tsai, R. Asadpour, J.-C. Blancon, A. J. Neukirch, G. Gupta, J. J. Crochet, M. Chhowalla, S. Tretiak, M. A. Alam, *et al.*, "High-efficiency solution-processed perovskite solar cells with millimeter-scale grains," *Science*, vol. 347, no. 6221, pp. 522–525, 2015.

[24] M. Saliba, T. Matsui, K. Domanski, J.-Y. Seo, A. Ummadisingu, S. M. Zakeeruddin, J.-P. Correa-Baena, W. R. Tress, A. Abate, A. Hagfeldt, *et al.*, "Incorporation of rubidium cations into perovskite solar cells improves photovoltaic performance," *Science*, vol. 354, no. 6309, pp. 206–209, 2016.

[25] Y.-H. Huang, R. I. Dass, Z.-L. Xing, and J. B. Goodenough, "Double perovskites as anode materials for solid-oxide fuel cells," *Science*, vol. 312, no. 5771, pp. 254–257, 2006.

[26] S. Sengodan, S. Choi, A. Jun, T. H. Shin, Y.-W. Ju, H. Y. Jeong, J. Shin, J. T. Irvine, and G. Kim, "Layered oxygen-deficient double perovskite as an efficient and stable anode for direct hydrocarbon solid oxide fuel cells," *Nature materials*, vol. 14, no. 2, p. 205, 2015.

[27] C. Duan, D. Hook, Y. Chen, J. Tong, and R. O'Hayre, "Zr and y co-doped perovskite as a stable, high performance cathode for solid oxide fuel cells operating below 500 c," *Energy & Environmental Science*, vol. 10, no. 1, pp. 176–182, 2017.

[28] J. Hwang, R. R. Rao, L. Giordano, Y. Katayama, Y. Yu, and Y. Shao-Horn, "Perovskites in catalysis and electrocatalysis," *Science*, vol. 358, no. 6364, pp. 751–756, 2017.

[29] H. B. Gray, "Powering the planet with solar fuel," *Nature chemistry*, vol. 1, no. 1, p. 7, 2009.

[30] U. Babic, M. Suermann, F. N. Büchi, L. Gubler, and T. J. Schmidt, "Critical reviewidentifying critical gaps for polymer electrolyte water electrolysis development," *Journal of The Electrochemical Society*, vol. 164, no. 4, pp. F387–F399, 2017.

[31] M. Carmo, D. L. Fritz, J. Mergel, and D. Stolten, "A comprehensive review on pem water electrolysis," *International journal of hydrogen energy*, vol. 38, no. 12, pp. 4901–4934, 2013.

[32] E. Fabbri and T. J. Schmidt, "Oxygen evolution reactionthe enigma in water electrolysis," 2018.

[33] R. Schmalensee, *The future of solar energy: an interdisciplinary MIT study.* Energy Initiative, Massachusetts Institute of Technology, 2015.

[34] A. Mudipalli *et al.*, "Lead hepatotoxicity & potential health effects," *Indian Journal of Medical Research*, vol. 126, no. 6, p. 518, 2007.

[35] D. Linden and T. B. Reddy, *Handbook of batteries.* McGraw-Hill Professional, 2002.

[36] W. M. Haynes, "Crc handbook of chemistry and physics, june 9, 2015 by crc press."

[37] J. Bravo-Suárez, R. Chaudhari, and B. Subramaniam, "Design of heterogeneous catalysts for fuels and chemicals processing: An overview," *Novel materials for catalysis and fuels processing*, vol. 1132, pp. 3–68, 2013.

[38] A. Ashcroft, A. Cheetham, J. a. Foord, M. Green, C. Grey, and A. Murrell, "Selective oxidation of methane to synthesis gas using transition metal catalysts," *Nature*, vol. 344, no. 6264, p. 319, 1990.

[39] N. Cheng, S. Stambula, D. Wang, M. N. Banis, J. Liu, A. Riese, B. Xiao, R. Li, T.-K. Sham, L.-M. Liu, *et al.*, "Platinum single-atom and cluster catalysis of the hydrogen evolution reaction," *Nature communications*, vol. 7, p. 13638, 2016.

[40] M. Wakisaka, S. Mitsui, Y. Hirose, K. Kawashima, H. Uchida, and M. Watanabe, "Electronic structures of pt- co and pt- ru alloys for co-tolerant anode catalysts in polymer electrolyte fuel cells studied by ec- xps," *The Journal of Physical Chemistry B*, vol. 110, no. 46, pp. 23489–23496, 2006.

[41] R. Forgie, G. Bugosh, K. Neyerlin, Z. Liu, and P. Strasser, "Bimetallic ru electrocatalysts for the oer and electrolytic water splitting in acidic media," *Electrochemical and Solid-State Letters*, vol. 13, no. 4, pp. B36–B39, 2010.

[42] J. Zhang, M. P. Everson, T. J. Wallington, F. R. Field III, R. Roth, and R. E. Kirchain, "Assessing economic modulation of future critical materials use: The case of automotive-related platinum group metals," *Environmental science & technology*, vol. 50, no. 14, pp. 7687–7695, 2016.

[43] C.-J. Yang, "An impending platinum crisis and its implications for the future of the automobile," *Energy Policy*, vol. 37, no. 5, pp. 1805–1808, 2009.

[44] R. Wittstock, A. Pehlken, and M. Wark, "Challenges in automotive fuel cells recycling," *Recycling*, vol. 1, no. 3, pp. 343–364, 2016.

[45] P. C. Ghosh, "High platinum cost: obstacle or blessing for commercialization of low-temperature fuel cell technologies," *Clean Technologies and Environmental Policy*, vol. 19, no. 2, pp. 595–601, 2017.

[46] K. Sasaki, H. Naohara, Y. Choi, Y. Cai, W.-F. Chen, P. Liu, and R. R. Adzic, "Highly stable pt monolayer on pdau nanoparticle electrocatalysts for the oxygen reduction reaction," *Nature communications*, vol. 3, p. 1115, 2012.

[47] M. Shao, *Electrocatalysis in fuel cells: a non-and low-platinum approach*, vol. 9. Springer Science & Business Media, 2013.

[48] S. T. Hunt and Y. Romn-Leshkov, "Principles and methods for the rational design of core–shell nanoparticle catalysts with ultralow noble metal loadings," *Accounts of chemical research*, vol. 51, no. 5, pp. 1054–1062, 2018.

[49] P. Strasser, S. Koh, T. Anniyev, J. Greeley, K. More, C. Yu, Z. Liu, S. Kaya, D. Nordlund, H. Ogasawara, *et al.*, "Lattice-strain control of the activity in dealloyed core–shell fuel cell catalysts," *Nature chemistry*, vol. 2, no. 6, p. 454, 2010.

[50] Y. C. Kimmel, X. Xu, W. Yu, X. Yang, and J. G. Chen, "Trends in electrochemical stability of transition metal carbides and their potential use as supports for low-cost electrocatalysts," *ACS Catalysis*, vol. 4, no. 5, pp. 1558–1562, 2014.

[51] S. Oyama, "Preparation and catalytic properties of transition metal carbides and nitrides," *Catalysis today*, vol. 15, no. 2, pp. 179–200, 1992.

[52] S. T. Oyama, "Introduction to the chemistry of transition metal carbides and nitrides," in *The chemistry of transition metal carbides and nitrides*, pp. 1–27, Springer, 1996.

[53] H. H. Hwu and J. G. Chen, "Surface chemistry of transition metal carbides," *Chemical reviews*, vol. 105, no. 1, pp. 185–212, 2005.

[54] Z. Yan, M. Cai, and P. K. Shen, "Nanosized tungsten carbide synthesized by a novel route at low temperature for high performance electrocatalysis," *Scientific reports*, vol. 3, p. 1646, 2013.

[55] I. J. Hsu, Y. C. Kimmel, X. Jiang, B. G. Willis, and J. G. Chen, "Atomic layer deposition synthesis of platinum–tungsten carbide core–shell catalysts for the hydrogen evolution reaction," *Chemical Communications*, vol. 48, no. 7, pp. 1063–1065, 2012.

[56] R. Ganesan and J. S. Lee, "Tungsten carbide microspheres as a noble-metal-economic electrocatalyst for methanol oxidation," *Angewandte Chemie International Edition*, vol. 44, no. 40, pp. 6557–6560, 2005.

[57] S. T. Hunt, M. Milina, A. C. Alba-Rubio, C. H. Hendon, J. A. Dumesic, and Y. Román-Leshkov, "Self-assembly of noble metal monolayers on transition metal carbide nanoparticle catalysts," *Science*, vol. 352, no. 6288, pp. 974–978, 2016.

[58] A. Garg, M. Milina, M. Ball, D. Zanchet, S. T. Hunt, J. A. Dumesic, and Y. Román-Leshkov, "Transition-metal nitride core@ noble-metal shell nanoparticles as highly co tolerant catalysts," *Angewandte Chemie International Edition*, vol. 56, no. 30, pp. 8828–8833, 2017.

[59] S. T. Hunt, M. Milina, Z. Wang, and Y. Román-Leshkov, "Activating earth-abundant electrocatalysts for efficient, low-cost hydrogen evolution/oxidation:

sub-monolayer platinum coatings on titanium tungsten carbide nanoparticles," *Energy & Environmental Science*, vol. 9, no. 10, pp. 3290–3301, 2016.

[60] A. A. Peterson and J. K. Nørskov, "Activity descriptors for co2 electroreduction to methane on transition-metal catalysts," *The Journal of Physical Chemistry Letters*, vol. 3, no. 2, pp. 251–258, 2012.

[61] B. Hammer and J. Norskov, "Why gold is the noblest of all the metals," *Nature*, vol. 376, no. 6537, p. 238, 1995.

[62] S. Holloway, B. Lundqvist, and J. Nørskov, "Electronic factors in catalysis," in *Proceedings of the Eighth Conference on Catalysis*, vol. 4, p. 85, 1984.

[63] L. A. Kibler, A. M. El-Aziz, R. Hoyer, and D. M. Kolb, "Tuning reaction rates by lateral strain in a palladium monolayer," *Angewandte Chemie International Edition*, vol. 44, no. 14, pp. 2080–2084, 2005.

[64] T. Jiang, D. Mowbray, S. Dobrin, H. Falsig, B. Hvolbæk, T. Bligaard, and J. K. Nørskov, "Trends in co oxidation rates for metal nanoparticles and close-packed, stepped, and kinked surfaces," *The Journal of Physical Chemistry C*, vol. 113, no. 24, pp. 10548–10553, 2009.

[65] H. Xin and S. Linic, "Communications: Exceptions to the d-band model of chemisorption on metal surfaces: The dominant role of repulsion between adsorbate states and metal d-states," 2010.

[66] P. Sabatier, *Catalysis in organic chemistry*. D. Van Nostrand Company, 1922.

[67] J. Bronsted, "Acid and basic catalysis.," *Chemical Reviews*, vol. 5, no. 3, pp. 231–338, 1928.

[68] M. Evans and M. Polanyi, "Inertia and driving force of chemical reactions," *Transactions of the Faraday Society*, vol. 34, pp. 11–24, 1938.

[69] M. A. Barteau, "Linear free energy relationships for c 1-oxygenate decomposition on transition metal surfaces," *Catalysis Letters*, vol. 8, no. 2-4, pp. 175–183, 1991.

[70] J. Nørskov, T. Bligaard, A. Logadottir, S. Bahn, L. Hansen, M. Bollinger, H. Bengaard, B. Hammer, Z. Sljivancanin, M. Mavrikakis, Y. Xu, S. Dahl, and C. Jacobsen, "Universality in heterogeneous catalysis," *Journal of Catalysis*, vol. 209, pp. 275–278, July 2002.

[71] V. Pallassana and M. Neurock, "Electronic factors governing ethylene hydrogenation and dehydrogenation activity of pseudomorphic PdML/re(0001), PdML/ru(0001), pd(111), and PdML/au(111) surfaces," *Journal of Catalysis*, vol. 191, pp. 301–317, Apr. 2000.

[72] Z.-P. Liu and P. Hu, "General trends in CO dissociation on transition metal surfaces," *The Journal of Chemical Physics*, vol. 114, pp. 8244–8247, May 2001.

[73] A. Logadottir, T. Rod, J. Nørskov, B. Hammer, S. Dahl, and C. Jacobsen, "The brønsted–evans–polanyi relation and the volcano plot for ammonia synthesis over transition metal catalysts," *Journal of Catalysis*, vol. 197, pp. 229–231, Jan. 2001.

[74] A. Michaelides, Z.-P. Liu, C. J. Zhang, A. Alavi, D. A. King, and P. Hu, "Identification of general linear relationships between activation energies and enthalpy changes for dissociation reactions at surfaces," *Journal of the American Chemical Society*, vol. 125, pp. 3704–3705, Apr. 2003.

[75] M. Born and R. Oppenheimer, "Zur quantentheorie der molekeln," *Annalen der Physik*, vol. 389, no. 20, pp. 457–484, 1927.

[76] P. Hohenberg and W. Kohn, "Inhomogeneous electron gas," *Physical review*, vol. 136, no. 3B, p. B864, 1964.

[77] W. Kohn and L. J. Sham, "Self-consistent equations including exchange and correlation effects," *Physical review*, vol. 140, no. 4A, p. A1133, 1965.

[78] B. Hammer, L. B. Hansen, and J. K. Nørskov, "Improved adsorption energetics within density-functional theory using revised perdew-burke-ernzerhof functionals," *Physical Review B*, vol. 59, no. 11, p. 7413, 1999.

[79] K. Yang, J. Zheng, Y. Zhao, and D. G. Truhlar, "Tests of the RPBE, revPBE, -HCTHhyb, b97x-d, and MOHLYP density functional approximations and 29 others against representative databases for diverse bond energies and barrier heights in catalysis," *The Journal of Chemical Physics*, vol. 132, p. 164117, Apr. 2010.

[80] N. W. Ashcroft, N. D. Mermin, *et al.*, "Solid state physics by neil w. ashcroft and n. david mermin.," 1976.

[81] P. E. Blöchl, "Projector augmented-wave method," *Physical review B*, vol. 50, no. 24, p. 17953, 1994.

[82] G. Kresse and J. Furthmüller, "Efficient iterative schemes for ab initio total-energy calculations using a plane-wave basis set," *Physical review B*, vol. 54, no. 16, p. 11169, 1996.

[83] G. W. Watson, R. P. K. Wells, D. J. Willock, and G. J. Hutchings, "Density functional theory calculations on the interaction of ethene with the {111} surface of platinum," *The Journal of Physical Chemistry B*, vol. 104, pp. 6439–6446, July 2000.

[84] F. Calle-Vallejo, A. Krabbe, and J. M. García-Lastra, "How covalence breaks adsorption-energy scaling relations and solvation restores them," *Chemical Science*, vol. 8, no. 1, pp. 124–130, 2017.

[85] R. Christensen, H. A. Hansen, C. F. Dickens, J. K. Nørskov, and T. Vegge, "Functional independent scaling relation for ORR/OER catalysts," *The Journal of Physical Chemistry C*, vol. 120, pp. 24910–24916, Oct. 2016.

[86] K. Lejaeghere, G. Bihlmayer, T. Bjorkman, P. Blaha, S. Blugel, V. Blum, D. Caliste, I. E. Castelli, S. J. Clark, A. D. Corso, S. de Gironcoli, T. Deutsch, J. K. Dewhurst, I. D. Marco, C. Draxl, M. D. ak, O. Eriksson, J. A. Flores-Livas, K. F. Garrity, L. Genovese, P. Giannozzi, M. Giantomassi, S. Goedecker, X. Gonze, O. Granas, E. K. U. Gross, A. Gulans, F. Gygi, D. R. Hamann, P. J. Hasnip, N. A. W. Holzwarth, D. I. an, D. B. Jochym, F. Jollet, D. Jones, G. Kresse, K. Koepernik, E. Kucukbenli, Y. O. Kvashnin, I. L. M. Locht, S. Lubeck, M. Marsman, N. Marzari, U. Nitzsche, L. Nordstrom, T. Ozaki, L. Paulatto, C. J. Pickard, W. Poelmans, M. I. J. Probert, K. Refson, M. Richter, G.-M. Rignanese, S. Saha, M. Scheffler, M. Schlipf, K. Schwarz, S. Sharma, F. Tavazza, P. Thunstrom, A. Tkatchenko, M. Torrent, D. Vanderbilt, M. J. van Setten, V. V. Speybroeck, J. M. Wills, J. R. Yates, G.-X. Zhang, and S. Cottenier, "Reproducibility in density functional theory calculations of solids," *Science*, vol. 351, pp. aad3000–aad3000, Mar. 2016.

[87] J. S. Yoo, Y. Liu, X. Rong, and A. M. Kolpak, "Electronic origin and kinetic feasibility of the lattice oxygen participation during the oxygen evolution reaction on perovskites," *The journal of physical chemistry letters*, vol. 9, no. 7, pp. 1473–1479, 2018.

[88] J. S. Yoo, X. Rong, Y. Liu, and A. M. Kolpak, "Role of lattice oxygen participation in understanding trends in the oxygen evolution reaction on perovskites," *ACS Catalysis*, vol. 8, no. 5, pp. 4628–4636, 2018.

[89] M. G. Walter, E. L. Warren, J. R. McKone, S. W. Boettcher, Q. Mi, E. A. Santori, and N. S. Lewis, "Solar water splitting cells," *Chemical reviews*, vol. 110, no. 11, pp. 6446–6473, 2010.

[90] S. U. Khan, M. Al-Shahry, and W. B. Ingler, "Efficient photochemical water splitting by a chemically modified n-tio2," *science*, vol. 297, no. 5590, pp. 2243–2245, 2002.

[91] A. Kudo and Y. Miseki, "Heterogeneous photocatalyst materials for water splitting," *Chemical Society Reviews*, vol. 38, no. 1, pp. 253–278, 2009.

[92] A. J. Bard and M. A. Fox, "Artificial photosynthesis: solar splitting of water to hydrogen and oxygen," *Accounts of Chemical Research*, vol. 28, no. 3, pp. 141–145, 1995.

[93] T. J. Meyer, "Catalysis: the art of splitting water," *Nature*, vol. 451, no. 7180, p. 778, 2008.

[94] C. C. McCrory, S. Jung, J. C. Peters, and T. F. Jaramillo, "Benchmarking heterogeneous electrocatalysts for the oxygen evolution reaction," *Journal of the American Chemical Society*, vol. 135, no. 45, pp. 16977–16987, 2013.

[95] T. Reier, M. Oezaslan, and P. Strasser, "Electrocatalytic oxygen evolution reaction (oer) on ru, ir, and pt catalysts: a comparative study of nanoparticles and bulk materials," *Acs Catalysis*, vol. 2, no. 8, pp. 1765–1772, 2012.

[96] M. S. Burke, L. J. Enman, A. S. Batchellor, S. Zou, and S. W. Boettcher, "Oxygen evolution reaction electrocatalysis on transition metal oxides and (oxy) hydroxides: activity trends and design principles," *Chemistry of Materials*, vol. 27, no. 22, pp. 7549–7558, 2015.

[97] J. O. Bockris and T. Otagawa, "The electrocatalysis of oxygen evolution on perovskites," *Journal of the Electrochemical Society*, vol. 131, no. 2, pp. 290–302, 1984.

[98] W. T. Hong, M. Risch, K. A. Stoerzinger, A. Grimaud, J. Suntivich, and Y. Shao-Horn, "Toward the rational design of non-precious transition metal oxides for oxygen electrocatalysis," *Energy & Environmental Science*, vol. 8, no. 5, pp. 1404–1427, 2015.

[99] W. G. Hardin, J. T. Mefford, D. A. Slanac, B. B. Patel, X. Wang, S. Dai, X. Zhao, R. S. Ruoff, K. P. Johnston, and K. J. Stevenson, "Tuning the electrocatalytic activity of perovskites through active site variation and support interactions," *Chemistry of Materials*, vol. 26, no. 11, pp. 3368–3376, 2014.

[100] S. Yagi, I. Yamada, H. Tsukasaki, A. Seno, M. Murakami, H. Fujii, H. Chen, N. Umezawa, H. Abe, N. Nishiyama, *et al.*, "Covalency-reinforced oxygen evolution reaction catalyst," *Nature communications*, vol. 6, p. 8249, 2015.

[101] A. Grimaud, O. Diaz-Morales, B. Han, W. T. Hong, Y.-L. Lee, L. Giordano, K. A. Stoerzinger, M. T. Koper, and Y. Shao-Horn, "Activating lattice oxygen redox reactions in metal oxides to catalyse oxygen evolution," *Nature chemistry*, vol. 9, no. 5, p. 457, 2017.

[102] J. T. Mefford, X. Rong, A. M. Abakumov, W. G. Hardin, S. Dai, A. M. Kolpak, K. P. Johnston, and K. J. Stevenson, "Water electrolysis on la 1- x sr x coo 3- δ perovskite electrocatalysts," *Nature communications*, vol. 7, p. ncomms11053, 2016.

[103] X. Rong, J. Parolin, and A. M. Kolpak, "A fundamental relationship between reaction mechanism and stability in metal oxide catalysts for oxygen evolution," *ACS Catalysis*, vol. 6, no. 2, pp. 1153–1158, 2016.

[104] J. R. Petrie, V. R. Cooper, J. W. Freeland, T. L. Meyer, Z. Zhang, D. A. Lutterman, and H. N. Lee, "Enhanced bifunctional oxygen catalysis in strained lanio3 perovskites," *Journal of the American Chemical Society*, vol. 138, no. 8, pp. 2488–2491, 2016.

[105] Y. Choi, D. S. Mebane, M. Lin, and M. Liu, "Oxygen reduction on lamno3-based cathode materials in solid oxide fuel cells," *Chemistry of Materials*, vol. 19, no. 7, pp. 1690–1699, 2007.

[106] R. Evarestov, E. Kotomin, Y. A. Mastrikov, D. Gryaznov, E. Heifets, and J. Maier, "Comparative density-functional lcao and plane-wave calculations of la mn o 3 surfaces," *Physical Review B*, vol. 72, no. 21, p. 214411, 2005.

[107] Z. Feng, E. J. Crumlin, W. T. Hong, D. Lee, E. Mutoro, M. D. Biegalski, H. Zhou, H. Bluhm, H. M. Christen, and Y. Shao-Horn, "In situ studies of the temperature-dependent surface structure and chemistry of single-crystalline (001)-oriented la0. 8sr0. 2coo3- δ perovskite thin films," *The journal of physical chemistry letters*, vol. 4, no. 9, pp. 1512–1518, 2013.

[108] J. Druce, H. Tellez, M. Burriel, M. Sharp, L. Fawcett, S. Cook, D. McPhail, T. Ishihara, H. Brongersma, and J. Kilner, "Surface termination and subsurface restructuring of perovskite-based solid oxide electrode materials," *Energy & Environmental Science*, vol. 7, no. 11, pp. 3593–3599, 2014.

[109] K. A. Stoerzinger, W. T. Hong, E. J. Crumlin, H. Bluhm, M. D. Biegalski, and Y. Shao-Horn, "Water reactivity on the lacoo3 (001) surface: an ambient pressure x-ray photoelectron spectroscopy study," *The Journal of Physical Chemistry C*, vol. 118, no. 34, pp. 19733–19741, 2014.

[110] K. A. Stoerzinger, W. T. Hong, G. Azimi, L. Giordano, Y.-L. Lee, E. J. Crumlin, M. D. Biegalski, H. Bluhm, K. K. Varanasi, and Y. Shao-Horn, "Reactivity of perovskites with water: role of hydroxylation in wetting and implications for oxygen electrocatalysis," *The Journal of Physical Chemistry C*, vol. 119, no. 32, pp. 18504–18512, 2015.

[111] P. E. Blöchl, "Projector augmented-wave method," *Physical review B*, vol. 50, no. 24, p. 17953, 1994.

[112] H. J. Monkhorst and J. D. Pack, "Special points for brillouin-zone integrations," *Physical review B*, vol. 13, no. 12, p. 5188, 1976.

[113] W. Tang, E. Sanville, and G. Henkelman, "A grid-based bader analysis algorithm without lattice bias," *Journal of Physics: Condensed Matter*, vol. 21, no. 8, p. 084204, 2009.

[114] E. Sanville, S. D. Kenny, R. Smith, and G. Henkelman, "Improved grid-based algorithm for bader charge allocation," *Journal of computational chemistry*, vol. 28, no. 5, pp. 899–908, 2007.

[115] G. Henkelman, A. Arnaldsson, and H. Jónsson, "A fast and robust algorithm for bader decomposition of charge density," *Computational Materials Science*, vol. 36, no. 3, pp. 354–360, 2006.

[116] M. Yu and D. R. Trinkle, "Accurate and efficient algorithm for bader charge integration," *The Journal of chemical physics*, vol. 134, no. 6, p. 064111, 2011.

[117] G. Henkelman, B. P. Uberuaga, and H. Jónsson, "A climbing image nudged elastic band method for finding saddle points and minimum energy paths," *The Journal of chemical physics*, vol. 113, no. 22, pp. 9901–9904, 2000.

[118] G. Henkelman and H. Jónsson, "Improved tangent estimate in the nudged elastic band method for finding minimum energy paths and saddle points," *The Journal of chemical physics*, vol. 113, no. 22, pp. 9978–9985, 2000.

[119] K. Mathew, R. Sundararaman, K. Letchworth-Weaver, T. Arias, and R. G. Hennig, "Implicit solvation model for density-functional study of nanocrystal surfaces and reaction pathways," *The Journal of chemical physics*, vol. 140, no. 8, p. 084106, 2014.

[120] M. Fishman, H. L. Zhuang, K. Mathew, W. Dirschka, and R. G. Hennig, "Accuracy of exchange-correlation functionals and effect of solvation on the surface energy of copper," *Physical Review B*, vol. 87, no. 24, p. 245402, 2013.

[121] J. Rossmeisl, Z.-W. Qu, H. Zhu, G.-J. Kroes, and J. K. Nørskov, "Electrolysis of water on oxide surfaces," *Journal of Electroanalytical Chemistry*, vol. 607, no. 1-2, pp. 83–89, 2007.

[122] W. G. Hardin, D. A. Slanac, X. Wang, S. Dai, K. P. Johnston, and K. J. Stevenson, "Highly active, nonprecious metal perovskite electrocatalysts for bifunctional metal–air battery electrodes," *The journal of physical chemistry letters*, vol. 4, no. 8, pp. 1254–1259, 2013.

[123] L. Pauling, *The Nature of the Chemical Bond...*, vol. 260. Cornell university press Ithaca, NY, 1960.

[124] S. Lias, "Ionization energy evaluation," *NIST chemistry webbook, NIST standard reference database*, vol. 69, 2005.

[125] L. Wang, T. Maxisch, and G. Ceder, "Oxidation energies of transition metal oxides within the gga+ u framework," *Physical Review B*, vol. 73, no. 19, p. 195107, 2006.

[126] C. Rao, J. Gopalakrishnan, and K. Vidyasagar, "Superstructures, ordered defects & nonstoichiometry in metal oxides of perovskite & related structures," in *Solid State Chemistry: Selected Papers of CNR Rao*, pp. 275–294, World Scientific, 1995.

[127] R.-A. Eichel, "Structural and dynamic properties of oxygen vacancies in perovskite oxidesanalysis of defect chemistry by modern multi-frequency and pulsed epr techniques," *Physical Chemistry Chemical Physics*, vol. 13, no. 2, pp. 368–384, 2011.

[128] P. Lambeck and G. Jonker, "Ferroelectric domain stabilization in batio3 by bulk ordering of defects," *Ferroelectrics*, vol. 22, no. 1, pp. 729–731, 1978.

[129] G. Arlt and H. Neumann, "Internal bias in ferroelectric ceramics: origin and time dependence," *Ferroelectrics*, vol. 87, no. 1, pp. 109–120, 1988.

[130] M. I. Morozov and D. Damjanovic, "Hardening-softening transition in fe-doped pb (zr, ti) o 3 ceramics and evolution of the third harmonic of the polarization response," *Journal of Applied Physics*, vol. 104, no. 3, p. 034107, 2008.

[131] J. Scott and M. Dawber, "Oxygen-vacancy ordering as a fatigue mechanism in perovskite ferroelectrics," *Applied Physics Letters*, vol. 76, no. 25, pp. 3801–3803, 2000.

[132] A. Rothschild, W. Menesklou, H. L. Tuller, and E. Ivers-Tiffee, "Electronic structure, defect chemistry, and transport properties of srti1-x fe x o3-y solid solutions," *Chemistry of materials*, vol. 18, no. 16, pp. 3651–3659, 2006.

[133] M. Martin, "Oxygen and cation diffusion processes in oxygen ion conductors," *Diffusion Fundamentals*, vol. 6, pp. 39–1, 2007.

[134] R. Merkle and J. Maier, "How is oxygen incorporated into oxides? a comprehensive kinetic study of a simple solid-state reaction with srtio3 as a model material," *Angewandte Chemie International Edition*, vol. 47, no. 21, pp. 3874–3894, 2008.

[135] N. G. Petrik, Z. Zhang, Y. Du, Z. Dohnálek, I. Lyubinetsky, and G. A. Kimmel, "Chemical reactivity of reduced tio2 (110): the dominant role of surface defects in oxygen chemisorption," *The Journal of Physical Chemistry C*, vol. 113, no. 28, pp. 12407–12411, 2009.

[136] J.-I. Jung, S. Park, M.-G. Kim, and J. Cho, "Tunable internal and surface structures of the bifunctional oxygen perovskite catalysts," *Advanced Energy Materials*, vol. 5, no. 24, p. 1501560, 2015.

[137] J. R. Petrie, H. Jeen, S. C. Barron, T. L. Meyer, and H. N. Lee, "Enhancing perovskite electrocatalysis through strain tuning of the oxygen deficiency," *Journal of the American Chemical Society*, vol. 138, no. 23, pp. 7252–7255, 2016.

[138] J. G. Lee, J. Hwang, H. J. Hwang, O. S. Jeon, J. Jang, O. Kwon, Y. Lee, B. Han, and Y.-G. Shul, "A new family of perovskite catalysts for oxygen-evolution reaction in alkaline media: Banio3 and bani0. 83o2. 5," *Journal of the American Chemical Society*, vol. 138, no. 10, pp. 3541–3547, 2016.

[139] F. Esch, S. Fabris, L. Zhou, T. Montini, C. Africh, P. Fornasiero, G. Comelli, and R. Rosei, "Electron localization determines defect formation on ceria substrates," *Science*, vol. 309, no. 5735, pp. 752–755, 2005.

[140] J.-I. Jung, H. Y. Jeong, M. G. Kim, G. Nam, J. Park, and J. Cho, "Fabrication of ba0. 5sr0. 5co0. 8fe0. 2o3–δ catalysts with enhanced electrochemical performance by removing an inherent heterogeneous surface film layer," *Advanced Materials*, vol. 27, no. 2, pp. 266–271, 2015.

[141] P. Pasierb, S. Komornicki, and M. Rekas, "Comparison of the chemical diffusion of undoped and nb-doped srtio3," *Journal of Physics and Chemistry of Solids*, vol. 60, no. 11, pp. 1835–1844, 1999.

[142] M. Kubicek, Z. Cai, W. Ma, B. Yildiz, H. Hutter, and J. Fleig, "Tensile lattice strain accelerates oxygen surface exchange and diffusion in la1–x sr x coo3- δ thin films," *ACS nano*, vol. 7, no. 4, pp. 3276–3286, 2013.

[143] O. Bikondoa, C. L. Pang, R. Ithnin, C. A. Muryn, H. Onishi, and G. Thornton, "Direct visualization of defect-mediated dissociation of water on tio 2 (110)," *Nature materials*, vol. 5, no. 3, p. 189, 2006.

[144] J. Kim, X. Yin, K.-C. Tsao, S. Fang, and H. Yang, "Ca2mn2o5 as oxygen-deficient perovskite electrocatalyst for oxygen evolution reaction," *Journal of the American Chemical Society*, vol. 136, no. 42, pp. 14646–14649, 2014.

[145] S. H. Chang, N. Danilovic, K.-C. Chang, R. Subbaraman, A. P. Paulikas, D. D. Fong, M. J. Highland, P. M. Baldo, V. R. Stamenkovic, J. W. Freeland, *et al.*, "Functional links between stability and reactivity of strontium ruthenate single crystals during oxygen evolution," *Nature communications*, vol. 5, p. 4191, 2014.

[146] A. Grimaud, K. J. May, C. E. Carlton, Y.-L. Lee, M. Risch, W. T. Hong, J. Zhou, and Y. Shao-Horn, "Double perovskites as a family of highly active catalysts for oxygen evolution in alkaline solution," *Nature communications*, vol. 4, p. 2439, 2013.

[147] M. Bajdich, M. García-Mota, A. Vojvodic, J. K. Nørskov, and A. T. Bell, "Theoretical investigation of the activity of cobalt oxides for the electrochemical oxidation of water," *Journal of the American chemical Society*, vol. 135, no. 36, pp. 13521–13530, 2013.

[148] J. Suntivich, K. J. May, H. A. Gasteiger, J. B. Goodenough, and Y. Shao-Horn, "A perovskite oxide optimized for oxygen evolution catalysis from molecular orbital principles," *Science*, vol. 334, no. 6061, pp. 1383–1385, 2011.

[149] W. Zhou and J. Sunarso, "Enhancing bi-functional electrocatalytic activity of perovskite by temperature shock: A case study of lanio3- δ," *The journal of physical chemistry letters*, vol. 4, no. 17, pp. 2982–2988, 2013.

[150] J. Yu, J. Sunarso, Y. Zhu, X. Xu, R. Ran, W. Zhou, and Z. Shao, "Activity and stability of ruddlesden–popper-type lan+ 1nino3n+ 1 (n= 1, 2, 3, and) electrocatalysts for oxygen reduction and evolution reactions in alkaline media," *Chemistry–A European Journal*, vol. 22, no. 8, pp. 2719–2727, 2016.

[151] M. T. Colomer, D. A. Fumo, J. R. Jurado, and A. M. Segadas, "Non-stoichiometric la (1–x) nio (3–δ) perovskites produced by combustion synthesis," *Journal of Materials Chemistry*, vol. 9, no. 10, pp. 2505–2510, 1999.

[152] R. Dronskowski and P. E. Blöchl, "Crystal orbital hamilton populations (cohp): energy-resolved visualization of chemical bonding in solids based on density-functional calculations," *The Journal of Physical Chemistry*, vol. 97, no. 33, pp. 8617–8624, 1993.

[153] V. L. Deringer, A. L. Tchougréeff, and R. Dronskowski, "Crystal orbital hamilton population (cohp) analysis as projected from plane-wave basis sets," *The Journal of Physical Chemistry A*, vol. 115, no. 21, pp. 5461–5466, 2011.

[154] S. Maintz, V. L. Deringer, A. L. Tchougréeff, and R. Dronskowski, "Analytic projection from plane-wave and paw wavefunctions and application to chemical-bonding analysis in solids," *Journal of computational chemistry*, vol. 34, no. 29, pp. 2557–2567, 2013.

[155] S. Maintz, V. L. Deringer, A. L. Tchougréeff, and R. Dronskowski, "Lobster: A tool to extract chemical bonding from plane-wave based dft," *Journal of computational chemistry*, vol. 37, no. 11, pp. 1030–1035, 2016.

[156] A. Garg, D. Gonalves, Y. Liu, Z. Wang, L. Wang, J. S. Yoo, A. Kolpak, R. M. Rioux, D. Zanchet, and Y. Romn-Leshkov, "Probing the structural and electronic properties of pt-coated transition metal carbide and nitride nanoparticles through in-situ x-ray absorption spectroscopy," *ACS Catalysts*, vol. In Revision, 2019.

[157] F. E. López-Suárez, A. Bueno-López, K. I. B. Eguiluz, and G. R. Salazar-Banda, "Pt–sn/c catalysts prepared by sodium borohydride reduction for alcohol oxidation in fuel cells: Effect of the precursor addition order," *Journal of Power Sources*, vol. 268, pp. 225–232, 2014.

[158] K. Sasaki, H. Naohara, Y. Cai, Y. M. Choi, P. Liu, M. B. Vukmirovic, J. X. Wang, and R. R. Adzic, "Core-protected platinum monolayer shell high-stability electrocatalysts for fuel-cell cathodes," *Angewandte Chemie International Edition*, vol. 49, no. 46, pp. 8602–8607, 2010.

[159] R. R. Adzic, J. Zhang, K. Sasaki, M. B. Vukmirovic, M. Shao, J. Wang, A. U. Nilekar, M. Mavrikakis, J. Valerio, and F. Uribe, "Platinum monolayer fuel cell electrocatalysts," *Topics in Catalysis*, vol. 46, no. 3-4, pp. 249–262, 2007.

[160] J. Hu, L. Wu, K. A. Kuttiyiel, K. R. Goodman, C. Zhang, Y. Zhu, M. B. Vukmirovic, M. G. White, K. Sasaki, and R. R. Adzic, "Increasing stability and activity of core–shell catalysts by preferential segregation of oxide on edges and vertexes: oxygen reduction on ti–au@ pt/c," *Journal of the American Chemical Society*, vol. 138, no. 29, pp. 9294–9300, 2016.

[161] D. V. Esposito and J. G. Chen, "Monolayer platinum supported on tungsten carbides as low-cost electrocatalysts: opportunities and limitations," *Energy & Environmental Science*, vol. 4, no. 10, pp. 3900–3912, 2011.

[162] A. L. Strickler, A. Jackson, and T. F. Jaramillo, "Active and stable ir@ pt core–shell catalysts for electrochemical oxygen reduction," *ACS Energy Letters*, vol. 2, no. 1, pp. 244–249, 2016.

[163] T. G. Kelly and J. G. Chen, "Metal overlayer on metal carbide substrate: unique bimetallic properties for catalysis and electrocatalysis," *Chemical Society Reviews*, vol. 41, no. 24, pp. 8021–8034, 2012.

[164] M. Oezaslan, F. Hasche, and P. Strasser, "Pt-based core–shell catalyst architectures for oxygen fuel cell electrodes," *The Journal of Physical Chemistry Letters*, vol. 4, no. 19, pp. 3273–3291, 2013.

[165] S. Wannakao, N. Artrith, J. Limtrakul, and A. M. Kolpak, "Catalytic activity and product selectivity trends for carbon dioxide electroreduction on transition metal-coated tungsten carbides," *The Journal of Physical Chemistry C*, vol. 121, no. 37, pp. 20306–20314, 2017.

[166] M. Neylon, S. Choi, H. Kwon, K. Curry, and L. Thompson, "Catalytic properties of early transition metal nitrides and carbides: n-butane hydrogenolysis, dehydrogenation and isomerization," *Applied Catalysis A: General*, vol. 183, no. 2, pp. 253–263, 1999.

[167] S. Ramanathan and S. T. Oyama, "New catalysts for hydroprocessing: transition metal carbides and nitrides," *The Journal of Physical Chemistry*, vol. 99, no. 44, pp. 16365–16372, 1995.

[168] C. C. Yu, S. Ramanathan, B. Dhandapani, J. Chen, and S. T. Oyama, "Bimetallic nb- mo carbide hydroprocessing catalysts: Synthesis, characterization, and activity studies," *The Journal of Physical Chemistry B*, vol. 101, no. 4, pp. 512–518, 1997.

[169] E. Iglesia, J. E. Baumgartner, F. H. Ribeiro, and M. Boudart, "Bifunctional reactions of alkanes on tungsten carbides modified by chemisorbed oxygen," *Journal of Catalysis*, vol. 131, no. 2, pp. 523–544, 1991.

[170] F. H. Ribeiro, R. A. Dalla Betta, M. Boudart, J. Baumgartner, and E. Iglesia, "Reactions of neopentane, methylcyclohexane, and 3, 3-dimethylpentane on tungsten carbides: the effect of surface oxygen on reaction pathways," *Journal of Catalysis*, vol. 130, no. 1, pp. 86–105, 1991.

[171] J.-G. Choi, J. R. Brenner, C. W. Colling, B. G. Demczyk, J. L. Dunning, and L. T. Thompson, "Synthesis and characterization of molybdenum nitride hydrodenitrogenation catalysts," *Catalysis Today*, vol. 15, no. 2, pp. 201–222, 1992.

[172] J. Patt, D. J. Moon, C. Phillips, and L. Thompson, "Molybdenum carbide catalysts for water–gas shift," *Catalysis Letters*, vol. 65, no. 4, pp. 193–195, 2000.

[173] M. Yang, Z. Cui, and F. J. DiSalvo, "Mesoporous titanium nitride supported pt nanoparticles as high performance catalysts for methanol electrooxidation," *Physical Chemistry Chemical Physics*, vol. 15, no. 4, pp. 1088–1092, 2013.

[174] V. Molinari, C. Giordano, M. Antonietti, and D. Esposito, "Titanium nitride-nickel nanocomposite as heterogeneous catalyst for the hydrogenolysis of aryl ethers," *Journal of the American Chemical Society*, vol. 136, no. 5, pp. 1758–1761, 2014.

[175] Y. Zhong, X. Xia, F. Shi, J. Zhan, J. Tu, and H. J. Fan, "Transition metal carbides and nitrides in energy storage and conversion," *Advanced science*, vol. 3, no. 5, p. 1500286, 2016.

[176] J. R. Kitchin, J. K. Nørskov, M. A. Barteau, and J. Chen, "Role of strain and ligand effects in the modification of the electronic and chemical properties of bimetallic surfaces," *Physical review letters*, vol. 93, no. 15, p. 156801, 2004.

[177] J. Kitchin, J. K. Nørskov, M. Barteau, and J. Chen, "Modification of the surface electronic and chemical properties of pt (111) by subsurface 3d transition metals," *The Journal of chemical physics*, vol. 120, no. 21, pp. 10240–10246, 2004.

[178] T. Ghosh, M. B. Vukmirovic, F. J. DiSalvo, and R. R. Adzic, "Intermetallics as novel supports for pt monolayer o2 reduction electrocatalysts: potential for significantly improving properties," *Journal of the American Chemical Society*, vol. 132, no. 3, pp. 906–907, 2009.

[179] K. Gong, D. Su, and R. R. Adzic, "Platinum-monolayer shell on auni0. 5fe nanoparticle core electrocatalyst with high activity and stability for the oxygen reduction reaction," *Journal of the American Chemical Society*, vol. 132, no. 41, pp. 14364–14366, 2010.

[180] K. A. Kuttiyiel, K. Sasaki, Y. Choi, D. Su, P. Liu, and R. R. Adzic, "Nitride stabilized ptni core–shell nanocatalyst for high oxygen reduction activity," *Nano letters*, vol. 12, no. 12, pp. 6266–6271, 2012.

[181] X. Tian, J. Luo, H. Nan, H. Zou, R. Chen, T. Shu, X. Li, Y. Li, H. Song, S. Liao, *et al.*, "Transition metal nitride coated with atomic layers of pt as a low-cost, highly stable electrocatalyst for the oxygen reduction reaction," *Journal of the American Chemical Society*, vol. 138, no. 5, pp. 1575–1583, 2016.

[182] D. Wang, H. L. Xin, H. Wang, Y. Yu, E. Rus, D. A. Muller, F. J. DiSalvo, and H. D. Abrua, "Facile synthesis of carbon-supported pd–co core–shell nanoparticles as oxygen reduction electrocatalysts and their enhanced activity and stability with monolayer pt decoration," *Chemistry of Materials*, vol. 24, no. 12, pp. 2274–2281, 2012.

[183] M. Brown, R. Peierls, and E. Stern, "White lines in x-ray absorption," *Physical Review B*, vol. 15, no. 2, p. 738, 1977.

[184] D. E. Sayers, E. A. Stern, and F. W. Lytle, "New technique for investigating noncrystalline structures: Fourier analysis of the extended x-rayabsorption fine structure," *Physical review letters*, vol. 27, no. 18, p. 1204, 1971.

[185] N. V. Long, T. D. Hien, T. Asaka, M. Ohtaki, and M. Nogami, "Synthesis and characterization of pt–pd alloy and core-shell bimetallic nanoparticles for direct methanol fuel cells (dmfcs): Enhanced electrocatalytic properties of well-shaped core-shell morphologies and nanostructures," *international journal of hydrogen energy*, vol. 36, no. 14, pp. 8478–8491, 2011.

[186] X. Wang, S.-I. Choi, L. T. Roling, M. Luo, C. Ma, L. Zhang, M. Chi, J. Liu, Z. Xie, J. A. Herron, *et al.*, "Palladium–platinum core-shell icosahedra with substantially enhanced activity and durability towards oxygen reduction," *Nature communications*, vol. 6, p. 7594, 2015.

[187] J. Rossmeisl, G. S. Karlberg, T. Jaramillo, and J. K. Nørskov, "Steady state oxygen reduction and cyclic voltammetry," *Faraday discussions*, vol. 140, pp. 337–346, 2009.

[188] B. Hammer and J. K. Nørskov, "Theoretical surface science and catalysiscalculations and concepts," in *Advances in catalysis*, vol. 45, pp. 71–129, Elsevier, 2000.

[189] Y. Lei, J. Jelic, L. C. Nitsche, R. Meyer, and J. Miller, "Effect of particle size and adsorbates on the l 3, l 2 and l 1 x-ray absorption near edge structure of supported pt nanoparticles," *Topics in Catalysis*, vol. 54, no. 5-7, pp. 334–348, 2011.

[190] A. Mansour, J. Cook Jr, and D. Sayers, "Quantitative technique for the determination of the number of unoccupied d-electron states in a platinum catalyst using the l2, 3 x-ray absorption edge spectra," *The Journal of Physical Chemistry*, vol. 88, no. 11, pp. 2330–2334, 1984.

[191] T. R. Wilken, W. R. Morcom, C. A. Wert, and J. B. Woodhouse, "Reduction of tungsten oxide to tungsten metal," *Metallurgical Transactions B*, vol. 7, no. 4, pp. 589–597, 1976.

[192] R. P. Forslund, W. G. Hardin, X. Rong, A. M. Abakumov, D. Filimonov, C. T. Alexander, J. T. Mefford, H. Iyer, A. M. Kolpak, K. P. Johnston, *et al.*, "Exceptional electrocatalytic oxygen evolution via tunable charge transfer interactions in la 0.5 sr 1.5 ni 1- x fe x o $4\pm\delta$ ruddlesden-popper oxides," *Nature communications*, vol. 9, no. 1, p. 3150, 2018.

[193] Q. Zhu, L. Li, A. R. Oganov, and P. B. Allen, "Evolutionary method for predicting surface reconstructions with variable stoichiometry," *Physical Review B*, vol. 87, no. 19, p. 195317, 2013.

[194] Q. Wang, A. R. Oganov, Q. Zhu, and X.-F. Zhou, "New reconstructions of the (110) surface of rutile tio 2 predicted by an evolutionary method," *Physical review letters*, vol. 113, no. 26, p. 266101, 2014.

[195] X.-F. Zhou, A. R. Oganov, X. Shao, Q. Zhu, and H.-T. Wang, "Unexpected reconstruction of the α-boron (111) surface," *Physical review letters*, vol. 113, no. 17, p. 176101, 2014.

[196] Z. W. Ulissi, A. R. Singh, C. Tsai, and J. K. Nørskov, "Automated discovery and construction of surface phase diagrams using machine learning," *The journal of physical chemistry letters*, vol. 7, no. 19, pp. 3931–3935, 2016.

[197] R. B. Wexler, T. Qiu, and A. M. Rappe, "Automatic prediction of surface phase diagrams using ab initio grand canonical monte carlo," *The Journal of Physical Chemistry C*, 2019.